

BMO TR-81-1

SAI DOCUMENT NO. SAI-79-506-VF

2
LEVEL III
#108544

**PERFORMANCE TECHNOLOGY PROGRAM
(PTP-S II)**

VOLUME III

INVISCID AERODYNAMIC PREDICTIONS FOR BALLISTIC REENTRY
VEHICLES WITH ABLATED NOSETIPS

SCIENCE APPLICATIONS, INC.
APPLIED MECHANICS OPERATION
WAYNE, PENNSYLVANIA, 19087

SEPTEMBER, 1979

FINAL REPORT FOR PERIOD MARCH 1978 - SEPTEMBER 1979

CONTRACT NO. F04701-77-C-0126

APPROVED FOR PUBLIC RELEASE; DISTRIBUTION UNLIMITED.
ALL OF AFR 80-45 APPLIES.

AIR FORCE BALLISTIC MISSILE OFFICE
NORTON AFB, CALIFORNIA 92409

DTIC
ELECTE
DEC 28 1981
S D D

11746

81 12 23 117

AD A108845

DTIC FILE COPY

This final report was submitted by Science Applications, Inc., 1200 Prospect Street, La Jolla, California 92038, under Contract Number F04701-77-C-0126 with the Ballistic Missile Office, AFSC, Norton AFB, California. Major Kevin E. Yelmgren, BMO/SYDT, was the Project Officer in charge. This technical report has been reviewed and is approved for publication.

Kevin E. Yelmgren

KEVIN E. YELMGREN, Major, USAF
Chief, Vehicle Technology Branch
Reentry Technology Division
Advanced Ballistic Reentry Systems

FOR THE COMMANDER

Nicholas C. Belmonte

NICHOLAS C. BELMONTE, Lt Col, USAF
Director, Reentry Technology Division
Advanced BALLISTIC Reentry Systems

UNCLASSIFIED

SECURITY CLASSIFICATION OF THIS PAGE (When Data Entered)

REPORT DOCUMENTATION PAGE		READ INSTRUCTIONS BEFORE COMPLETING FORM	
1. REPORT NUMBER BMO TR-81-1	2. GOVT ACCESSION NO. AD-A108	3. RECIPIENT'S CATALOG NUMBER 845	
4. TITLE (and Subtitle) "Performance Technology Program (PTP-S II), Vol. III, Inviscid Aerodynamic Predictions for Ballistic Reentry Vehicles with Ablated Nosedtips."		5. TYPE OF REPORT & PERIOD COVERED Final Report: 3/78 to 9/79	
7. AUTHOR(s) Darryl W. Hall		6. PERFORMING ORG. REPORT NUMBER SAI-79-506-VF - Vol-3	
9. PERFORMING ORGANIZATION NAME AND ADDRESS Science Applications, Inc. 994 Old Eagle School Rd., Ste. 1018 Wayne, Pennsylvania 19087		8. CONTRACT OR GRANT NUMBER(s) F04701-77-C-0126	
11. CONTROLLING OFFICE NAME AND ADDRESS Ballistic Missile Office Norton AFB, California 92409		10. PROGRAM ELEMENT, PROJECT, TASK AREA & WORK UNIT NUMBERS Task 3.2.1.2	
14. MONITORING AGENCY NAME & ADDRESS (if different from Controlling Office)		12. REPORT DATE September 1979	
		13. NUMBER OF PAGES 169	
		15. SECURITY CLASS. (of this report) Unclassified	
		15a. DECLASSIFICATION/DOWNGRADING SCHEDULE	
16. DISTRIBUTION STATEMENT (of this Report) Approved for public release; distribution unlimited. All of AFR 80-45 applies.			
17. DISTRIBUTION STATEMENT (of the abstract entered in Block 20, if different from Report)			
18. SUPPLEMENTARY NOTES			
19. KEY WORDS (Continue on reverse side if necessary and identify by block number) Flow Field Blunt Body Code Reentry Vehicles Asymmetric Nosedtips Conformal Mapping			
20. ABSTRACT (Continue on reverse side if necessary and identify by block number) A three-dimensional inviscid time-dependent blunt body flow field code is developed for calculation of hypersonic flow over ablated reentry vehicle nosetips. The code is formulated in a coordinate system that is based on a sequence of conformal mappings and is capable of being aligned with arbitrary nosetip shapes. This procedure includes a finite difference scheme that permits the automatic calculation of embedded shocks in an approximate manner.			

DD FORM 1473
(FACSIMILE)

UNCLASSIFIED

SECURITY CLASSIFICATION OF THIS PAGE (When Data Entered)

UNCLASSIFIED

SECURITY CLASSIFICATION OF THIS PAGE(When Data Entered)

19. KEY WORDS (Continued)

20. ABSTRACT (Continued)

BLANK PAGE

TABLE OF CONTENTS

	<u>Page</u>
ABSTRACT (DD1473)	i
TABLE OF CONTENTS	1
LIST OF FIGURES	3
NOMENCLATURE	6
SECTION 1 INTRODUCTION	9
SECTION 2 PROBLEM DEFINITION	15
2.1 STATEMENT OF THE PROBLEM	15
2.2 OUTLINE OF APPROACH	18
SECTION 3 COORDINATE SYSTEM AND GOVERNING EQUATIONS	22
3.1 INVISCID EQUATIONS OF MOTION	22
3.2 THREE-DIMENSIONAL CONFORMAL TRANSFORMATION	26
3.3 TRANSFORMED EQUATIONS OF MOTION	40
3.4 COMPUTATIONAL TRANSFORMATION	44
3.5 CHARACTERISTIC RELATIONS	52
3.6 TREATMENT OF THE SINGULAR CENTERLINE	58
SECTION 4 CALCULATION OF EMBEDDED SHOCKS	67
4.1 CONSERVATION LAW APPROACH TO SHOCK-CAPTURING	67
4.2 λ -DIFFERENCING APPROACH TO SHOCK-CAPTURING	75
4.3 COMPARISON OF AXISYMMETRIC SHOCK-CAPTURING PROCEDURES	80
4.4 λ -DIFFERENCING SCHEME IN THREE DIMENSIONS	88
SECTION 5 NUMERICAL PROCEDURES	91
5.1 TIME-ASYMPTOTIC SOLUTION & INITIALIZATION	91
5.2 NON-CONSERVATION FIELD POINT TREATMENT	95
5.3 BODY POINT TREATMENT	97

TABLE OF CONTENTS (Cont'd.)

	<u>Page</u>
5.4 BOW SHOCK POINT TREATMENT	100
5.5 CENTERLINE POINT TREATMENT	105
5.6 CONSERVATION FIELD POINT TREATMENT	109
5.7 λ -DIFFERENCING FIELD POINT TREATMENT	112
SECTION 6 VALIDATION OF SOLUTION	114
6.1 LIMITATIONS OF TECHNIQUE	114
6.2 CONVERGENCE PROPERTIES	116
6.3 VALIDATION OF NOSETIP SOLUTION	123
6.4 PREDICTION OF TOTAL VEHICLE INVISCID AERODYNAMICS	136
SECTION 7 CONCLUSIONS	156
SECTION 8 REFERENCES	160
SECTION 9 APPENDIX: COEFFICIENTS FOR THE SHOCK ACCELERATION EQUATION	163

Accession For	
NTIS GRA&I	<input checked="" type="checkbox"/>
DTIC TAB	<input type="checkbox"/>
Unannounced	<input type="checkbox"/>
Justification	
By	
Distribution/	
Availability Codes	
Dist	Avail and/or Special
A	

S DTIC
 ELECTE **D**
 DEC 28 1981
D

LIST OF FIGURES

<u>Figure</u>		<u>Page</u>
1.1	Typical Nose Shape Progression	10
1.2	Schlieren Photograph of Ablated Nostip with Embedded Shock	13
2.1	Re _{co} -M _∞ Map of Flow Regimes with Typical Reentry Vehicle Trajectory Superimposed	16
3.1	Hinge Point Definition	29
3.2	Hinge Point Images (Sphere)	31
3.3	ζ Plane Hinge Point Images and Body Contour (Sphere)	33
3.4	Body Contour in Transformed Plane for 50°/10° Biconic Nose	36
3.5	Body Contour in Transformed Plane for Very Mildly Indented Body	37
3.6	Body Contour in Transformed Plane for PANT Triconic	38
3.7	Body Contour in Transformed Plane for Indented Nose Shape	39
3.8	Computational Mesh for Spherical Nose	49
3.9	Computational Mesh for PANT Triconic	50
3.10	Computational Mesh for Indented Nose Shape	51
3.11	Cartesian Coordinate System at the Centerline	60
3.12	Unit Vectors at Centerline	64
4.1	Steady Inclined Shock	68
4.2	Unsteady Normal Shock	70
4.3	Characteristic Slopes in x-t Plane	77
4.4	Shock Shape Predictions for VMIB at M _∞ = 7.2	81
4.5	Surface Pressure Predictions for VMIB at M _∞ = 7.2	82
4.6	Effect of Damping on Shock Shape Predictions with Conservation Scheme	84

LIST OF FIGURES (Cont'd.)

<u>Figure</u>		<u>Page</u>
4.7	Shock Shape Predictions for MIB at $M_\infty = 9$	86
5.1	Numerical Domain of Dependence for Regular MacCormack Scheme	110
5.2	Typical Alignment of Embedded Shock in Y-Z Coordinate Mesh	111
5.3	Numerical Domain of Dependence for MacCormack Scheme Inverted in Z-direction	112
6.1	Typical p_0 History (Converged)	119
6.2	Typical p_0 History (Not Converged)	120
6.3	Typical $(c_T/G)_{rms}$ History (Converged)	121
6.4	Typical $(c_T/G)_{rms}$ History (Not Converged)	122
6.5	Shock Shape Predictions for a Sphere in Equilibrium Real Gas	125
6.6	Predictions of Surface Pressure Distribution for a Sphere in Equilibrium Real Gas	126
6.7	CM3DT(NC) Prediction of Surface Pressure Distribution for the PANT Triconic (with Cone) at $M_\infty = 5, \alpha = 0^\circ$	128
6.8	CM3DT(NC) Prediction of Surface Pressure Distribution for the PANT Triconic (without Cone) at $M_\infty = 5, \alpha = 0^\circ$	129
6.9	CM3DT(λ) Prediction of Surface Pressure Distribution for the PANT Triconic (with Cone) at $M_\infty = 5, \alpha = 0^\circ$	130
6.10	CM3DT Shock Shape Predictions for the PANT Triconic at $M_\infty = 5, \alpha = 0^\circ$	131
6.11	Surface Pressure Predictions for the PANT Simple Biconic at $M_\infty = 5, \alpha = 5^\circ$	133
6.12	Bow Shock Shape Predictions for the Blunt-1 Shape at $M_\infty = 13.4, \alpha = 3^\circ$	135
6.13	Surface Pressure Predictions for the PANT Triconic at $M_\infty = 5, \alpha = 10^\circ$	137
6.14	Normal Force and Pitching Moment Coefficients vs. Angle of Attack for 9° Sphere-Cone of 15% Bluntness at $M_\infty = 20, \alpha = 0^\circ$	139

LIST OF FIGURES (Cont'd.)

<u>Figure</u>		<u>Page</u>
6.15	Pitch Center of Pressure vs. Bluntness Ratio for 9° Sphere-Cone at $M_\infty = 20$, $\alpha = 5^\circ$, $\beta = 0^\circ$	141
6.16	Normal Force and Pitching Moment Coefficients vs. Angle of Attack for 9° Sphere-Cone of 15% Bluntness at $M_\infty = 20$, $\beta = 5^\circ$	142
5.17	Normal Force Coefficient vs. Angle of Attack for Blunt-1 Configuration at $M_\infty = 13.4$, 20 KFT Altitude	143
6.18	Pitching Moment Coefficient vs. Angle of Attack for Blunt-1 Configuration at $M_\infty = 13.4$, 20 KFT Altitude	144
6.19	N8 Configuration	146
6.20	Normal Force Coefficient vs. Angle of Attack for N8 Configuration at $M_\infty = 8$	148
6.21	Pitching Moment Coefficient vs. Angle of Attack for N8 Configuration at $M_\infty = 8$	149
6.22	Normal Force Coefficient vs. Angle of Attack for VMIB Configuration at $M_\infty = 11.6$	151
6.23	Pitching Moment Coefficient vs. Angle of Attack for VMIB Configuration at $M_\infty = 11.6$	152
6.24	Normal Force Coefficient vs. Angle of Attack for MIB Configuration at $M_\infty = 11.6$	153
6.25	Pitching Moment Coefficient vs. Angle of Attack for MIB Configuration at $M_\infty = 11.6$	154
6.26	Pitch Center of Pressure vs. Angle of Attack for VMIB and MIB Configurations at $M_\infty = 11.6$	155

NOMENCLATURE

a	isentropic speed of sound
a_k	stretching coefficient in $\phi = \phi_k$ plane
A_B	vehicle base area, πR_B^2
$b(\xi, \theta)$	body surface in (ξ, η, θ) space
$c(\xi, \theta, \tau)$	bow shock surface in (ξ, η, θ) space
C_N	normal force coefficient, $F_N/q_\infty A_B$
C_m	pitching moment coefficient, $M_z/q_\infty A_B L$
\bar{c}	$\cos(-\omega)$
d	shock layer thickness
e	total energy per unit volume
F_N	normal force
g	$\partial \tau / \partial z _{\phi = \text{constant}}$
g_j	$\partial z_{j+1} / \partial z_j _{\phi = \text{constant}}$
G	$ g $
h	static enthalpy, or altitude
$h_{i,j,k}$	hinge point i in j^{th} transformed plane in $\phi = \phi_k$ plane
H	total enthalpy
i	$\sqrt{-1}$
$\hat{i}, \hat{j}, \hat{k}$	unit vectors in (ξ, η, θ) space
$\hat{i}, \hat{j}, \hat{R}$	unit vectors in (x, y, ϕ) space
L	reference length
L_A	vehicle length, measured from virtual apex
M	Mach number
M_z	pitching moment
\hat{n}	unit normal vector
p	pressure

P_0	stagnation pressure
P	logarithm of pressure
q	dynamic pressure, $1/2\rho V^2$
R	gas constant
R_B	vehicle base radius
R_N	vehicle nose radius
Re	Reynolds number
\bar{s}	entropy
s	non-dimensional entropy, \bar{s}/R
\tilde{S}	$\sin(-\omega)$
t	time coordinate in (x,y,ϕ) frame
T	time coordinate in (X,Y,Z) frame
U,V,W	velocity components in (x,y,ϕ) space
u,v,w	velocity components in (ξ,η,θ) space
\tilde{u}	normal velocity component
\vec{V}	velocity vector
V	magnitude of velocity vector
\tilde{v}	tangential velocity component
W	shock velocity
x,y,ϕ	cylindrical coordinates in physical space
x_1,x_2,x_3	Cartesian coordinates at centerline
X,Y,Z	computational coordinates
x_{cg}	moment reference point
x_{cp}	pitch center of pressure location
z_k	$x+iy$ in $\phi = \phi_k$ plane
$z_{j,k}$	image of z_k in j^{th} transformed plane
α,β,γ	damping coefficients for conservation calculations

α	angle of attack
α_T	trim angle of attack
β	sideslip angle
γ	isentropic exponent
δ	boundary layer thickness
$\delta_{j,k}$	exponent for j^{th} conformal transformation in $\phi = \phi_k$ plane
Δ_0	bow shock stand-off distance
ζ_k	$\xi + i\eta$ in $\phi = \phi_k$ plane
θ_b	body slope
λ	characteristic slope
μ	viscosity
ξ, η, θ	coordinates in transformed space
$\xi_L(\theta)$	downstream boundary of computational region in transformed space
ρ	density
σ	shock slope
τ	time coordinate in (ξ, η, θ) frame
ϕ	$\phi_1 + i\phi_2 = \partial(\log g)/\partial\zeta _{\phi = \text{constant}}$
ω	$\arg(g)$
$()_b$	quantity at body surface
$()_s$	quantity at bow shock
$()_\infty$	freestream quantity

SECTION 1
INTRODUCTION

Current research efforts in ballistic reentry vehicle aerodynamics are primarily concerned with the improvement of vehicle targeting accuracy. Accurate evaluation of possible targeting errors requires a detailed understanding of all mechanisms that may deflect the vehicle away from its nominal ballistic trajectory. Of the dispersion errors that can be attributed directly to the reentry vehicle, the low altitude roll-trim effect is one of the prime contributors to miss distance.

Roll-trim dispersion results when normal forces, such as created by a trim angle of attack condition, are not integrated out by the spin of the vehicle. The characterization of such dispersion requires a coupling of the vehicle's dynamics with its aerodynamic characteristics along the entire entry trajectory. This effort is aimed at extending current aerodynamic prediction capabilities relative to the low altitude roll-trim dispersion problem.

The current generation of ballistic reentry vehicles are typically slender blunted cones or biconic configurations, with the nosetips generally being fabricated from woven carbonaceous materials. During reentry the severity of the aerothermodynamic environment causes ablation of the nosetip material, leading to both axial recession of the nosetip and to alterations in the basic shape of the nose.

At higher altitudes ($100 \text{ KFT} \geq h \geq 50 \text{ KFT}$) the flow in the nosetip boundary layer remains laminar, resulting primarily in blunting of the nosetip. Below approximately 50 KFT, however, as the nosetip boundary layer is passing through transition to a fully turbulent

state, the increased heating levels lead to a sharpening of the nosetip shape, as illustrated in Figure 1.1.

Because of circumferential variations in the onset and progression of nosetip transition, asymmetric nose geometries can result. The mechanisms governing this transition process, such as surface roughness variations, are generally evaluated statistically, as by Dirling¹.

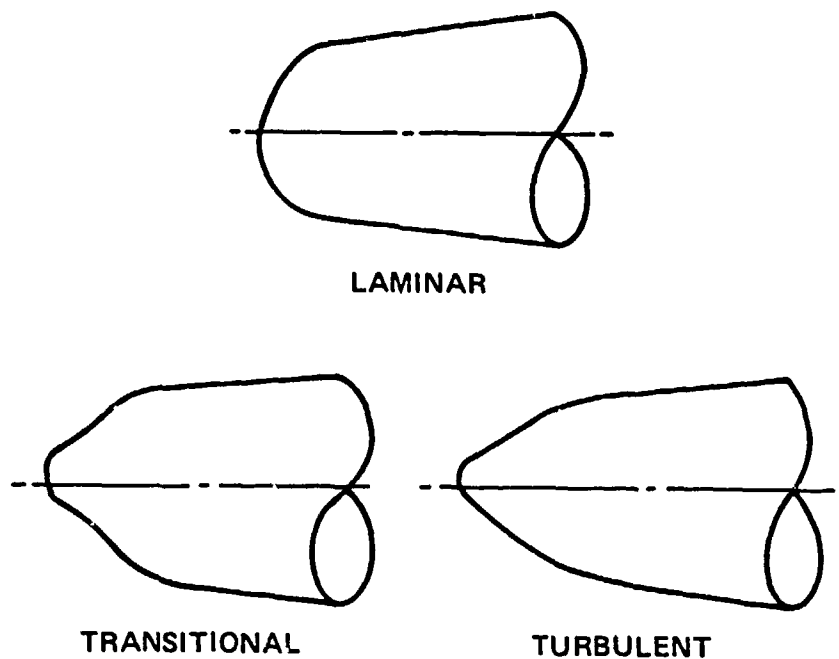


Figure 1.1. Typical Nose Shape Progression

The development of an asymmetric nosetip shape on an otherwise axisymmetric body will lead to the development of a trim angle of attack and corresponding side forces which tend to deflect the vehicle from its ballistic trajectory. To minimize these trim effects, reentry vehicles are spun prior to their reentering the atmosphere; thus the integrated resultant of a body-fixed lift force over one revolution of the body will be nearly zero. However, rapid variations in nose shape and angle of attack (and hence lift force) and roll rate can result in a non-zero resultant force, leading to trajectory deflection due to roll-trim dispersion.

Because of the inherent uncertainties in nose shape change predictions, the roll-trim effect is usually evaluated statistically, as by Pettus, Larmour, and Palmer². Given a nose shape, however, the evaluation of aerodynamic characteristics, a necessary part of any roll-trim evaluation, is a deterministic problem.

Aside from expensive and time-consuming wind tunnel tests, the most accurate and reliable method for the prediction of aerodynamic characteristics is the numerical integration of the inviscid equations of fluid motion. Fortunately, at the flight conditions of interest (and in most hypersonic wind tunnels simulating reentry conditions at low altitudes) the Reynolds number is sufficiently large that the shock layer is almost entirely inviscid, except for the thin boundary layer adjacent to the vehicle surface. Additionally, the flow is in the weak interaction regime, as defined in Hayes and Probstein³, where viscous shear and induced pressure effects significantly affect only the axial force experienced by the vehicle. Other vehicle forces and moments (normal and side forces, pitching and yawing moments) can then be

accurately determined solely through consideration of the inviscid pressure distribution.

In the past decade many numerical procedures have been developed for the calculation of inviscid aerodynamic characteristics for ballistic reentry vehicles. These techniques have proven to be valuable adjuncts to the design process and have, to some extent, lessened the need of performing extensive wind tunnel tests to validate proposed configurations. The three-dimensional numerical procedures currently in use consist of two parts: a transonic flow field procedure to treat the subsonic region surrounding the stagnation point, and an afterbody procedure to treat the the supersonic flow on the vehicle frustum.

The inviscid afterbody flow field problem is now well in hand for the simple axisymmetric frusta found on ballistic reentry vehicles. (In addition, ballistic vehicles at low altitudes generally do not develop large angles of attack which would lead to flow separation on the leeside of the afterbody, invalidating the inviscid assumption.) The existing inviscid transonic nosetip flow field capability is restricted, however, to convex shapes, where strong embedded shock waves, such as shown in the Schlieren photograph in Figure 1.2, do not occur. Furthermore, other restrictions arise even for convex shapes, when the coordinate system used in the calculation is not closely aligned with the surface of the nosetip. (These shortcomings of the current techniques were identified by Hall, Kyriakos, Truncellito, and Martellucci⁴.)



Figure 1.2. Schlieren Photograph of Ablated Nosetip with Embedded Shock

The goal of the current research effort is to eliminate the above two restrictions on inviscid transonic flow field techniques. By extending the range of nosetip shapes that can be analyzed numerically to include slender and indented shapes, such as have been observed in flight, the capability for accurate evaluation of roll-trim dispersion will be greatly expanded. In addition this new capability will allow more accurate nose shape reconstruction efforts (in which a nose shape is sought that produces aerodynamic characteristics that agree with those derived from the vehicle motion observed in flight), as described by Hall and Nowlan⁵. Furthermore, this transonic flow field technique will be applicable to maneuvering as well as ballistic reentry vehicles, since autopilot design for maneuvering vehicles must account for the aerodynamic characteristics that result from ablated nosetip geometries.

The approach taken to eliminate these deficiencies of the current nosetip flow field procedures is outlined in Section 2.2. Section 3.0 details the conformal mapping transformation used to produce a coordinate system closely aligned with the body surface, and Section 4.0 describes the procedures used for the calculation of embedded shocks. In Section 5.0, details are provided on the numerical procedures used in this new transonic flow field technique, which is validated by comparisons to data in Section 6.0.

SECTION 2

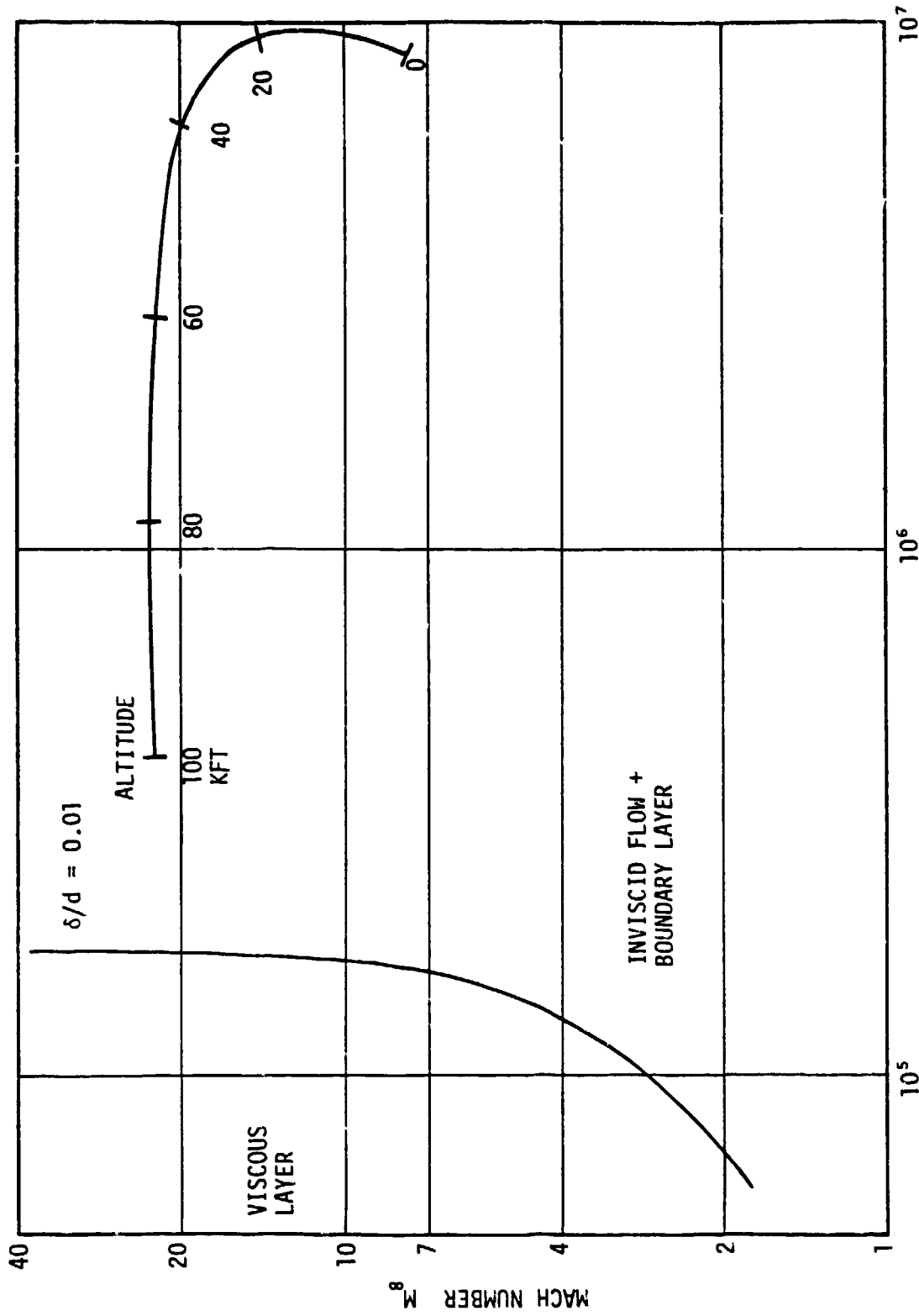
PROBLEM DEFINITION

2.1 STATEMENT OF THE PROBLEM

The problem being examined in this research effort involves the numerical prediction of the inviscid aerodynamic characteristics of ballistic reentry vehicles with asymmetric, ablated nosetips. In particular, emphasis is placed on the development of a numerical technique to determine the inviscid flow field about a three-dimensional, asymmetric nosetip in a uniform hypersonic or supersonic freestream flow. The determination of the nosetip flow field is a necessary first step for the prediction of total vehicle aerodynamics.

The assumption is made in this analysis that inviscid flow theory is adequate to accurately predict the aerodynamic characteristics of reentry vehicles at altitudes where asymmetric nose shapes can result from ablation ($h \leq 50$ KFT). (Accurate calculation of drag forces will also require consideration of surface shear and induced pressure effects, however.) Implicit in the assumption of inviscid flow are the requirements that the thin boundary layer assumption be valid and that no regions of separated flow exist on the vehicle.

Moretti and Salas⁶, in their analysis of viscous rarefied flows, have presented a breakdown of the various flow regimes that might be expected as a function of freestream Mach and Reynolds numbers (with the Reynolds number based on nosetip radius for a spherical nose), as depicted in Figure 2.1. Also indicated in this figure is an $M_\infty - Re_\infty$ history for a typical modern ballistic reentry vehicle as a function of altitude. Defining the thin boundary layer regime as the region where



REYNOLDS NUMBER $Re_\infty = V_\infty \rho_\infty R_N / \mu_\infty$

FIGURE 2.1. Re_∞ - M_∞ MAP OF FLOW REGIMES WITH TYPICAL REENTRY VEHICLE TRAJECTORY SUPERIMPOSED

the boundary layer thickness (δ) is less than 1% of the shock layer thickness (d), this figure clearly indicates the validity of the inviscid assumption for the problem being considered here.

The hypersonic flow over a blunt nosetip is characterized by a detached bow shock wave separating the shock layer from the undisturbed freestream flow. In the vicinity of the stagnation point, where the bow shock is nearly normal to the freestream velocity vector, the flow in the shock layer is locally subsonic; thus, the steady flow problem in this region has an elliptic character. As the bow shock curves back around the body and becomes more oblique to the freestream velocity vector, and as the shock layer flow expands around the nose, the flow becomes locally supersonic, and the steady flow problem becomes hyperbolic. Other complications can arise in this basic inviscid flow field structure if the body surface has indented regions producing embedded shock waves. Depending on the shock strength, the flow behind such an embedded shock could be either subsonic or supersonic.

Because of this variety of flow conditions that can be encountered in the blunt body problem, it is convenient to seek the steady solution as the asymptotic limit of the time-dependent problem, since the unsteady flow equations are hyperbolic in time, regardless of the local Mach number. Furthermore, since the location of the bow shock wave is unknown a priori and must be determined as part of the solution procedure, this time-asymptotic approach has the additional benefit of allowing the calculation of the time history of the shock shape starting from an assumed initial shock position.

The numerical procedure to be used in the solution of this time-dependent problem is an explicit, second-order accurate finite-

difference procedure. Similar schemes have been developed previously, and are currently in wide use; however, these procedures are limited in their ability to treat slender ablated nosetip shapes, and in their ability to treat embedded shocks. This research effort is devoted to the development of a procedure that eliminates the deficiencies observed in other transonic time-dependent codes. In particular, this requires development of a generalized coordinate system that is capable of being closely aligned with the three-dimensional body surface for arbitrary body geometries, as well as the development of a procedure for the calculation of three-dimensional embedded shocks on indented nosetip shapes.

Coupling this nosetip transonic procedure to an existing supersonic afterbody code will thus allow accurate theoretical assessment of the effect of ablated nosetip geometries on the performance of the total vehicle for many nose shapes that could not previously be analyzed.

2.2 OUTLINE OF APPROACH

The fundamental approach selected in this research effort for the solution of the blunt body problem for ablated asymmetric nosetips is the time-dependent relaxation approach. This technique has been widely used in previous work and has several advantages directly related to difficulties associated with the blunt body problem. In particular, the time-dependent approach allows the use of a convenient forward-marching (in time) numerical algorithm, avoiding many of the difficulties otherwise encountered in the steady flow problem.

The numerical scheme selected for this analysis is in many ways similar to that used in other procedures. For example, the treatment of

field points in this algorithm (when no embedded shocks are present) is based on the second-order accurate explicit MacCormack⁷ predictor-corrector finite differencing scheme. This particular scheme has found wide application to computational fluid dynamics problems (e.g., References 8, 9, 10, 11, 12) because of its high degree of accuracy and ease of implementation. Boundary points at the body surface and at the outer (bow) shock are treated using the Kentzer-Moretti predictor-corrector boundary point procedure, in which a discretization of boundary conditions suggested by Kentzer¹³ was extended to a predictor-corrector format by Moretti and Pandolfi⁹. This boundary point procedure has found wide application in computational fluid dynamics, and its properties have been analyzed and discussed by Hall¹⁴.

A conformal mapping technique was selected to define the coordinate system for this problem because of its ability to preserve local angles under the transformation. Thus, by formulating a mapping in which the image of the body surface is a nearly horizontal line, and selecting another coordinate direction to be the vertical direction in the transformed space (and hence nearly normal to the body image), the resulting grid in physical space will consist of surfaces closely aligned with and nearly normal to the body surface. The ability to automatically generate such a coordinate system for ablated asymmetric nosetip shapes is critical to the success of the numerical algorithm in computing inviscid flows about such shapes.

The coordinate system developed in this research is based on the "hinge point" concept of Moretti, as developed in References 15, 16, and 17. Application of this technique to the asymmetric nosetip problem

has required the extension of this technique to three dimensions; this development is described in Section 3.2.

To treat the embedded shock problem in this research effort, the shock-capturing approach has been selected, in which the structure of the embedded shock is approximated, but for which no special logic is required to explicitly treat the shock. Two shock-capturing approaches are examined: the conservation formulation, discussed in Section 4.1, and the λ -differencing approach, discussed in Section 4.2. Axisymmetric versions of both of these techniques have been developed, and a comparison of the results of these two approaches is made in Section 4.3. Based on these comparisons, it is concluded that the λ -differencing approach is the superior method, and, accordingly, is extended to three-dimensions in Section 4.4.

Axisymmetric, inviscid, time-dependent procedures with a shock-capturing approach to the treatment of embedded shocks have, of course, been developed previously, notably by Kutler, Chakravarthy, and Lombard¹⁸ (using the conservation form) and by Moretti¹⁹ (using the λ -differencing approach). The successful application of the λ -shock-capturing technique to the three-dimensional time-dependent embedded shock problem is, however, new.

The final portion of this effort is devoted to the validation of the resulting numerical technique for the calculation of inviscid nose-tip flow fields. For simple nosetip shapes (e.g., spheres) this new technique is compared to proven flow field codes, such as that developed by Kyriss and Harris⁸. For other shapes, representative of nosetip shapes that result from the ablation process, comparisons are made with wind

tunnel measurements of surface pressure and bow shock shape. Unfortunately, most of the existing wind tunnel data providing these details on nosetip flows are available only for axisymmetric shapes, as in Reeves, Todisco, Lin, and Pallone²⁰ and Jackson and Baker²¹.

A large body of wind tunnel data does exist for the total aerodynamics of reentry vehicles with asymmetric nosetips. Coupling the new nosetip flow field procedure to an existing afterbody code, comparisons are made between predicted and measured vehicle forces and moments, thus providing an indirect means of verifying the accuracy of the nosetip calculation. These comparisons are presented in Section 6.4.

SECTION 3 COORDINATE SYSTEM AND GOVERNING EQUATIONS

This section provides details on the coordinate transformation developed in this effort that is capable of mapping the surface of ablated, asymmetric nosetip geometries onto a nearly horizontal surface, thus producing a coordinate grid closely aligned with the body geometry. This mapping is then used to generate the three-dimensional inviscid time-dependent equations of fluid motion written in terms of the new coordinates. A final computational transformation is described that maps the transformed shock layer onto a regular, equally spaced grid.

The equations derived in this section are written in non-conservation form; i.e., the dependent variables are the primary flow variables. This form of the governing equations is the form used for flow calculations when embedded shocks are not present, and as the basis of the λ -differencing shock-capturing scheme described in Section 4.2. The conservation form of the governing equations is discussed in Section 4.1.

3.1 INVISCID EQUATIONS OF MOTION

The three-dimensional time-dependent inviscid equations of motion in non-conservation form may be written in cylindrical coordinates as

$$P_t + UP_x + VP_y + WP_\phi/y + \gamma(U_x + V_y + W_\phi/y + V/y) = 0 \quad (3.1)$$

$$U_t + UU_x + VU_y + WU_\phi/y + pP_x/\rho = 0 \quad (3.2)$$

$$V_t + UV_x + VV_y + WV_\phi/y - W^2/y + pP_y/\rho = 0 \quad (3.3)$$

$$W_t + UW_x + VW_y + WW_\phi/y + VW/y + pP_\phi/\rho y = 0 \quad (3.4)$$

$$s_t + Us_x + Vs_y + Ws_\phi/y = 0 \quad (3.5)$$

where

$$\vec{V} = U\hat{I} + V\hat{J} + W\hat{K}$$

with \hat{I} , \hat{J} , and \hat{K} being the unit vectors in the x, y, and ϕ directions, respectively. (In this cylindrical system, x is the axial, y the radial, and ϕ the circumferential coordinate.) In this formulation the dependent thermodynamic variables are P and s, where

$$P = \rho n p \quad (3.6)$$

and s is some suitable analog of the entropy. The choice of P as a dependent variable is motivated by computational considerations, since the logarithm of pressure throughout the shock layer will not vary by several orders of magnitude as the pressure might; thus, one can expect more accurate finite difference representations of derivatives of P than could be expected for p.

For closure of this system of partial differential equations, a thermodynamic equation of state of the form

$$\rho = \rho(p,s) \quad (3.7)$$

is required. For an equilibrium real gas calculation, the relation embodied in Equation (3.7) may be provided either through tabulations of the thermodynamic properties or through an appropriate curve fit of the thermodynamic data. In the case of a thermally and calorically perfect (ideal) gas, this thermodynamic relation may be expressed implicitly as

$$s = (\ln p - \gamma \ln \rho) / (\gamma - 1) \quad (3.8)$$

where the thermodynamic variable s is defined in terms of the entropy \bar{s} as

$$s = (\bar{s} - \bar{s}_\infty) / R \quad (3.9)$$

with γ the isentropic exponent and R the gas constant. Inversion of Equation (3.8) yields

$$\rho = p^{1/\gamma} e^{\frac{1-\gamma}{\gamma} s} \quad (3.10)$$

Finally, to complete the definition of the mathematical problem, initial and boundary conditions must be specified. Since the steady-state solution is sought as the asymptotic limit of the transient problem, the specification of an initial flow field is required. Details on the definition of this assumed initial flow field are presented in Section 5.1.

Boundary conditions for this problem must be specified at the boundaries of the region being computed: at the bow shock wave $y = y_s(x, \phi)$, on the body surface $y = y_b(x, \phi)$, and on some downstream boundary, running between the body and the shock. The location of the downstream boundary is arbitrary, subject only to the restriction that the flow across this boundary be supersonic. As long as this boundary is entirely supersonic, no condition need be imposed there, since the range of influence of this boundary will then not extend back into the region being computed.

At the bow shock, whose position is unknown a priori and must be determined as part of the solution procedure, the appropriate boundary conditions are given by the familiar Rankine-Hugoniot conditions.

By incorporating differential forms of these relations for conservation of mass, momentum, and energy across the shock into a characteristic compatibility relation, an equation for the shock acceleration is obtained, which may be integrated to yield shock velocity and position. This numerical scheme is described in more detail in Section 5.4.

At the body the appropriate boundary condition to be imposed is the inviscid kinematic boundary condition, which requires that there be no velocity component normal to the body surface. This condition is applied in conjunction with a characteristic compatibility condition to develop a numerical procedure for body points as described in Section 5.3.

Also of interest in the treatment of boundary conditions for this problem is the value of entropy that applies along the streamline that wets the body surface. It is frequently assumed that the surface entropy for inviscid flows is exactly the normal shock value of entropy, but this can be proven only for axisymmetric flows. Numerical results of Swigart²² and the experimental results of Xerikos and Anderson²³ indicate that this assumption may not be true and that the normal shock streamline does not wet the body surface. However, in his survey paper, Rusanov²⁴ argues that the results of Swigart's calculations using an inverse method are inconclusive because of the inherent assumptions and computational errors. Additionally, Rusanov points out that his own computational results using a finite difference procedure produced variations between the computed surface entropy and the normal shock entropy of less than 0.1%, which is within the error level of his calculation. From the examination of his studies and the results of others, Rusanov concludes that there is no firm evidence of the surface entropy's

not having the normal shock value, although there is likewise no proof that these values coincide.

From a practical standpoint, the question of the value of the surface entropy is not critical, since even the variations in surface entropy claimed by Swigart and Xerikos and Anderson produce only small perturbations on the other flow variables (e.g., density, velocity). Accordingly, the body surface is assigned the known normal shock value of entropy in this problem.

Circumferentially, the boundary condition to be imposed in this problem is that of periodicity; i.e., the solution at $\phi = 0$ must coincide with the solution at $\phi = 2\pi$. For the case of a pitch plane of symmetry (geometric symmetry and no sideslip), the calculation need be performed only from $\phi = 0$ to $\phi = \pi$, and the circumferential boundary conditions simply require symmetry about the pitch plane.

3.2 THREE-DIMENSIONAL CONFORMAL TRANSFORMATION

A major portion of this research is devoted to the development of a generalized, three-dimensional coordinate transformation that is capable of producing a coordinate surface closely aligned with the body surface. As outlined earlier, the method that has resulted is based on an idea of Moretti's¹⁷ for axisymmetric time-dependent calculations.

The general coordinate transformation used takes the functional form

$$\xi = \xi(x, y, \phi) \quad (3.11)$$

$$\eta = \eta(x, y, \phi) \quad (3.12)$$

$$\theta = \phi \quad (3.13)$$

$$\tau = t \quad (3.14)$$

which implies that the transformation of the spatial coordinates is independent of time. Furthermore, $\phi = \text{constant}$ planes are transformed directly to $\theta = \text{constant}$ planes, thus retaining a somewhat "cylindrical" quality to the transformation.

Prior to reentry, ballistic vehicles are initially axisymmetric, and it may thus be expected that ablated asymmetric nosetip shapes that develop during reentry will retain some "axisymmetric" character. In other words, since the $\phi = \text{constant}$ planes will be normal to the vehicle surface prior to reentry, it is reasonable to expect that the simple transformation $\theta = \phi$ will lead to $\theta = \text{constant}$ planes that are nearly normal to the surface of the ablated nosetip, even though the ablated shape may not be truly axisymmetric.

Within each $\phi = \text{constant}$ plane, then, the transformation reduces to the form

$$\xi = \xi(x,y) \quad (3.15)$$

$$\eta = \eta(x,y) \quad (3.16)$$

Since it is desirable to have a coordinate grid closely aligned with the body geometry (and hence with the streamlines of the flow), a transformation is sought that closely aligns the ξ direction with the body surface (within a $\phi = \text{constant}$ plane). In order to have the η -direction normal to the ξ -direction at all points (and hence nearly normal to the body surface), a conformal transformation is sought, since under a conformal transformation, the orthogonal (x,y) grid maps onto an orthogonal (ξ,η) grid.

Conformal transformations from the $z_1 = x + iy$ space to the $\zeta = \xi + i\eta$ space can then be developed independently in each ϕ -plane. These transformations rely on the concept of "hinge points" as developed by Moretti^{15,16,17} to ensure that the ξ -direction is closely aligned with the body surface.

The concept behind this "hinge point" approach is to define a sequence of points in the z_1 space that lie close to the body surface and define an approximate equivalent body shape. A sequence of conformal transformations is then applied to map each of these hinge points in turn onto the horizontal axis; if the hinge points in the z_1 space accurately simulate the body contour, the resulting transformed contour will then be nearly horizontal (i.e., will be closely aligned with a coordinate surface).

For the mapping function developed in this research, which has been adopted by Moretti¹⁷ for axisymmetric calculations, hinge points are defined as illustrated in Figure 3.1. Let $h_{i,j,k}$ denote the i^{th} hinge point in the j^{th} transformed space ($j = 1$ is (x,y) space) in the $\phi = \phi_k$ plane. It is required that $h_{1,1,k}$ be located on the nosetip centerline outside of the body and that $h_{2,1,k}$ be located on the centerline inside the body. The remaining hinge points $h_{i,1,k}$, $i = 3,4,\dots,JC$ are selected so as to model the body contour. Note from Figure 3.1 that this specification of points produces $JA = JC - 2$ "corners" which must be eliminated by the mapping sequence to have all hinge point images on the horizontal axis (in the transformed space).

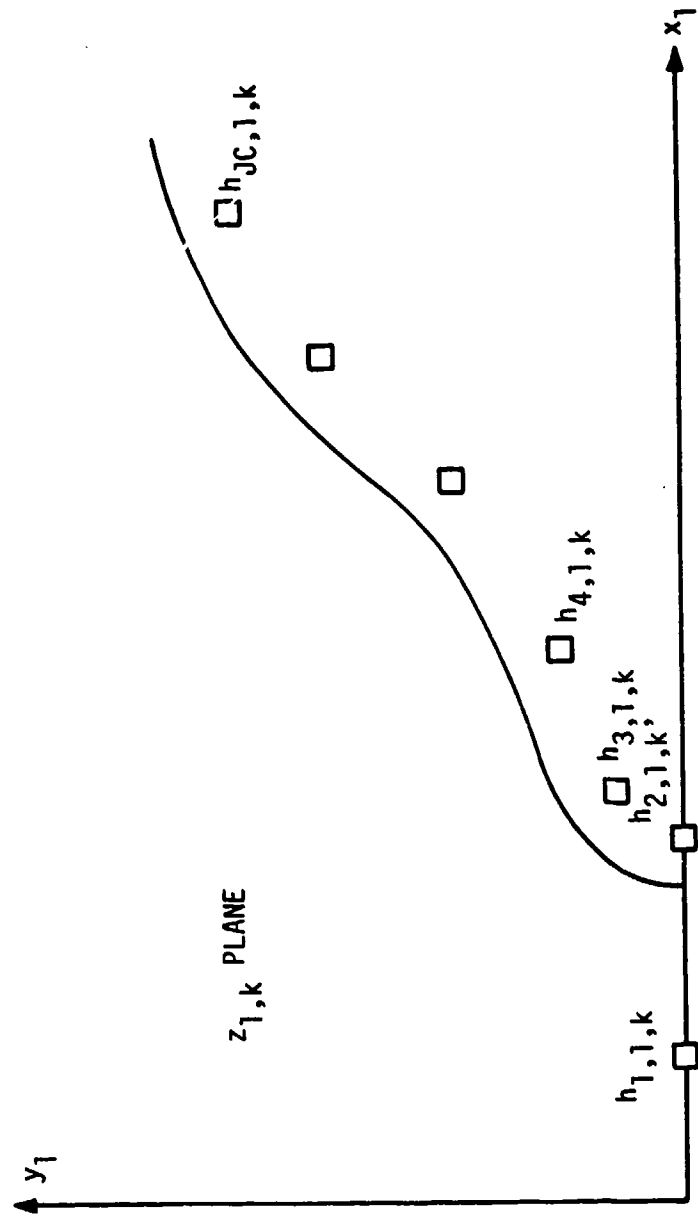


FIGURE 3.1. HINGE POINT DEFINITION

To eliminate each corner in succession, the mappings, which have been developed as part of this effort, of the form

$$z_{j+1,k} - 1 = [z_{j,k} - h_{j+1,j,k}]^{\delta_{j,k}} \quad (3.17)$$

are applied sequentially for $j = 1, 2, \dots, JA$. The form of this transformation is related to the Schwarz-Christoffel transformation and indeed may be regarded as a "point-wise" Schwarz-Christoffel transformation. By proper selection of the exponents $\delta_{j,k}$, defined from

$$\delta_{j,k} = \frac{\pi}{\pi - \tan^{-1} \frac{\operatorname{Im}[h_{j+2,j,k} - h_{j+1,j,k}]}{\operatorname{Re}[h_{j+2,j,k} - h_{j+1,j,k}]}} \quad (3.18)$$

these mappings have the required property of maintaining all hinge points $h_{i,j,k}$, $i \leq j$ on the real axis, while mapping $h_{j+1,j,k}$ onto the real axis.

The application of this mapping is illustrated in Figure 3.2, showing how each of the JA corners is eliminated successively, resulting in all $h_{i,JB,k}$ (with $JB = JA + 1 = JC - 1$) lying on the real axis in the $z_{JB,k}$ space. It is important to note that straight line segments between hinge points in the $z_{j,k}$ space are not maintained as straight segments under this sequence of transformations. Since each of these intermediate transformations is conformal, the sequence of mappings will itself be a conformal transformation.

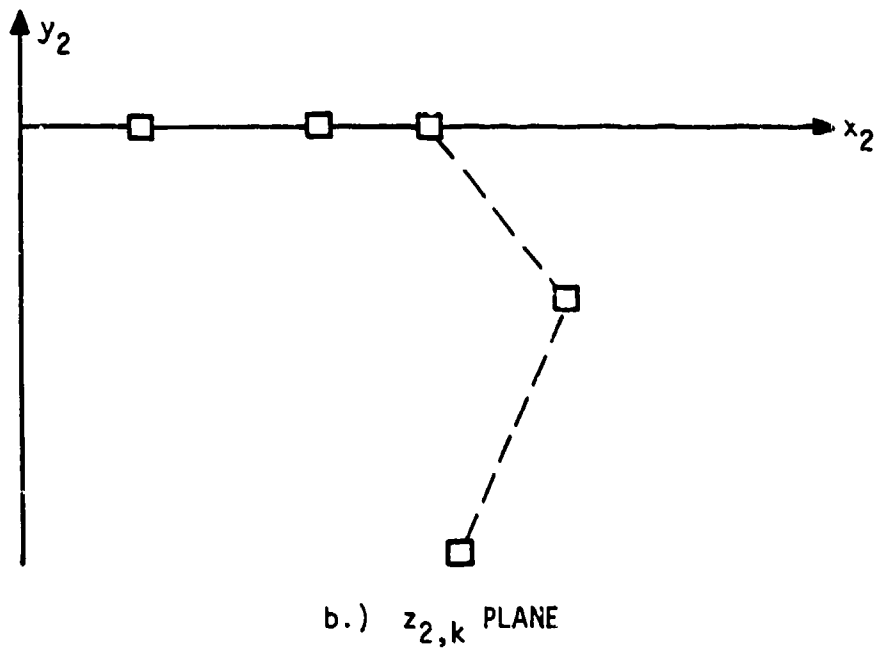
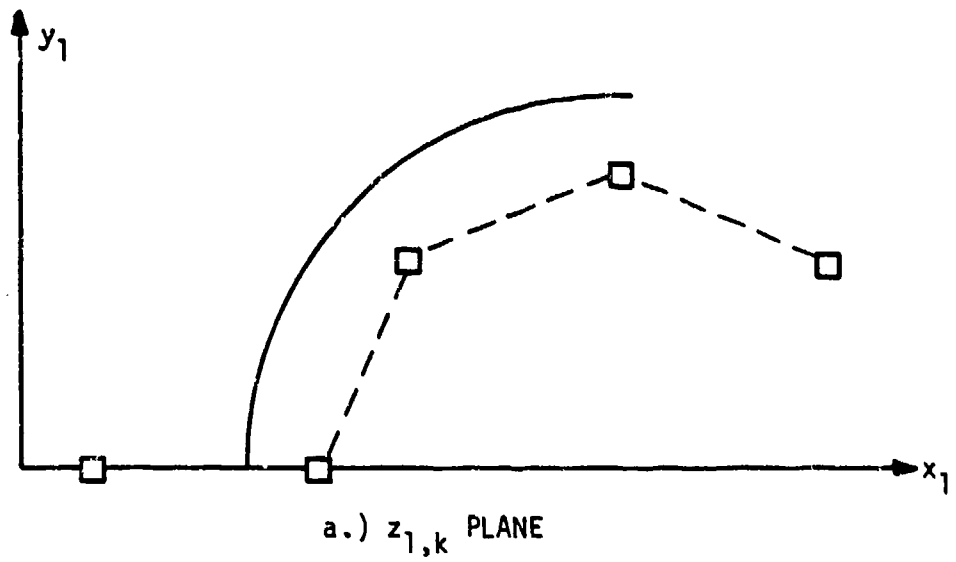
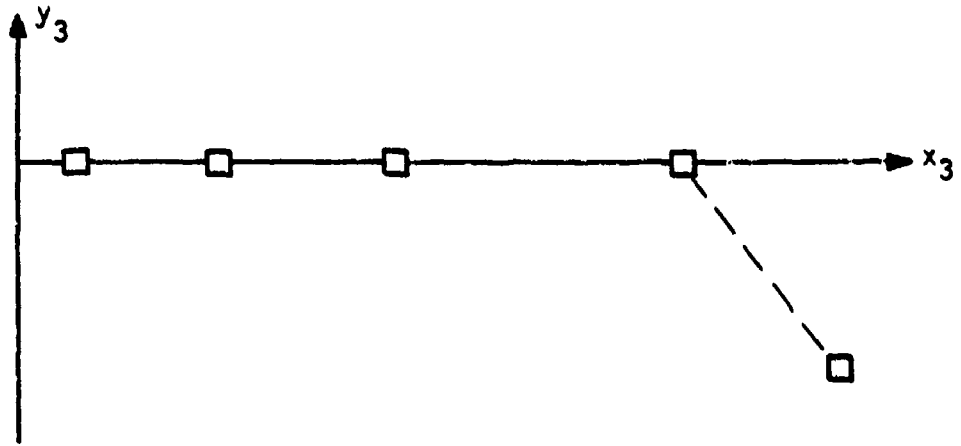
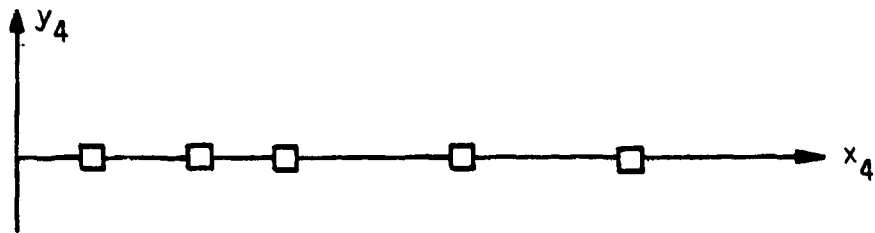


FIGURE 3.2. HINGE POINT IMAGES (SPHERE)



c.) $z_{3,k}$ PLANE



d.) $z_{4,k}$ PLANE

FIGURE 3.2. (CONTD.) HINGE POINT IMAGES (SPHERE)

Two further transformations are required to complete the specification of a suitable coordinate grid. First, it is beneficial to have the transformed body contour (which is now aligned closely with the horizontal axis in the $z_{JB,k}$ space) nearly perpendicular to the image of the centerline, which runs between $h_{1,JB,k}$ and $h_{2,JB,k}$ (and is still a straight line). Accordingly, a simple square root conformal transformation may be applied in the form

$$z_{JC,k} = (z_{JB,k} - h_{2,JB,k})^{1/2} \quad (3.19)$$

leading to the hinge point alignment shown in Figure 3.3. Also shown in this figure is the resulting body surface contour for the simple case of a sphere, using the hinge points shown in Figure 3.2.

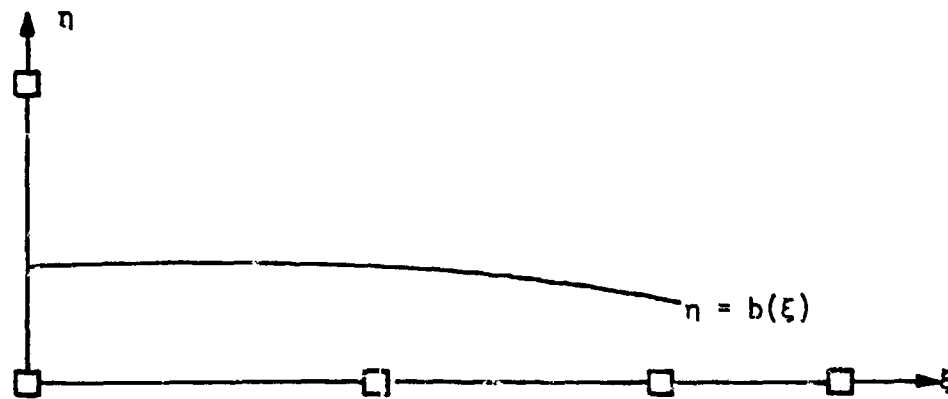


FIGURE 3.3. z PLANE HINGE POINT IMAGES AND BODY CONTOUR (SPHERE)

Because the sequence of transformations defined above is carried out independently in each $\phi = \phi_k$ plane, there is no necessary correspondence between hinge point image locations in these planes, except that $h_{2,JC,k} = 0$ and $\text{Re}(h_{1,JC,k}) = 0$ for all ϕ_k . In order to minimize the discrepancies that must arise between these mappings along the centerline (which is common to all ϕ_k planes), a final stretching is applied in each plane to ensure that the hinge point images $h_{1,JC,k}$ coincide in the $\zeta_k = \xi + i\eta$ space. This goal is attained by setting

$$\zeta_k = a_k z_{JC,k} \quad (3.20)$$

with the real coefficients a_k defined by

$$a_k = h_{1,JC,1} / h_{1,JC,k} \quad (3.21)$$

This simple scaling is itself a conformal transformation and thus preserves the orthogonal nature of the (ξ, η) grid. (Note that the (ξ, η, θ) space is not, however, necessarily orthogonal.)

It is important to note that while the final images of $h_{1,1,k}$ and $h_{2,1,k}$ have the same values in the ζ_k space that only those two points along the centerline have direct correspondence in the $z_{1,k}$ space. Because of different scale factors that arise from the independent conformal transformations in each ϕ_k plane, points with the same ζ value do not necessarily correspond to the same point in the $z_{1,k}$ planes.

Although the conformal mappings in each ϕ_k plane are defined independently, the global transformation may be considered continuous by requiring that the governing parameters of the transformation be continuous functions of ϕ and that each ϕ_k plane have the same number of hinge points (JC). In particular, this requires that the functions $a(\phi)$, $h_{2,jB}(\phi)$, $h_{j+1,j}(\phi)$, and $\delta_j(\phi)$ be continuous.

The success of this mapping sequence is illustrated in Figures 3.4 - 3.7. Shown in these figures are longitudinal nosetip profiles that are characteristics of low altitude, turbulent ablation of initially spherical carbonaceous nosetips. In each case, the hinge points used in the transformation are indicated in the z_j plane, as well as the body contours that result in the ζ plane. These figures indicate the flexibility inherent in this conformal mapping procedure, allowing any arbitrary nosetip contour to be mapped onto a nearly horizontal line. Figures 3.5 and 3.6 represent postulated axisymmetric nosetip shapes that have been tested in wind tunnels: the Very Mildly Indented Body (VMIB), as reported by Reeves, Todisco, Lin, and Pallone²⁰ (Figure 3.5) and the PANT Triconic, as reported by Jackson and Baker²¹ (Figure 3.6). Figure 3.7 represents a profile of the indented nosetip shown in the Schlieren photograph in Figure 1.2, which was recovered from a flight test.

The process of mapping the body contour onto a nearly horizontal line is relatively insensitive to the selection of hinge points, as long as the hinge points approximate the body shape in some reasonable fashion. Thus, the selection of hinge points is easily automated by spacing them at a fixed distance along inward body normals (in the (x,y) plane) from body points equally spaced in wetted length.

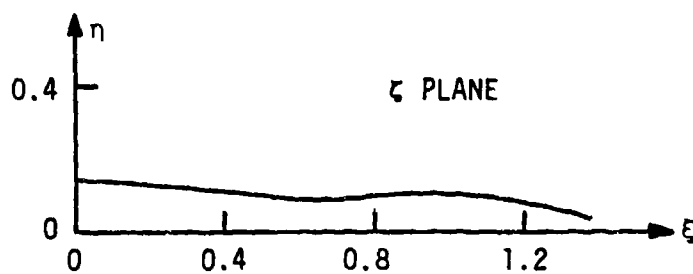
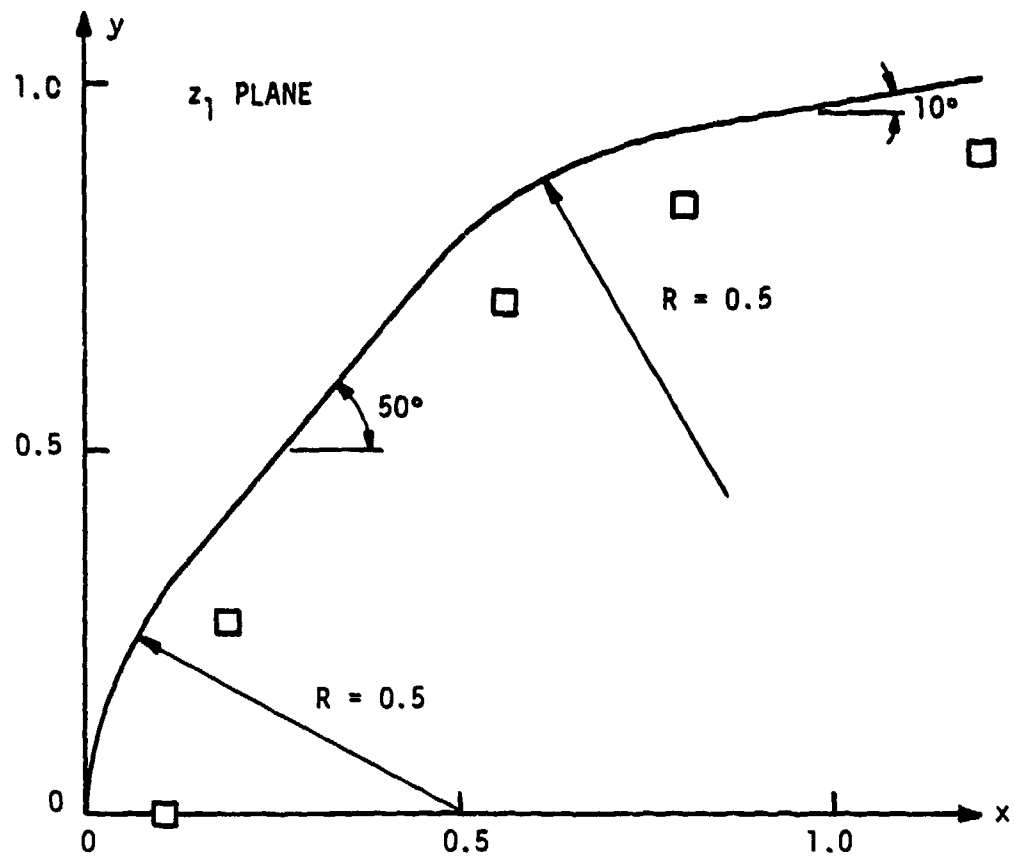


FIGURE 3.4. BODY CONTOUR IN TRANSFORMED PLANE FOR 50°/10° BICONIC NOSE

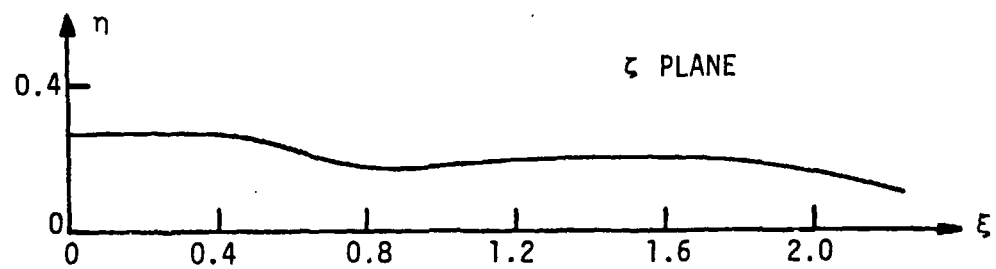
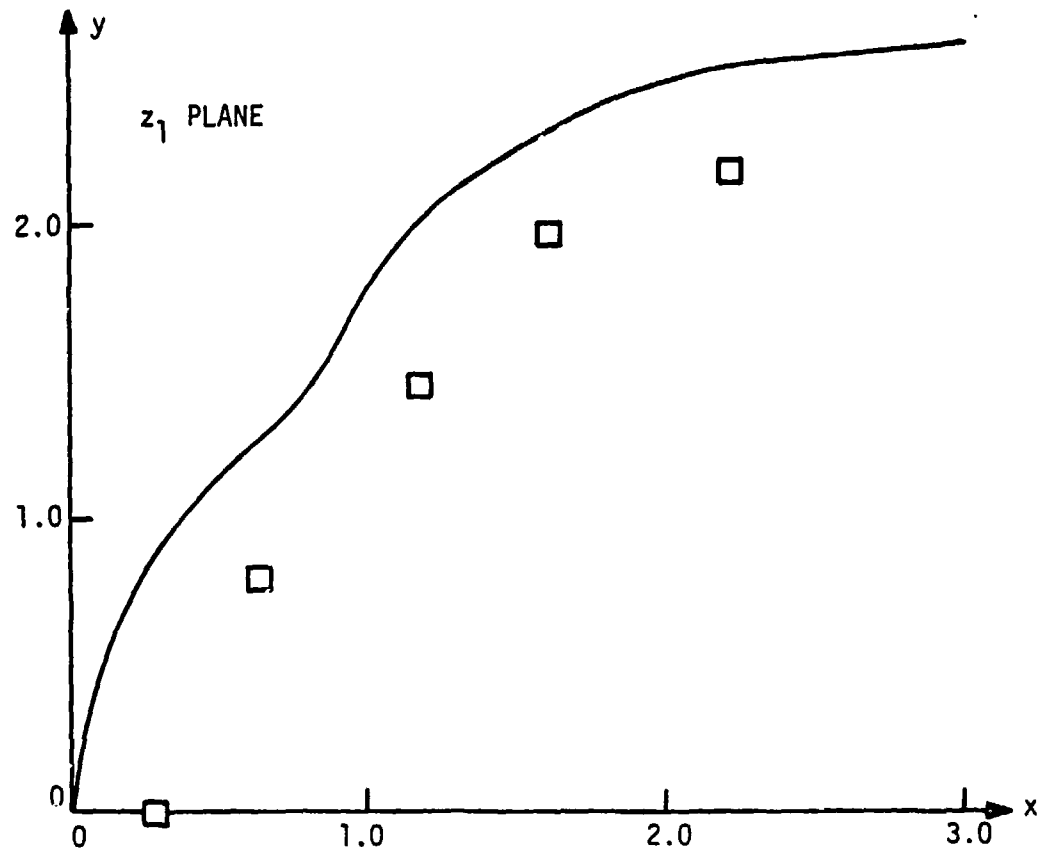


FIGURE 3.5. BODY CONTOUR IN TRANSFORMED PLANE FOR VERY MILDLY INDENTED BODY (20)

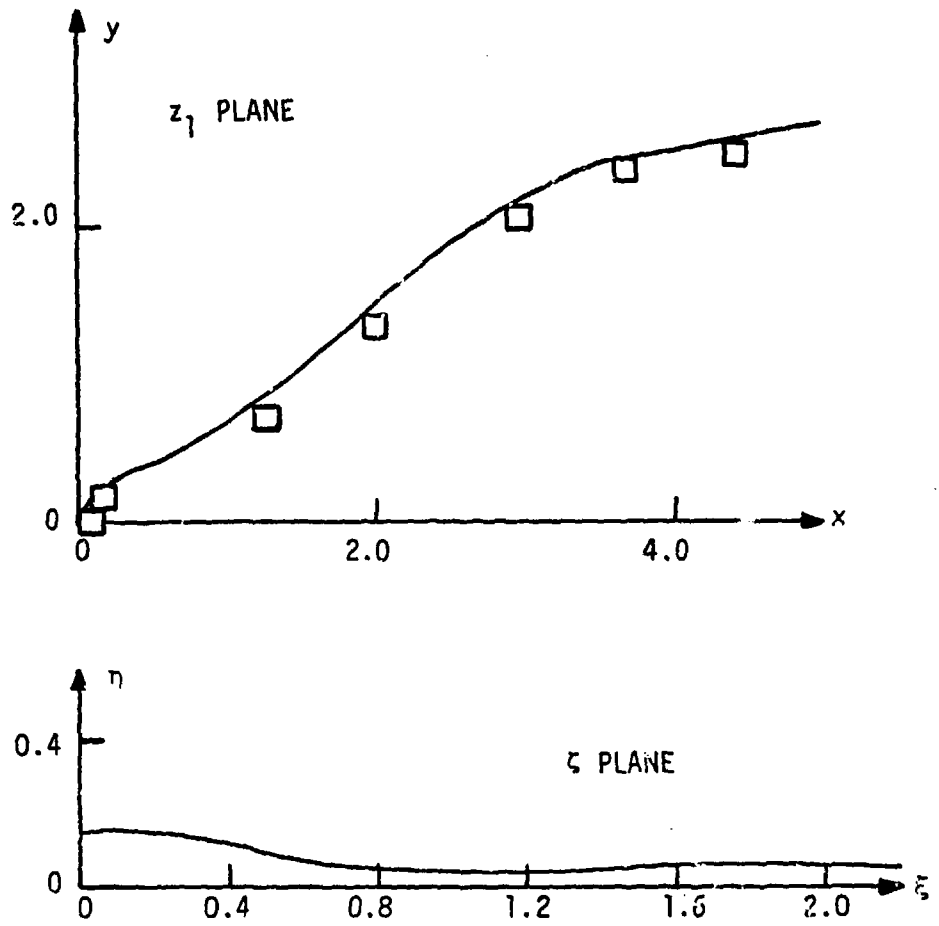


FIGURE 3.6. BODY CONTOUR IN TRANSFORMED PLANE FOR PANT TRICONIC (21)

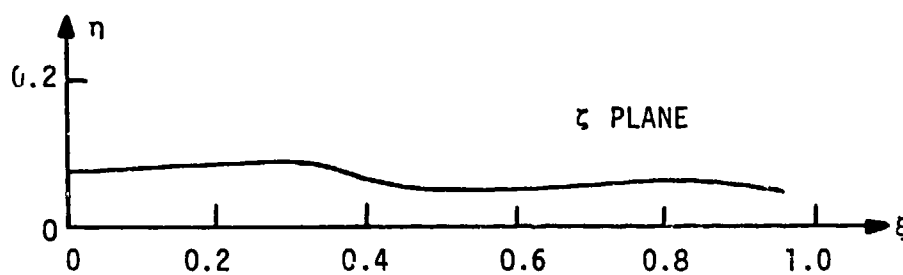
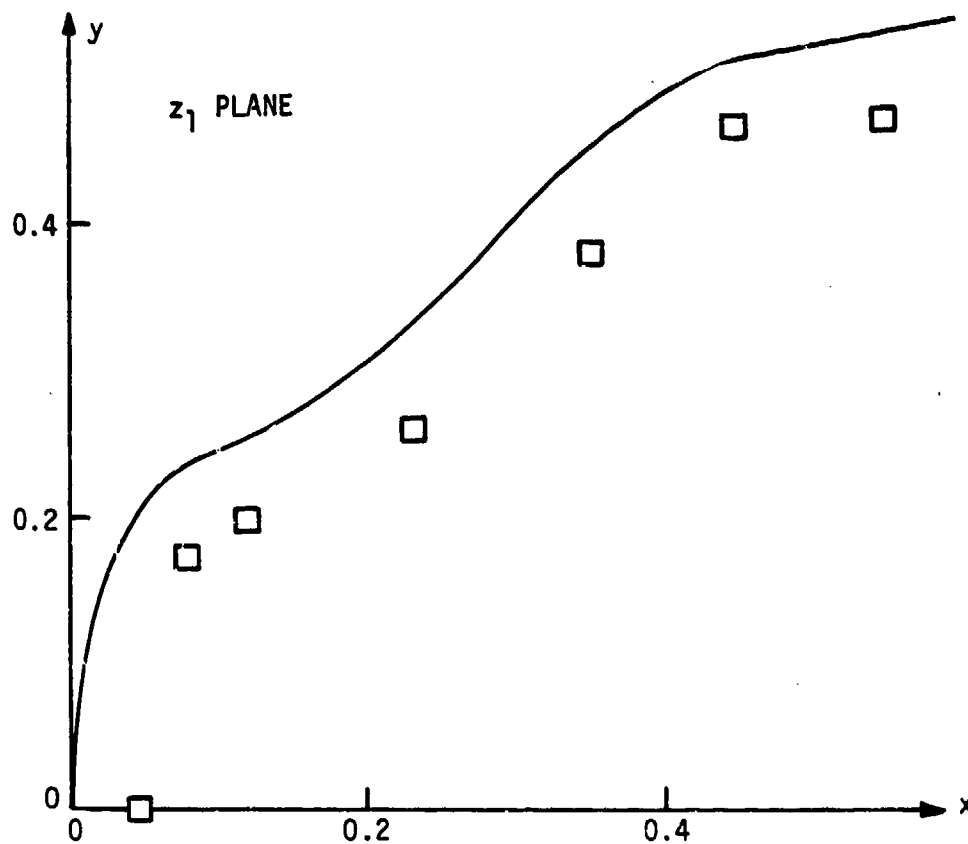


FIGURE 3.7. BODY CONTOUR IN TRANSFORMED PLANE FOR INDENTED NOSE SHAPE

3.3 TRANSFORMED EQUATIONS OF MOTION

Using the mapping from (x, y, ϕ, t) space to $(\xi, \eta, \theta, \tau)$ space described in the preceding section, the governing inviscid equations (Equations (3.1)-(3.5)) may be transformed to $(\xi, \eta, \theta, \tau)$ coordinates by application of the chain rule. Recalling the functional dependence of the transformation defined in Equations (3.11)-(3.14), the appropriate chain rules take the forms

$$\frac{\partial}{\partial t} = \frac{\partial}{\partial \tau} \quad (3.22)$$

$$\frac{\partial}{\partial x} = \xi_x \frac{\partial}{\partial \xi} + \eta_x \frac{\partial}{\partial \eta} \quad (3.23)$$

$$\frac{\partial}{\partial y} = \xi_y \frac{\partial}{\partial \xi} + \eta_y \frac{\partial}{\partial \eta} \quad (3.24)$$

$$\frac{\partial}{\partial \phi} = \xi_\phi \frac{\partial}{\partial \xi} + \eta_\phi \frac{\partial}{\partial \eta} + \frac{\partial}{\partial \theta} \quad (3.25)$$

It is convenient to define, using the notation of Moretti¹⁷,

$$g = \frac{\partial \zeta}{\partial z_1} = G e^{i\omega} = G(\tilde{C} - i\tilde{S}) \quad (3.26)$$

and

$$\phi = \frac{\partial(\log g)}{\partial \zeta} = \phi_1 + i\phi_2 \quad (3.27)$$

with

$$G = |g| \quad (3.28)$$

$$\omega = \arg(g) \quad (3.29)$$

$$\tilde{C} = \cos(-\omega) \quad (3.30)$$

$$\tilde{S} = \sin(-\omega) \quad (3.31)$$

From the definition of the conformal transformation, it follows that

$$g = a_k \left\{ \prod_{j=1}^{JA} g_j \right\} / 2z_{JC,k} \quad (3.32)$$

with

$$g_j = \delta_{jk} (z_{j+1,k} - 1) / (z_{j,k} - h_{j+1,j,k}) \quad (3.33)$$

and

$$\phi = -\frac{1}{a_k z_{JC,k}} + \frac{1}{g} \sum_{j=1}^{JA} \{g_1 g_2 \dots g_j (\delta_{j,k}^{-1}) / (z_{j,k} - h_{j+1,j,k})\} \quad (3.34)$$

With these definitions, the partial derivatives required by the chain rules are found to be

$$\xi_x = G\tilde{C} \quad (3.35)$$

$$\xi_y = G\tilde{S} \quad (3.36)$$

$$\eta_x = -G\tilde{S} \quad (3.37)$$

$$\eta_y = G\tilde{C} \quad (3.38)$$

Note that these forms verify that the mapping $\zeta = \zeta(z_1)$ in any $\phi = \text{constant}$ plane is conformal, since the Cauchy-Riemann conditions

$$\xi_x = \eta_y \quad (3.39)$$

$$\xi_y = -\eta_x \quad (3.40)$$

are satisfied.

Circumferential variations of the mappings are accounted for with the equations (derived from a Taylor series expansion)

$$\zeta_\phi = \xi_\phi + i\eta_\phi = [\zeta_2 - \zeta_1 - g(z_2 - z_1)] / (\phi_2 - \phi_1) \quad (3.41)$$

$$g_\phi = [g_2 - g_1 - g^2 \phi (z_2 - z_1)] / (\phi_2 - \phi_1) \quad (3.42)$$

where

$$\zeta_1 = \zeta(x_1, y_1, \phi_1)$$

$$\zeta_2 = \zeta(x_2, y_2, \phi_2)$$

$$g_1 = g(x_1, y_1, \phi_1)$$

$$g_2 = g(x_2, y_2, \phi_2)$$

with (x_1, y_1, ϕ_1) and (x_2, y_2, ϕ_2) representing computational grid points in surrounding ϕ planes; i.e., $\phi_1 = \phi - \Delta\phi$, $\phi_2 = \phi + \Delta\phi$.

It is convenient to write the governing equations in terms of velocity components in the (ξ, η, θ) space. Defining

$$\vec{V} = u\hat{i} + v\hat{j} + w\hat{k} \quad (3.43)$$

with \hat{i} , \hat{j} , and \hat{k} being unit vectors in the ξ, η , and θ directions, respectively, the new velocity components may be written in terms of the cylindrical velocity components (U, V, W) as

$$u = U\tilde{C} + V\tilde{S} \quad (3.44)$$

$$v = -U\tilde{S} + V\tilde{C} \quad (3.45)$$

$$w = W \quad (3.46)$$

In terms of these velocity components, the governing equations in non-conservation form may be transformed, using the chain rules defined above, to

$$\begin{aligned} \frac{DP}{D\tau} + \gamma[G(u\xi + v\eta + v\phi_2 - u\phi_1) \\ + (\xi_\phi w_\xi + \eta_\phi w_\eta + w_\theta + u\tilde{S} + v\tilde{C})/y] = 0 \end{aligned} \quad (3.47)$$

$$\begin{aligned} \frac{DU}{D\tau} + vG(v\phi_1 + u\phi_2) + vw(\xi_\phi\phi_2 + \eta_\phi\phi_1 + \omega_\theta)/y \\ - \tilde{S}w^2/y + G\rho P_\xi/\rho = 0 \end{aligned} \quad (3.48)$$

$$\begin{aligned} \frac{DV}{D\tau} - uG(v\phi_1 + u\phi_2) - uw(\xi_\phi\phi_2 + \eta_\phi\phi_1 + \omega_\theta)/y \\ - \tilde{C}w^2/y + G\rho P_\eta/\rho = 0 \end{aligned} \quad (3.49)$$

$$\frac{Dw}{D\tau} + w(u\tilde{S} + v\tilde{C})/y + p(\epsilon_\phi P_\xi + \eta_\phi P_\eta + P_\theta)/\rho y = 0 \quad (3.50)$$

$$\frac{Ds}{D\tau} = 0 \quad (3.51)$$

where

$$\begin{aligned} \frac{D}{D\tau} = \frac{\partial}{\partial\tau} + (Gu + w\epsilon_\phi/y) \frac{\partial}{\partial\xi} + (Gv + w\eta_\phi/y) \frac{\partial}{\partial\eta} \\ + w/y \frac{\partial}{\partial\theta} \end{aligned}$$

The term ω_θ can be evaluated from

$$\omega_\theta = \text{Im}\{g_\theta/g\} \quad (3.52)$$

with g_θ expressed as

$$g_\theta = g_\phi - g \phi z_\phi \quad (3.53)$$

3.4 COMPUTATIONAL TRANSFORMATION

Prior to obtaining numerical solutions of the transformed governing equations, it is convenient to perform an additional coordinate transformation to map $(\xi, \eta, \theta, \tau)$ space onto a rectangular computational space (X, Y, Z, T) , in which an equally spaced mesh can easily be established to facilitate numerical approximations of derivatives. In this computational system, the coordinate Z is selected so as to be 0 on the body surface and 1 on the outer boundary (bow shock wave) of the region of interest. Similarly, Y is defined as being 0 on the centerline and 1 at the downstream boundary of the region to be computed. X is directly proportional to the circumferential coordinate θ .

This computational transformation is described mathematically
as

$$X = \theta/2\pi \quad (3.54)$$

$$Y = \xi/\xi_L(\theta) \quad (3.55)$$

$$Z = [\eta - b(\xi, \theta)]/[c(\xi, \theta, \tau) - b(\xi, \theta)] \quad (3.56)$$

$$T = \tau \quad (3.57)$$

where the body surface is described as

$$\eta = b(\xi, \theta) \quad (3.58)$$

and the bow shock position as

$$\eta = c(\xi, \theta, \tau) \quad (3.59)$$

The downstream boundary is defined by

$$\xi = \xi_L(\theta) \quad (3.60)$$

Because the position of the bow shock varies with time during the solution of the time-dependent problem, the computational grid also varies with time, but always maintains equally spaced points between the body and bow shock (in Z).

To transform the governing equations into the computational coordinates, the following chain rules are applied:

$$\frac{\partial}{\partial \tau} = \frac{\partial}{\partial T} + Z_{,\tau} \frac{\partial}{\partial Z} \quad (3.61)$$

$$\frac{\partial}{\partial \xi} = Y_{,\xi} \frac{\partial}{\partial Y} + Z_{,\xi} \frac{\partial}{\partial Z} \quad (3.62)$$

$$\frac{\partial}{\partial \eta} = Z_{\eta} \frac{\partial}{\partial Z} \quad (3.63)$$

$$\frac{\partial}{\partial \theta} = X_{\theta} \frac{\partial}{\partial X} + Y_{\theta} \frac{\partial}{\partial Y} + Z_{\theta} \frac{\partial}{\partial Z} \quad (3.64)$$

where

$$X_{\theta} = 1/2\pi$$

$$Y_{\xi} = 1/\xi_L(\theta)$$

$$Y_{\theta} = -Y Y_{\xi} \xi_{L\theta}$$

$$Z_{\eta} = 1/[c(\xi, \theta, \tau) - b(\xi, \theta)]$$

$$Z_{\xi} = -Z_{\eta} [(1-Z)b_{\xi} + Zc_{\xi}]$$

$$Z_{\theta} = -Z_{\eta} [(1-Z)b_{\theta} + Zc_{\theta}]$$

$$Z_{\tau} = -ZZ_{\eta} c_{\tau}$$

with the body and shock slopes in the transformed space being determined from

$$b_{\xi} = (\tilde{C}y_{bx} - \tilde{S})/(\tilde{S}y_{bx} + \tilde{C}) \quad (3.65)$$

$$b_{\theta} = Gy_{b\phi}/(\tilde{S}y_{bx} + \tilde{C}) - \xi_{\phi} b_{\xi} + \eta_{\phi} \quad (3.66)$$

$$c_{\xi} = (\tilde{C}y_{sx} - \tilde{S})/(\tilde{S}y_{sx} + \tilde{C}) \quad (3.67)$$

$$c_{\theta} = Gy_{s\phi}/(\tilde{S}y_{sx} + \tilde{C}) - \xi_{\phi} c_{\xi} + \eta_{\phi} \quad (3.68)$$

Using Equations (3.54)-(3.57) to define the computational transformation and selecting equal mesh intervals in X,Y, and Z leads to points equally spaced in η (between body and shock), in ξ (along the body), and in θ (circumferentially). It is possible, however, to use stretching functions in the definitions of X,Y, and Z in order to concentrate mesh points in certain regions if so desired, while maintaining equal spacing in X,Y, and Z. For example, Moretti¹⁷ and Kutler, Chakravarthy, and Lombard¹⁸ have used such stretching functions to concentrate grid points near the body surface to facilitate viscous calculations. For the nosetip inviscid flow problem, such stretching is not deemed necessary, and the simpler definitions of X,Y, and Z, as presented above, are used.

The governing equations written in the computational space may now be expressed as

$$\begin{aligned} \frac{DP}{DT} + \gamma G[Y_{\xi}u_{\gamma} + Z_{\xi}u_Z + Z_{\eta}v_Z + E + (u\tilde{S} + v\tilde{C})/Gy] \\ + \gamma[\xi_{\phi}(Y_{\xi}w_{\gamma} + Z_{\xi}w_Z) + \eta_{\phi}Z_{\eta}w_Z + X_{\theta}w_X + Y_{\theta}w_Y \\ + Z_{\theta}w_Z]/y = 0 \end{aligned} \quad (3.69)$$

$$\frac{Du}{DT} + vGD + vwF/y - \tilde{S}w^2/y + Gp(Y_{\xi}P_{\gamma} + Z_{\xi}P_Z)/\rho = 0 \quad (3.70)$$

$$\frac{Dv}{DT} - uGD - uwF/y - \tilde{C}w^2/y + GpZ_{\eta}P_Z/\rho = 0 \quad (3.71)$$

$$\begin{aligned} \frac{Dw}{DT} + w(u\tilde{S} + v\tilde{C})/y + p[(Z_{\xi}\xi_{\phi} + Z_{\eta}\eta_{\phi} + Z_{\theta})P_Z \\ + (\xi_{\phi}Y_{\xi} + Y_{\theta})P_{\gamma} + X_{\theta}P_X]/\rho y = 0 \end{aligned} \quad (3.72)$$

$$\frac{Ds}{DT} = 0 \quad (3.73)$$

with

$$\frac{D}{DT} = \frac{\partial}{\partial T} + A \frac{\partial}{\partial Z} + B \frac{\partial}{\partial Y} + C \frac{\partial}{\partial X}$$

$$A = Z_{\tau} + (Gu + w\xi_{\phi}/y)Z_{\xi} + (Gv + w\eta_{\phi}/y)Z_{\eta} + wZ_{\theta}/y$$

$$B = (Gu + w\xi_{\phi}/y)Y_{\xi} + wY_{\theta}/y$$

$$C = wX_{\theta}/y$$

$$D = v\phi_1 + u\phi_2$$

$$E = v\phi_2 - u\phi_1$$

$$F = \xi_{\phi}\phi_2 + \eta_{\phi}\phi_1 + \omega_{\theta}$$

Typical grids (in physical space, $\phi = \text{constant}$) that result from this computational transformation are shown in Figures 3.8-3.10. (In these figures, the bow shock shape used in defining the computational region is an assumed initial bow shock shape.) For clarity in these figures, a coarser grid is shown than would actually be used in the calculation of a flow field about such bodies.

It is important to note in these figures that the $\xi = \text{constant}$ lines are indeed nearly normal to the body surface, as is expected when the image of the body contour is nearly horizontal ($\eta = \text{constant}$) and the mapping is conformal. The generation of such grids was the goal in the development of the mapping function presented here, and will greatly expand the range of nosetip shapes that can be successfully computed.

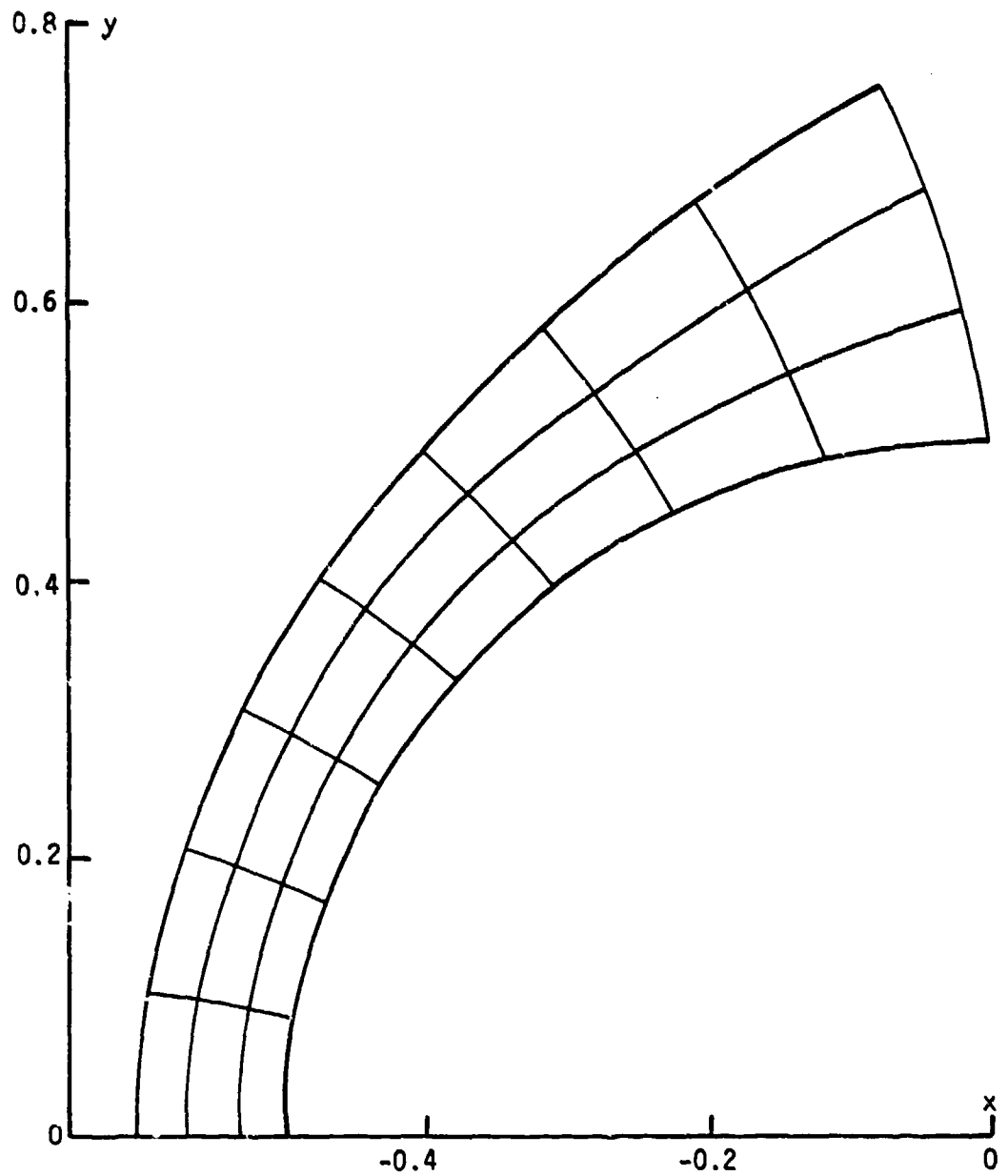


FIGURE 3.8. COMPUTATIONAL MESH FOR SPHERICAL NOSE

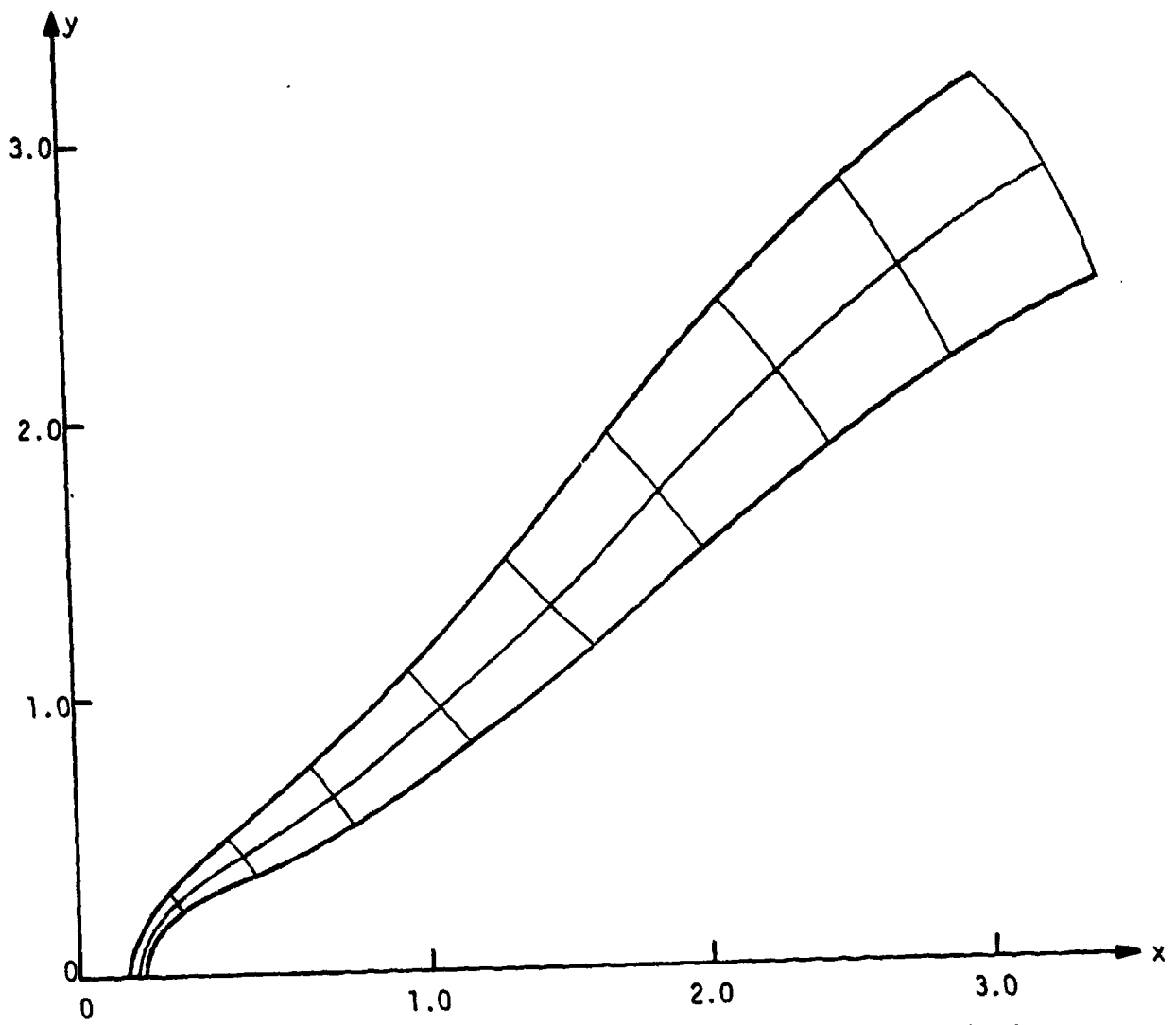


FIGURE 3.9. COMPUTATIONAL MESH FOR PANT TRICONIC (21)

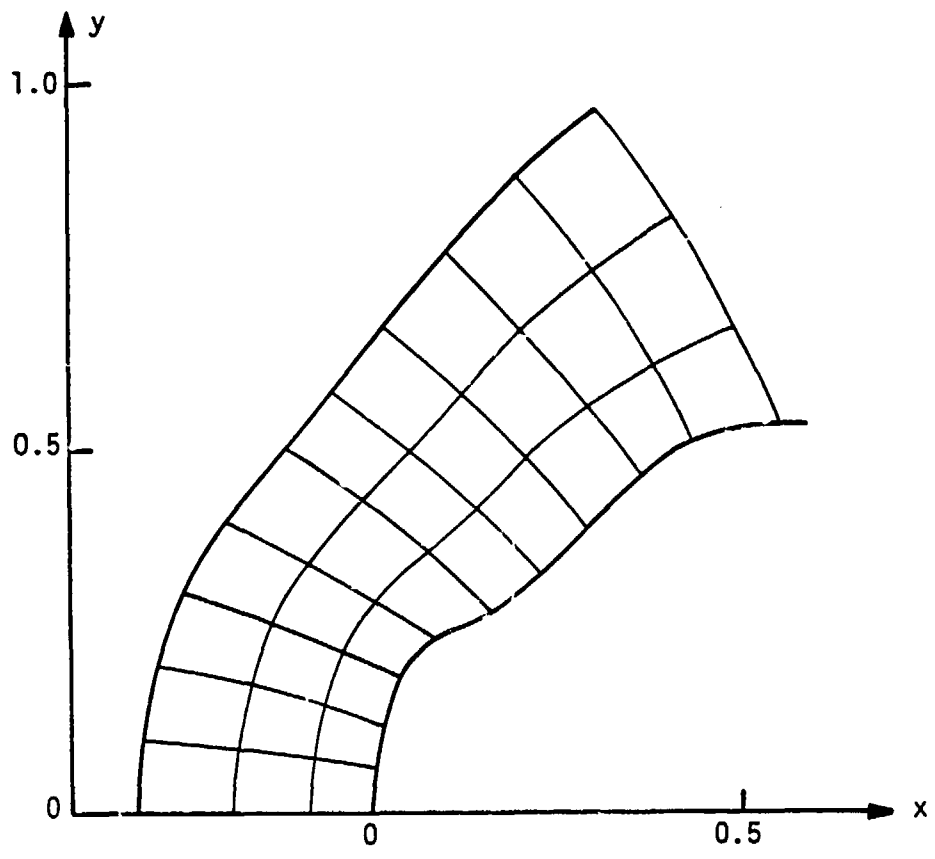


FIGURE 3.10. COMPUTATIONAL MESH FOR INDENTED NOSE SHAPE

3.5 CHARACTERISTIC RELATIONS

The numerical procedures to be used at body and bow shock points (which will be discussed in Sections 5.3 and 5.4) are based on the characteristic compatibility relations resulting from the governing system of partial differential equations, Equations (3.69)-(3.73). Accordingly, the appropriate forms of these compatibility relations at the body and bow shock are derived in this section.

In the theory of partial differential equations a characteristic surface is a surface across which the derivatives of the dependent variables may be indeterminate in the direction normal to the surface. The characteristic compatibility condition is a linear combination of the governing equations valid along this characteristic surface.

For use in this analysis, characteristics in the (Z,T) reference plane are of interest; X and Y derivatives appearing in the governing equations will be treated as forcing functions. Reduction of the four-dimensional (X,Y,Z,T) problem to two dimensions results in a characteristic curve, rather than a characteristic surface.

The governing equations may be rewritten as

$$P_T + AP_Z + \gamma G(Z_\xi u_Z + Z_\eta v_Z) + \gamma(\xi_\phi Z_\xi + \eta_\phi Z_\eta + Z_\theta)w_Z/y = R_1 \quad (3.74)$$

$$u_T + Au_Z + GpZ_\xi P_Z/\rho = R_2 \quad (3.75)$$

$$v_T + Av_Z + GpZ_\eta P_Z/\rho = R_3 \quad (3.76)$$

$$w_T + Aw_Z + p(\xi_\phi Z_\xi + \eta_\phi Z_\eta + Z_\theta)P_Z/\rho y = R_4 \quad (3.77)$$

where

$$R_1 = -[BP_Y + CP_X + \gamma G(Y_\xi u_Y + E + V/Gy) + \gamma(\xi_\phi Y_\xi w_Y + X_\theta w_X - Y_\theta w_Y)/y]$$

$$R_2 = -[Bu_Y + Cu_X + vGD + vwF/y - \tilde{S}w^2/y + GpY_\xi P_Y/\rho]$$

$$R_3 = -[Bv_Y + Cv_X - uGD - uwF/y - \tilde{C}w^2/y]$$

$$R_4 = -[Bw_Y + Cw_X + w(u\tilde{S} + v\tilde{C})/y + p\{(\xi_\phi Y_\xi + Y_\theta)P_Y + X_\theta P_X\}/\rho y]$$

(The equation for entropy convection, Equation (3.73), is not considered here, since it is known that the characteristic resulting from its inclusion is simply a streamline. While a streamline is a valid characteristic, it is not of immediate interest for this application.)

Defining the characteristic curve as

$$f(T,Z) = 0 \quad (3.78)$$

the normal to this curve is

$$\vec{N} = \nabla f = (f_T, f_Z) \quad (3.79)$$

and the characteristic slope may then be defined as

$$\lambda = -\frac{f_T}{f_Z} \quad (3.80)$$

The characteristic compatibility condition is written as a linear combination of the governing equations, where λ_1 , λ_2 , λ_3 and λ_4 are the as yet undetermined multipliers for Equations (3.74)-(3.77), respectively. Combining terms, the compatibility condition can then be written as

$$\begin{aligned} & \lambda_1 P_T + [\lambda_1 A + G\rho(\lambda_2 Z_\xi + \lambda_3 Z_\eta)/\rho + \lambda_4 \rho(\epsilon_\phi Z_\xi + \eta_\phi Z_\eta + Z_\theta)/\rho y] P_Z \\ & + \lambda_2 u_T + (\lambda_1 \gamma G Z_\xi + \lambda_2 A) u_Z + \lambda_3 v_T + (\lambda_1 \gamma G Z_\eta + \lambda_3 A) v_Z \\ & + \lambda_4 w_T + [\lambda_1 \gamma (\epsilon_\phi Z_\xi + \eta_\phi Z_\eta + Z_\theta)/y + \lambda_4 A] w_Z = \sum_{i=1}^4 \lambda_i R_i \quad (3.81) \end{aligned}$$

The terms involving derivatives of P may be regarded as a directional derivative in the direction \vec{W}_1 , where

$$\begin{aligned} \vec{W}_1 = & [\lambda_1 \{ \lambda_1 A + G\rho(\lambda_2 Z_\xi + \lambda_3 Z_\eta)/\rho + \lambda_4 \rho(\epsilon_\phi Z_\xi \\ & + \eta_\phi Z_\eta + Z_\theta)/\rho y \}] \quad (3.82) \end{aligned}$$

Similarly, derivatives of u, v, and w may also be viewed as directional derivatives in the directions \vec{W}_2 , \vec{W}_3 , and \vec{W}_4 :

$$\vec{W}_2 = [\lambda_2, \lambda_1 \gamma G Z_\xi + \lambda_2 A] \quad (3.83)$$

$$\vec{W}_3 = [\lambda_3, \lambda_1 \gamma G Z_\eta + \lambda_3 A] \quad (3.84)$$

$$\vec{W}_4 = [\lambda_4, \lambda_1 \gamma (\epsilon_\phi Z_\xi + \eta_\phi Z_\eta + Z_\theta)/y + \lambda_4 A] \quad (3.85)$$

For Equation (3.81) to be valid along the characteristic, these directional derivatives must not have any component along the direction of the normal to the characteristic curve (in which direction the derivatives may be indeterminate). These conditions may be expressed as

$$\vec{N} \cdot \vec{W}_1 = \vec{N} \cdot \vec{W}_2 = \vec{N} \cdot \vec{W}_3 = \vec{N} \cdot \vec{W}_4 = 0 \quad (3.86)$$

Noting that $\frac{\partial}{\partial T} = -\lambda \frac{\partial}{\partial Z}$, this system of equations may be written in matrix form as

$$\begin{bmatrix} A-\lambda & GpZ_{\xi}/\rho & GpZ_{\eta}/\rho & p(\xi_{\phi}Z_{\xi} + \eta_{\phi}Z_{\eta} + Z_{\theta})/\rho y \\ \gamma GZ_{\xi} & A-\lambda & 0 & 0 \\ \gamma GZ_{\eta} & 0 & A-\lambda & 0 \\ \gamma(\xi_{\phi}Z_{\xi} + \eta_{\phi}Z_{\eta} + Z_{\theta})/y & 0 & 0 & A-\lambda \end{bmatrix} \begin{Bmatrix} x_1 \\ x_2 \\ x_3 \\ x_4 \end{Bmatrix} = \vec{0} \quad (3.87)$$

For a solution to this system of homogeneous equations to exist, it is necessary that the determinant of the coefficient matrix vanish. Furthermore, any one of the four unknowns may be scaled arbitrarily. Expansion of the determinant results in the following algebraic equation:

$$(A-\lambda)^2 [(A-\lambda)^2 - a^2 G^2 Z_{\xi}^2 - \eta^2 G^2 Z_{\eta}^2 - a^2 (\xi_{\phi} Z_{\xi} + \eta_{\phi} Z_{\eta} + Z_{\theta})^2 / y^2] = 0 \quad (3.88)$$

where the isentropic speed of sound is defined from

$$a = (\gamma p / \rho)^{1/2} \quad (3.89)$$

The four roots to this equation are

$$\lambda = A \text{ (redundant root)} \quad (3.90)$$

and

$$\lambda = A \pm a [G^2(Z_\xi^2 + Z_\eta^2) + \frac{1}{y^2} (\xi_\phi Z_\xi + \eta_\phi Z_\eta + Z_\theta)^2]^{1/2} \quad (3.91)$$

The redundant root $\lambda = A$ simply shows that streamlines are characteristic directions, but, as stated earlier, this relation is not of immediate interest. Thus, the characteristic slopes being sought are those defined by Equation (3.91).

To evaluate the unknown multipliers λ_i , it is convenient to select $\lambda_1 = 1$; it then follows that

$$\lambda_2 = \gamma G Z_\xi / (\lambda - A) \quad (3.92)$$

$$\lambda_3 = \gamma G Z_\eta / (\lambda - A) \quad (3.93)$$

$$\lambda_4 = \gamma (\xi_\phi Z_\xi + \eta_\phi Z_\eta + Z_\theta) / (\lambda - A) y \quad (3.94)$$

The compatibility condition will then take the final form

$$P_T + \lambda P_Z + \lambda_2 (u_T + \lambda u_Z) + \lambda_3 (v_T + \lambda v_Z) + \lambda_4 (w_T + \lambda w_Z) = \sum_{i=1}^4 \lambda_i R_i \quad (3.95)$$

To derive forms of this relation valid at the body, it is first necessary to write the kinematic boundary condition in (ξ, η, θ) space. Denoting the body normal as

$$\vec{n}_b = -Gb_\xi \hat{i} + G\hat{j} + (\eta_\phi - \xi_\phi b_\xi - b_\theta)/y \hat{k} \quad (3.96)$$

the boundary condition becomes

$$-Gub_\xi + Gv + w(\eta_\phi - \xi_\phi b_\xi - b_\theta)/y = 0 \quad (3.97)$$

The coefficient A, defined as

$$A = Z_\tau + (Gu + w\xi_\phi/y)Z_\xi + (Gv + w\eta_\phi/y)Z_\eta + wZ_\theta/y$$

can be shown to vanish at the body since, with $Z = 0$,

$$Z_\tau = 0$$

$$Z_\xi = -Z_\eta b_\xi$$

$$Z_\theta = -Z_\eta b_\theta$$

and thus

$$A = Z_\eta [-Gub_\xi + Gv + w(\eta_\phi - \xi_\phi b_\xi - b_\theta)/y] \equiv 0$$

from Equation (3.97). Choosing $\lambda < 0$ at the body and simplifying the expression for λ yields

$$\lambda_b = -aZ_\eta [G^2(1+b_\xi^2) + (\eta_\phi - \xi_\phi b_\xi - b_\theta)^2/y^2]^{1/2} \quad (3.98)$$

and the compatibility condition becomes

$$P_T + \lambda P_Z + \gamma Z_\eta [-Gb_\xi u_Z + Gv_Z + (\eta_\phi - \xi_\phi b_\xi - b_\theta)w_Z/y] = \sum_{i=1}^4 \lambda_i R_i \quad (3.99)$$

since $\lambda_2 u_T + \lambda_3 v_T + \lambda_4 w_T = 0$ from the time invariant boundary condition, Equation (3.97).

At the shock, with $\lambda > 0$ and $Z = 1$, it follows that

$$\lambda_s = A + aZ_\eta [G^2(1+c_\xi^2) + (\eta_\phi - \xi_\phi c_\xi - c_\theta)^2/y^2]^{1/2} \quad (3.100)$$

since

$$Z_\xi = -Z_\eta c_\xi$$

$$Z_\theta = -Z_\eta c_\theta$$

and A no longer vanishes. The appropriate compatibility condition at the shock is given in the general form of Equation (3.95).

Specific application of these characteristic relations for boundary point calculations will be presented in Section 5.0.

3.6 TREATMENT OF THE SINGULAR CENTERLINE

In the (x, y, ϕ) cylindrical coordinate system the x -axis ($y = 0$) is a singular line, where the coordinate ϕ is multi-valued. Along this axis the governing Equations (3.69)-(3.73) must take on different forms valid along this axis, eliminating indeterminate terms that result from the singularity. The modified governing equations that then result involve second derivatives of the dependent variables, such as P_{xy} , etc.

In order to avoid these second derivatives, other approaches to the centerline problem may be used. For example, the governing equations can be reformulated in a local Cartesian coordinate system, which does not exhibit singular behavior. Approximation of derivatives in the Cartesian space would, however, require extensive interpolation on the data at the computational grid points which are not aligned with the Cartesian coordinates.

In this analysis, a set of governing equations based on the Cartesian approach at the centerline is developed which minimizes the need for interpolation, while simultaneously avoiding the approximation of second derivatives. (For the three-dimensional conformal mapping approach developed in this research effort, the approximation of second derivatives at the centerline is made particularly difficult by the fact that the transformations used in each ϕ plane are independent and thus are not continuous across the centerline.)

To develop the form of the governing equations desired at the centerline, consider a Cartesian reference frame (x_1, x_2, x_3) , oriented with the (x, y, ϕ) cylindrical system as shown in Figure 3.11, and defined by

$$x_1 = x \quad (3.101)$$

$$x_2 = y \cos \phi \quad (3.102)$$

$$x_3 = y \sin \phi \quad (3.103)$$

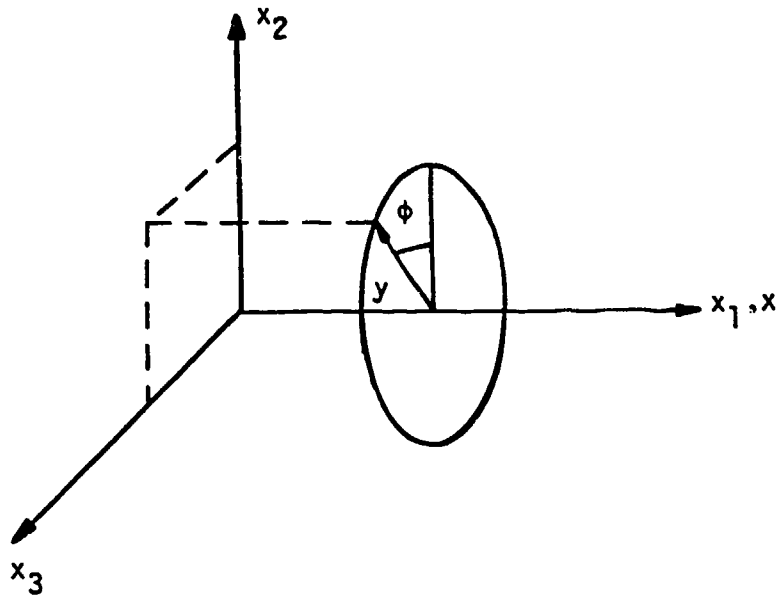


FIGURE 3.11. CARTESIAN COORDINATE SYSTEM AT THE CENTERLINE

Then, by the chain rule,

$$\frac{\partial}{\partial x_1} = \frac{\partial}{\partial x} \quad (3.104)$$

$$\frac{\partial}{\partial x_2} = \cos \phi \frac{\partial}{\partial y} - \sin \phi / y \frac{\partial}{\partial \phi} \quad (3.105)$$

$$\frac{\partial}{\partial x_3} = \sin \phi \frac{\partial}{\partial y} + \cos \phi / y \frac{\partial}{\partial \phi} \quad (3.106)$$

Derivatives in the Cartesian frame may now be expressed in terms of the cylindrical frame, without any indefinite forms appearing, by carefully selecting the values of ϕ for which certain derivatives are evaluated. For example, all derivatives $\frac{\partial}{\partial x_2}$ are evaluated as $\cos\phi \frac{\partial}{\partial y}$ in the $\phi = 0$ and $\phi = \pi$ planes, and all derivatives $\frac{\partial}{\partial x_3}$ are evaluated as $\sin\phi \frac{\partial}{\partial y}$ in the $\phi = \pi/2$ and $\phi = 3\pi/2$ planes. These simple forms result since

$$\lim_{y \rightarrow 0} \frac{1}{y} \frac{\partial}{\partial \phi} = \frac{\partial^2}{\partial y \partial \phi} \quad (3.107)$$

which has a finite value (if $\frac{\partial}{\partial x_2}$ and $\frac{\partial}{\partial x_3}$ are bounded, as is implicitly assumed in this analysis).

Starting with the governing inviscid equations written in a Cartesian coordinate system and applying these chain rules, a system of equations in cylindrical coordinates results that is valid along the centerline and does not involve any second derivatives. The resulting equations do, however, have some terms that must be evaluated in the $\phi = 0$ or $\phi = \pi$ planes, and others that must be evaluated in the $\phi = \pi/2$ or $\phi = 3\pi/2$ planes. (Because of this form of the equations, it is necessary in the numerical solution to require a computational grid that includes these four ϕ planes.)

Transforming these special equations in cylindrical coordinates to (ξ, η, θ, π) space and then to the (X, Y, Z, T) computational space, and writing the equations in terms of the transformed velocity components results in the final forms of

$$\begin{aligned} & [P_{\eta} + A_1 P_Z + B_1 P_Y + \gamma G \{Z_{\xi} u_Z + Y_{\xi} u_Y + Z_{\eta} v_Z + \epsilon\}]_{\phi = 0, \pi} \\ & + [G u (Z_{\xi} P_Z + Y_{\xi} P_Y) + \gamma G (Z_{\xi} u_Z + Y_{\xi} u_Y + v \phi_2)]_{\phi = \frac{\pi}{2}, \frac{3\pi}{2}} = 0 \end{aligned} \quad (3.108)$$

$$\begin{aligned} & [(u_T + A_1 u_Z + B_1 u_Y + vGD + \rho G(Z_\xi P_Z + Y_\xi P_Y)/\rho) \cos \phi]_\phi = 0, \pi \\ & + [-Gu(Z_\xi w_Z + Y_\xi w_Y) \sin \phi]_\phi = \frac{\pi}{2}, \frac{3\pi}{2} = 0 \end{aligned} \quad (3.109)$$

$$\begin{aligned} & [v_T + A_1 v_Z + B_1 v_Y - uGD + \rho G Z_\eta P_Z / \rho]_\phi = 0, \pi \\ & + [Gu(Z_\xi v_Z + Y_\xi v_Y - u\phi_2)]_\phi = \frac{\pi}{2}, \frac{3\pi}{2} = 0 \end{aligned} \quad (3.110)$$

$$\begin{aligned} & [(w_T + A_1 w_Z + B_1 w_Y) \cos \phi]_\phi = 0, \pi + [Gu(Z_\xi u_Z + Y_\xi u_Y + v\phi_2) \\ & + \rho G(Z_\xi P_Z + Y_\xi P_Y)/\rho] \sin \phi]_\phi = \frac{\pi}{2}, \frac{3\pi}{2} = 0 \end{aligned} \quad (3.111)$$

$$[s_T + A_1 s_Z + B_1 s_Y]_\phi = 0, \pi + [Gu(Z_\xi s_Z + Y_\xi s_Y)]_\phi = \frac{\pi}{2}, \frac{3\pi}{2} = 0 \quad (3.112)$$

where

$$A_1 = Z_T + G(uZ_\xi + vZ_\eta)$$

$$B_1 = GuY_\xi$$

The characteristic compatibility conditions required at the body and shock points on the centerline may be formed as a linear combination of these special centerline equations following the same procedure presented in Section 3.5 for regular points. Special forms of the characteristic slopes λ and the multipliers λ_i may be derived at the centerline as follows.

Consider the unit body normal at the centerline. In general the unit body normal at points off the centerline may be written as

$$\hat{n} = \frac{-Gb_{\xi} \hat{i} + G\hat{j} + (\eta_{\phi} - \epsilon_{\phi} b_{\xi} - b_{\theta})/y \hat{k}}{[G^2(1+b_{\xi}^2) + (\eta_{\phi} - \epsilon_{\phi} b_{\xi} - b_{\theta})^2/y^2]^{1/2}} \quad (3.113)$$

At the centerline, of course, a different expression must be used for the \hat{k} component of this vector. But now consider this unit vector at the centerline in the $\phi = 0$ plane (with unit vectors $\hat{i}_1, \hat{j}_1, \hat{k}_1$) and in the $\phi = \pi/2$ plane (with unit vectors $\hat{i}_2, \hat{j}_2, \hat{k}_2$), as depicted in Figure 3.12. This unit body normal can then be written in the two equivalent forms

$$\hat{n} = \frac{-G_1 b_{\xi_1} \hat{i}_1 + G_1 \hat{j}_1 + (\eta_{\phi_1} - \epsilon_{\phi_1} b_{\xi_1} - b_{\theta_1})/y_1 \hat{k}_1}{D_1} \quad (3.114)$$

$$\hat{n} = \frac{-G_2 b_{\xi_2} \hat{i}_2 + G_2 \hat{j}_2 + (\eta_{\phi_1} - \epsilon_{\phi_1} b_{\xi_1} - b_{\theta_1})/y_1 \hat{k}_1}{D_2} \quad (3.115)$$

where D_1 and D_2 are the respective denominators. But noting that \hat{j}_1 and \hat{j}_2 are coincident with the centerline and that Equations (3.114) and (3.115) represent the same vector, it follows that

$$\frac{G_1}{D_1} = \frac{G_2}{D_2} \quad (3.116)$$

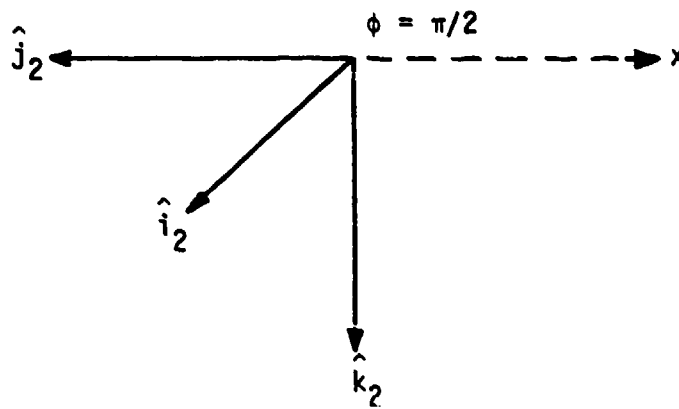
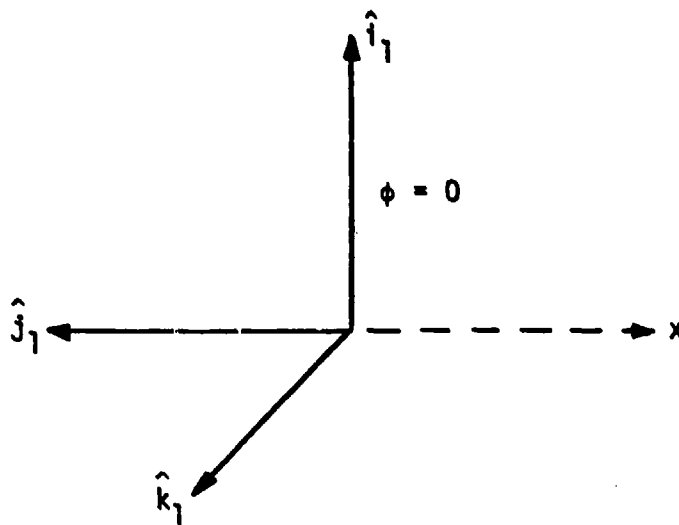


FIGURE 3.12. UNIT VECTORS AT CENTERLINE

Furthermore, since $\hat{k}_1 = \hat{i}_2$,

$$\frac{(\eta\phi_1 - \xi\phi_1 b_{\xi_1} - b_{\theta_1})/y_1}{D_1} = \frac{-G_2 b_{\xi_2}}{D_2} \quad (3.117)$$

and the indeterminate term at the centerline may be expressed as

$$\lim_{y_1 \rightarrow 0} (\eta\phi_1 - \xi\phi_1 b_{\xi_1} - b_{\theta_1})/y_1 = -G_1 b_{\xi_2} \quad (3.118)$$

Thus, the outward body normal may be written as

$$\hat{n}_b = \frac{-b_{\xi_1} \hat{i}_1 + \hat{j}_1 - b_{\xi_2} \hat{k}_1}{[1 + b_{\xi_1}^2 + b_{\xi_2}^2]^{1/2}} \quad (3.119)$$

and similarly, the shock normal may be written as

$$\hat{n}_s = \frac{-c_{\xi_1} \hat{i}_1 + \hat{j}_1 - c_{\xi_2} \hat{k}_1}{[1 + c_{\xi_1}^2 + c_{\xi_2}^2]^{1/2}} \quad (3.120)$$

The characteristic slopes can then be written in the $\phi = 0$ plane as

$$\lambda_b = -aGZ_{\eta} [1 + b_{\xi_1}^2 + b_{\xi_2}^2]^{1/2} \quad (3.121)$$

$$\lambda_s = A + aGZ_{\eta} [1 + c_{\xi_1}^2 + c_{\xi_2}^2]^{1/2} \quad (3.122)$$

where A at $\phi = 0$ is now given by

$$A = A_1 - \gamma G Z_\eta c_{\xi 2} \quad (3.123)$$

The multipliers λ_i at the body become

$$\lambda_2 = -\gamma G Z_\eta b_{\xi 1} / \lambda \quad (3.124)$$

$$\lambda_3 = \gamma G Z_\eta / \lambda \quad (3.125)$$

$$\lambda_4 = -\gamma G Z_\eta b_{\xi 2} / \lambda \quad (3.126)$$

and at the shock

$$\lambda_2 = -\gamma G Z_\eta c_{\xi 1} / (\lambda - A) \quad (3.127)$$

$$\lambda_3 = \gamma G Z_\eta / (\lambda - A) \quad (3.128)$$

$$\lambda_4 = -\gamma G Z_\eta c_{\xi 2} / (\lambda - A) \quad (3.129)$$

While the expressions presented above have been derived assuming that ()₁ refers to $\phi = 0$ and ()₂ refers to $\phi = \pi/2$, these forms are equally valid for ()₁ representing $\phi = \pi$ and ()₂ representing $\phi = 3\pi/2$.

SECTION 4

CALCULATION OF EMBEDDED SHOCKS

The method selected in this research for the calculation of embedded shocks is the shock-capturing approach, in which shock waves (and other discontinuities, such as slip lines) are computed automatically, albeit approximately. Two methods of shock-capturing are examined in this section: the conservation (shock-smearing) approach and the λ -differencing (non-conservation) approach. The relative merits of these two methods are compared by developing axisymmetric versions of both procedures, described in Sections 4.1 and 4.2, and assessing the abilities of each scheme to compute inviscid shock layer flows with embedded shocks. Section 4.3 details the comparisons of these calculations to experimental data, which show the λ -differencing approach to be superior. Finally, in Section 4.4, the λ -differencing scheme is extended to three dimensions.

4.1 CONSERVATION LAW APPROACH TO SHOCK-CAPTURING

The theory behind the conservation law approach is to reformulate the governing partial differential equations in terms of dependent variables that appear naturally in the integral conservation laws. The resulting dependent variables then represent quantities that are reminiscent of the quantities conserved across a discontinuity from the Rankine-Hugoniot conditions (mass, momentum, and energy flux). Hopefully, these new dependent variables will be continuous across the discontinuity, and thus a numerical solution can be obtained directly without special treatment for the discontinuity.

It must be noted, however, that the dependent variables in the differential conservation formulation are strictly continuous only if the discontinuity is perfectly aligned with the coordinate mesh used in the calculations and if the discontinuity is stationary. Therefore, for shocks that are not aligned with the mesh or that are moving (such as during the transient phase of a time-asymptotic calculation), the dependent variables are not continuous and the conservation form of the governing differential equations is not strictly valid.

To illustrate these points, consider a stationary shock inclined at an angle σ to a two-dimensional Cartesian mesh, as shown in Figure 4.1. The conservation form of the steady inviscid continuity equation is

$$(\rho u)_x + (\rho v)_y = 0 \quad (4.1)$$

where u and v are the x - and y - velocity components, respectively.

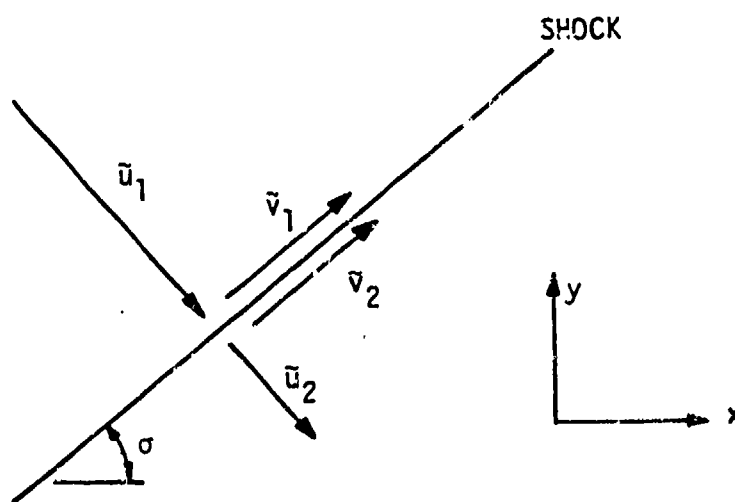


FIGURE 4.1. STEADY INCLINED SHOCK

The Rankine-Hugoniot conditions for this case require that

$$\rho_1 \tilde{u}_1 = \rho_2 \tilde{u}_2 \quad (4.2)$$

$$\tilde{v}_1 = \tilde{v}_2 \quad (4.3)$$

where $()_1$ denotes the low pressure side of the shock, and $()_2$ denotes the high pressure side. Since

$$\tilde{u} = u \cos \sigma - v \sin \sigma \quad (4.4)$$

$$\tilde{v} = u \sin \sigma + v \cos \sigma \quad (4.5)$$

the continuity relation given by Equation (4.2) becomes

$$\rho_1 u_1 = \rho_2 u_2 + \tan \sigma (\rho_1 v_1 - \rho_2 v_2) \quad (4.6)$$

Clearly, the conservation variable ρu will be continuous across the shock only if $\sigma = 0$ (i.e., if the shock is aligned with the coordinate system).

Similarly, consider the case of a normal shock ($\sigma = \pi/2$) moving to the left with velocity W , as illustrated in Figure 4.2. Equation (4.2) becomes

$$\rho_1 (u_1 + W) = \rho_2 (u_2 + W) \quad (4.7)$$

Hence the conservation variable ρu will be continuous across the shock only if the shock velocity were to vanish.

A discussion of the dependence of conservation shock-capturing results on the orientation of the discontinuity relative to the coordinate mesh may be found in McCormack and Paullay²⁵.

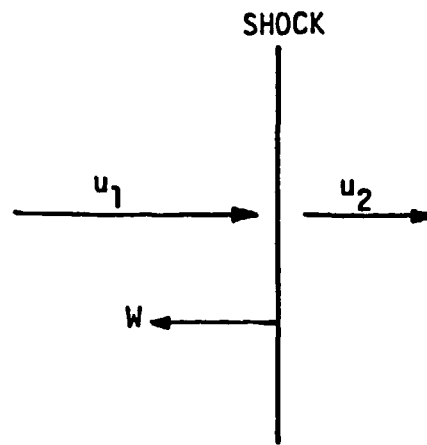


FIGURE 4.2. UNSTEADY NORMAL SHOCK

Despite the lack of continuity of the conservation variables across a shock in the general case, however, it can reasonably be expected that the conservation variables will be "smoother" than the primitive variables (p, ρ , etc.) across a shock. Thus, conservation form calculations may have the potential of "automatically" computing shocks in cases where the non-conservation (Eulerian) formulation, without λ -differencing or shock-fitting, would fail.

The calculation of discontinuities with the conservation formulation smears the discontinuities over several mesh intervals and also introduces oscillations into the calculation at discontinuities. The conservation approach must then be viewed as an approximate method for computing embedded shocks since the discrete discontinuity is smeared out; the results obtained with this approach will thus be mesh dependent. This approach requires a fine computational mesh to obtain accurate approximations to embedded shocks.

The presence of spurious oscillations in the conservation calculations may require special numerical treatment to avoid failure of the computation. The procedures used in this analysis to control these oscillations are detailed later in this section.

The conservation form of the governing equations can be derived in many forms; the recommended formulation for the calculation of embedded shocks is the "strong" conservation form, in which no undifferentiated terms appear, leading to the overall conservation of mass, momentum, and energy, as discussed by Vinokur²⁶. (Note, however, that this is a global conservation of mass, momentum, and energy.) The totally "strong" conservation form cannot be obtained for the axisymmetric equations, however.

The axisymmetric conservation equations in the computational coordinate system may be written as

$$\vec{F}_T + \vec{G}_Z + \vec{H}_Y + \vec{R} = 0 \quad (4.8)$$

where the vector quantities are defined as

$$\vec{F} = \frac{1}{G^2 Z_\eta} \begin{pmatrix} \rho \\ \rho U \\ \rho V \\ e \end{pmatrix}$$

$$\vec{G} = \frac{1}{G^2 Z_\eta} \begin{pmatrix} \rho A \\ \rho UA + G(\tilde{C}Z_\xi - \tilde{S}Z_\eta)p \\ \rho VA + G(\tilde{S}Z_\xi + \tilde{C}Z_\eta)p \\ eA + G(uZ_\xi + vZ_\eta)p \end{pmatrix}$$

$$\vec{H} = \frac{1}{GZ_\eta} \begin{Bmatrix} \rho u \\ \tilde{C}p + \rho uU \\ \tilde{S}p + \rho uV \\ u(e + p) \end{Bmatrix}$$

$$\vec{R} = \frac{V}{yG^2Z_\eta} \begin{Bmatrix} \rho \\ \rho U \\ \rho V \\ e + p \end{Bmatrix}$$

with e representing the total energy per unit volume,

$$e = \rho h = \rho \left[h + \frac{1}{2} (U^2 + V^2) \right] \quad (4.9)$$

and the computational coordinate Y being redefined for the axisymmetric case as

$$Y = \xi \quad (4.10)$$

and the coefficient A representing

$$A = Z_\tau + GuZ_\xi + GvZ_\eta \quad (4.11)$$

After each computational step (predictor or corrector), the conservation vector F must be decoded to recover the primitive flow variables. The quantities ρ, u, v , and h can be determined directly from \vec{F} ; the pressure p and entropy s can be found directly from these

quantities for an ideal gas, while an iterative decoding procedure may be required for equilibrium real gas thermodynamics.

The use of the conservation formulation of the governing equations can lead to the presence of spurious oscillations in the vicinity of a smeared-out discontinuity. Typically, the magnitude of the oscillations tends to increase as the shock strength increases, and if the oscillations are undamped, the calculation can quickly fail as the oscillations spread throughout the shock layer being computed.

Most conservation law techniques use some form of numerical damping (either implicit or explicit) to control these oscillations (which are mesh dependent). In this analysis, a simple damping technique has been used, which is shown to be equivalent to an artificial viscosity, similar to that used in other conservation formulations, such as by Lax and Wendroff²⁷.

To illustrate the damping procedure used, consider the simple hyperbolic equation

$$f_t + u_0 f_x + v_0 f_y = 0 \quad (4.12)$$

The numerical solution to this equation is first advanced one time step using the MacCormack⁷ predictor-corrector finite difference scheme, described in Section 5.6. Following the corrector stage, a weighted averaging of the solution f_{nm}^{k+1} is performed, as

$$\begin{aligned} \bar{f}_{nm}^{k+1} = & \alpha f_{nm}^{k+1} + \beta [f_{n+1,m}^{k+1} + f_{n-1,m}^{k+1}] \\ & + \gamma [f_{n,m+1}^{k+1} + f_{n,m-1}^{k+1}] \end{aligned} \quad (4.13)$$

where $f_{nm}^k = f(t_0 + k\Delta t, x_0 + n\Delta x, y_0 + m\Delta y)$ and subject to the constraint that

$$\alpha + 2\beta + 2\gamma = 1 \quad . \quad (4.14)$$

Application of this averaging procedure to the numerical solution of Equation (4.12) can be shown through Taylor series expansion to be equivalent to the solution of the modified equation

$$\begin{aligned} f_t + u_0 f_x + v_0 f_y = \beta(\Delta x)^2/\Delta t f_{xx} + \gamma(\Delta y)^2/\Delta t f_{yy} \\ + O(\Delta t^2, \Delta x^2, \Delta y^2) \quad . \quad (4.15) \end{aligned}$$

The coefficients of the second order terms are thus similar to viscosities. For consistency of these viscous-like coefficients, the coefficient γ can be selected to be

$$\gamma = \beta(\Delta x/\Delta y)^2 \quad . \quad (4.16)$$

To more closely simulate physical viscosity, this damping is applied only to the two momentum equations appearing in the axisymmetric conservation system, Equation (4.8).

While the damping formulation described above can be helpful in controlling the oscillations that arise in the calculation of embedded shocks with the conservation equations, it cannot completely compensate for large oscillations. If the oscillations are severe enough, the calculation will typically fail when a negative pressure ($p < 0$) is encountered in the decoding of the conservation variables. Since this condition might occur only during the transient phase of a time-dependent calculation, and not in the steady-state, a second damping (or smoothing) technique is applied locally when required to eliminate the $p < 0$

condition and allow the calculation to continue. At any point $Y = m\Delta Y$ and $Z = n\Delta Z$ where $p < 0$ is encountered, the entire F vector at that Y location is smoothed in Z , from

$$\bar{F}_{nm} = \frac{1}{4} [\bar{F}_{n+1,m} + 2\bar{F}_{n,m} + \bar{F}_{n-1,m}] \quad (4.16)$$

This is the same smoothing function used by Solomon, et al.¹² when the $p < 0$ condition is encountered in the conservation calculation of embedded shocks in steady supersonic flow on reentry vehicle afterbodies. This local smoothing function reduces the numerical scheme to first order accuracy in ΔZ , but has been found helpful in overcoming transient difficulties in the time-dependent calculation.

4.2 λ -DIFFERENCING APPROACH TO SHOCK-CAPTURING

The λ -differencing approach to shock-capturing is fundamentally different from the conservation approach in that its shock-capturing ability comes not from a special formulation of the dependent variables, but rather from careful treatment of the approximations to spatial derivatives. By constructing finite difference approximations that accurately model the domain of dependence of each point being computed, the resulting finite difference equations admit "discontinuous" solutions that approximate the structure of physical solutions with embedded shocks.

The λ -scheme is formulated in terms of the non-conservation governing equations, in which the dependent variables, in two-dimensions, are P, u, v , and s . To illustrate construction of the λ -scheme, consider a one-dimensional, time-dependent inviscid flow, whose governing equations are

$$P_t + uP_x + \gamma u_x = 0 \quad (4.17)$$

$$u_t + uu_x + p/\rho P_x = 0 \quad (4.18)$$

$$s_t + us_x = 0 \quad (4.19)$$

This system of equations has two characteristic directions (aside from the particle path, which is not of interest in this application), defined as

$$\lambda_1 = u - a \quad (4.20)$$

$$\lambda_2 = u + a \quad (4.21)$$

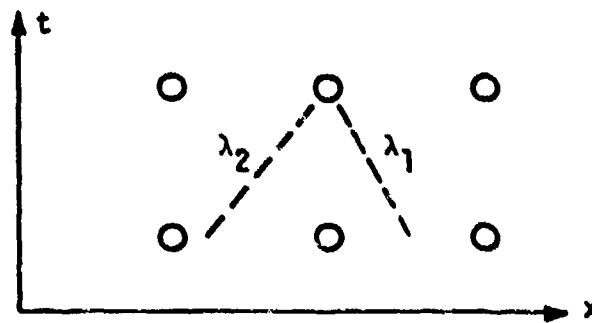
Note that supersonic flow implies $\lambda_1 > 0$ and $\lambda_2 > 0$ and that subsonic flow produces $\lambda_1 < 0$ and $\lambda_2 > 0$, as illustrated in Figure 4.3. The signs of these characteristic slopes at any point define the direction of the domain of dependence at that point.

The basis of the λ -scheme is to rewrite Equations (4.17) and (4.18) in such a manner that the domain of dependence information inherent in the characteristic slopes can easily be incorporated into the resulting finite difference scheme. To this end, the governing equations may be written as

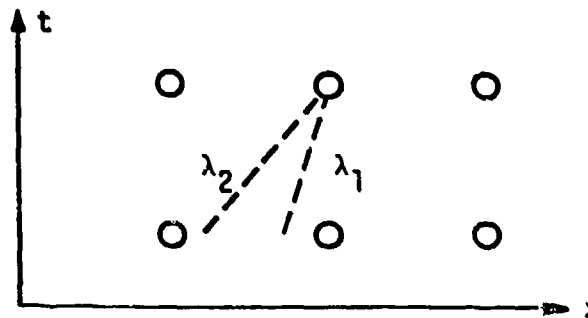
$$P_t + \frac{1}{2} (\lambda_1 P_{x1} + \lambda_2 P_{x2}) + \gamma (\lambda_2 u_{x2} - \lambda_1 u_{x1}) / 2a = 0 \quad (4.22)$$

$$u_t + \frac{1}{2} (\lambda_1 u_{x1} + \lambda_2 u_{x2}) + a (\lambda_2 P_{x2} - \lambda_1 P_{x1}) / 2\gamma = 0 \quad (4.23)$$

which are entirely equivalent to Equations (4.17) and (4.18), with $P_{x1} = P_{x2}$ and $u_{x1} = u_{x2}$.



a.) SUBSONIC FLOW



b.) SUPERSONIC FLOW

FIGURE 4.3. CHARACTERISTIC SLOPES IN x - t PLANE

In a finite difference representation of these equations, P_{x1} and P_{x2} (or u_{x1} and u_{x2}) need not be the same approximation to P_x (or u_x). By constructing second-order accurate one-sided derivative approximations for P_{x1} , P_{x2} , u_{x1} , and u_{x2} in the directions suggested by the corresponding coefficients λ_1 and λ_2 , the numerical algorithm will more accurately model the physical domain of dependence. Thus, for supersonic flow, only upwind information will enter the spatial derivative approximations, and for subsonic flow, a weighted averaging of upwind and downwind information will be employed.

The ability of this scheme to approximate discontinuities arises from its accurate modeling of the physical domain of dependence of each point being computed. In particular, points immediately upstream of a shock, where the flow must be supersonic, will then have no dependence on the flow downstream of the shock. This feature prevents any inaccuracies that arise at the shock from propagating upstream and affecting the entire calculation.

The fundamental limitation of the λ -scheme is that there is no mechanism for an entropy increase across an embedded shock since the shock is not treated explicitly. Furthermore, the λ -scheme is applied only to the continuity and momentum equations: the energy equation still expresses entropy conservation along streamlines. At best, then, the λ -scheme can be expected to approximate an embedded shock as an isentropic compressive discontinuity.

Extending the λ -scheme concept to two-dimensional unsteady flows using the new coordinate system requires the determination of characteristic slopes in both the Z-T and Y-T reference planes. These characteristic slopes may be written as

$$\lambda_{Z1} = A - aGZ_{\eta} (1 + Z_{\xi}^2/Z_{\eta}^2)^{1/2} \quad (4.24)$$

$$\lambda_{Z2} = A + aGZ_{\eta} (1 + Z_{\xi}^2/Z_{\eta}^2)^{1/2} \quad (4.25)$$

$$\lambda_{Y1} = G(u - a) \quad (4.26)$$

$$\lambda_{Y2} = G(u + a) \quad (4.27)$$

and the governing equations become

$$\begin{aligned}
 p_T + \frac{1}{2} (\lambda_{Z_1} p_{Z_1} + \lambda_{Z_2} p_{Z_2}) + \frac{1}{2} (\lambda_{\gamma_1} p_{\gamma_1} + \lambda_{\gamma_2} p_{\gamma_2}) \\
 + \gamma (\lambda_{\gamma_2} u_{\gamma_2} - \lambda_{\gamma_1} u_{\gamma_1}) / 2a + \gamma (\lambda_{Z_2} v_{Z_2} - \lambda_{Z_1} v_{Z_1}) / 2av \\
 + \gamma G Z_{\xi} u_Z + \gamma G E = 0
 \end{aligned} \tag{4.28}$$

$$\begin{aligned}
 u_T + A u_Z + \frac{1}{2} (\lambda_{\gamma_1} u_{\gamma_1} + \lambda_{\gamma_2} u_{\gamma_2}) + G \rho Z_{\xi} p_Z / \rho \\
 + a (\lambda_{\gamma_2} p_{\gamma_2} - \lambda_{\gamma_1} p_{\gamma_1}) / 2\gamma + G v D = 0
 \end{aligned} \tag{4.29}$$

$$\begin{aligned}
 v_T + \frac{1}{2} (\lambda_{Z_1} v_{Z_1} + \lambda_{Z_2} v_{Z_2}) + G u v_{\gamma} \\
 + a (\lambda_{Z_2} p_{Z_2} - \lambda_{Z_1} p_{Z_1}) / 2\gamma v - G u D = 0
 \end{aligned} \tag{4.30}$$

where $v = (1 + Z_{\xi}^2 / Z_{\eta}^2)^{1/2}$

$$A = Z_{\tau} + G u Z_{\xi} + G v Z_{\eta}$$

$$D = v \phi_1 + u \phi_2$$

$$E = -u \phi_1 + v \phi_2 + V / G \gamma$$

The derivative approximations used in the λ -scheme are described in Section 5.7.

4.3 COMPARISON OF AXISYMMETRIC SHOCK-CAPTURING PROCEDURES

In order to compare the relative merits of the conservation and λ -scheme shock-capturing algorithms for the computation of flows over indented nosetips, two axisymmetric codes have been developed from the analyses presented in the preceding two sections. Primarily, the two codes differ in their treatment of the field points; treatment of body and bow shock points is essentially the same for the two approaches, and is equivalent to the procedures described in Sections 5.3 and 5.4.

The first comparison made is for an axisymmetric indented shape, the Very Mildly Indented Body (VMIB), on which wind tunnel tests have been conducted, as described by Reeves, Todisco, Lin, and Pallone²⁰. (Recalibration of the wind tunnel subsequent to the VMIB tests revealed that the nominal Mach number was 7.2, and not 8, as stated in Reference 20.) Figure 4.4 presents predictions of bow shock shape compared to experimental data for the VMIB using the two schemes; both calculations used a 16 x 28 mesh (16 points across the shock layer and 28 points along the body) and were run for 1000 time steps; convergence criteria (see Section 6.2) were satisfied by both calculations. This comparison is continued in Figure 4.5, showing predictions of the surface pressure distribution and the experimental data. As evidenced by these figures, the predictions obtained with both techniques exhibit good agreement with the data. Differences are apparent in the two predictions in the bow shock position towards the downstream boundary of the nosetip shock layer, and in the local extrema of the surface pressure distribution.

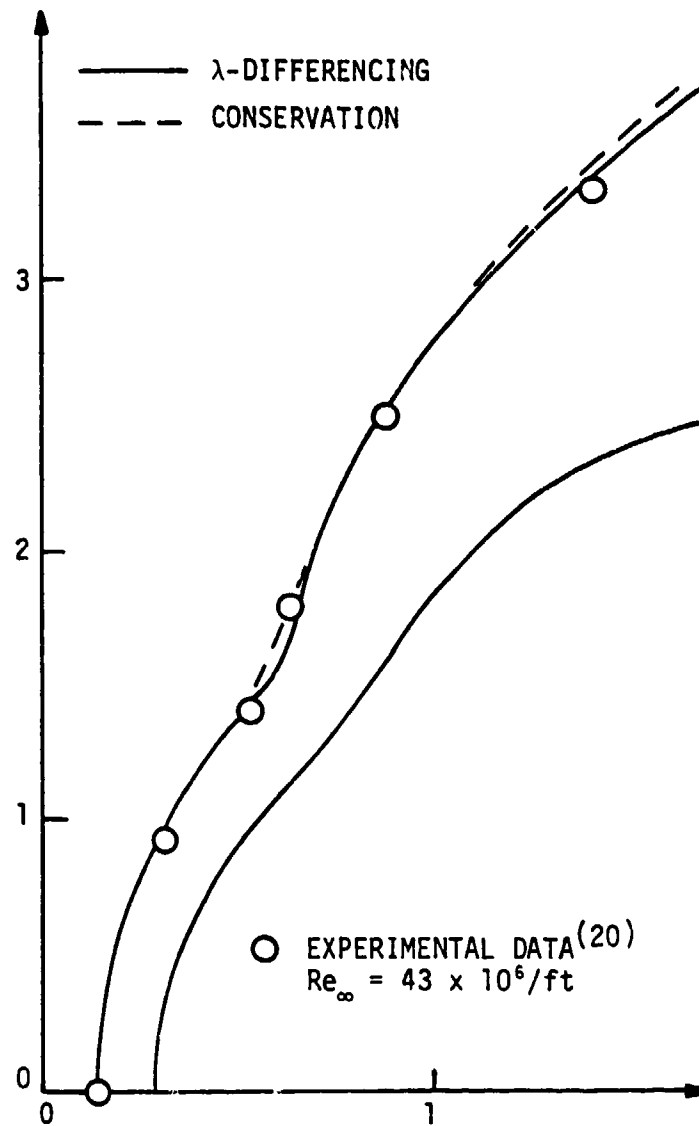


FIGURE 4.4. SHOCK SHAPE PREDICTIONS FOR VMIB AT $M_\infty = 7.2$

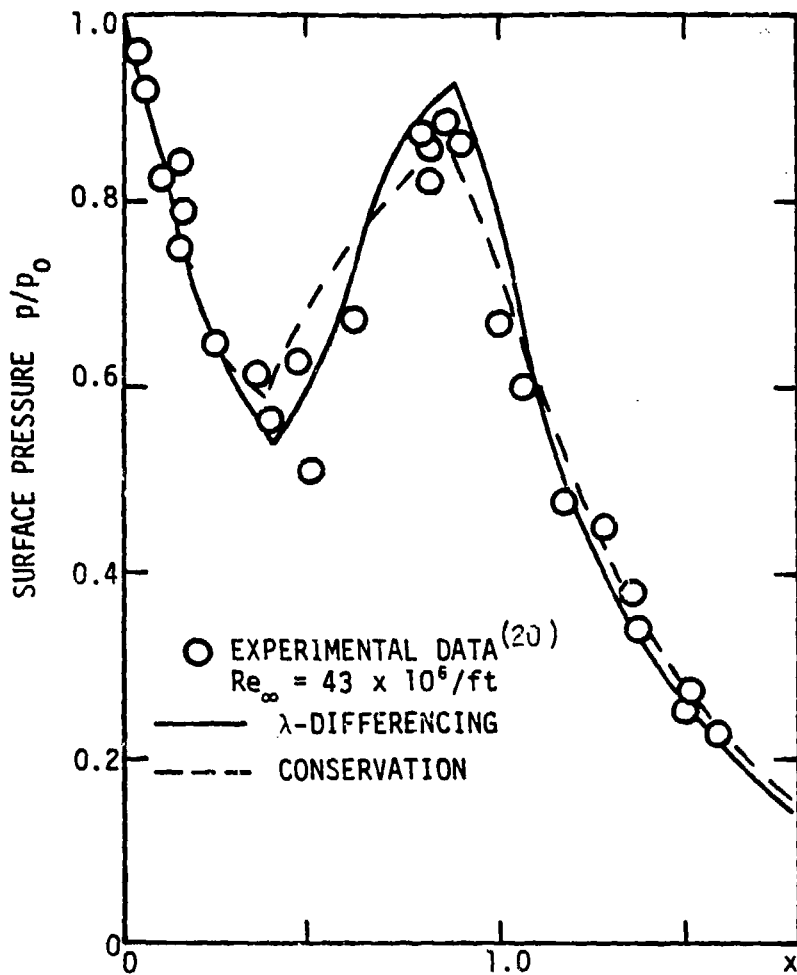


FIGURE 4.5. SURFACE PRESSURE PREDICTIONS
 FOR VMIB AT $M_\infty = 7.2$

It should be noted that, even though the VMIB does not have a strong embedded shock, a small amount of numerical damping ($\beta = 0.008$, with $\Delta Z = 0.067$ and $\Delta Y = 0.085$) is required to obtain a solution for this shape using the conservation form of shock-capturing. The differences noted above between the conservation and λ -differencing solutions are entirely consistent with the effective viscosity implied by the use of numerical damping.

The hazards of the use of numerical damping are illustrated in Figure 4.6, which presents predictions of the bow shock shape for a sphere in ideal gas ($\gamma = 1.4$) at $M_\infty = 10$ obtained with the conservation code using three values of the damping parameter β , with $\Delta Z = 0.2$ and $\Delta Y = 0.11$. The solution with $\beta = 0$ (no damping) agrees well with predictions made using a non-conservation axisymmetric code and the λ -differencing code. The effect of increased damping is clearly evident in this figure; the solution with $\beta = 0.02$ is fairly close to that obtained with no damping. At $\beta = 0.06$, however, the potential of numerical damping to distort the shock layer is graphically illustrated.

For most calculations, of course, a comparison such as that in Figure 4.6 is not possible, and the risk of obtaining a "reasonable" conservation solution with numerical damping that is a poor approximation to the inviscid flow being computed is great. In this regard, the λ -differencing approach is judged to be superior to the conservation approach in that the λ -differencing scheme eliminates the uncertainties inherent in the numerical damping required to generate solutions with the conservation formulation.

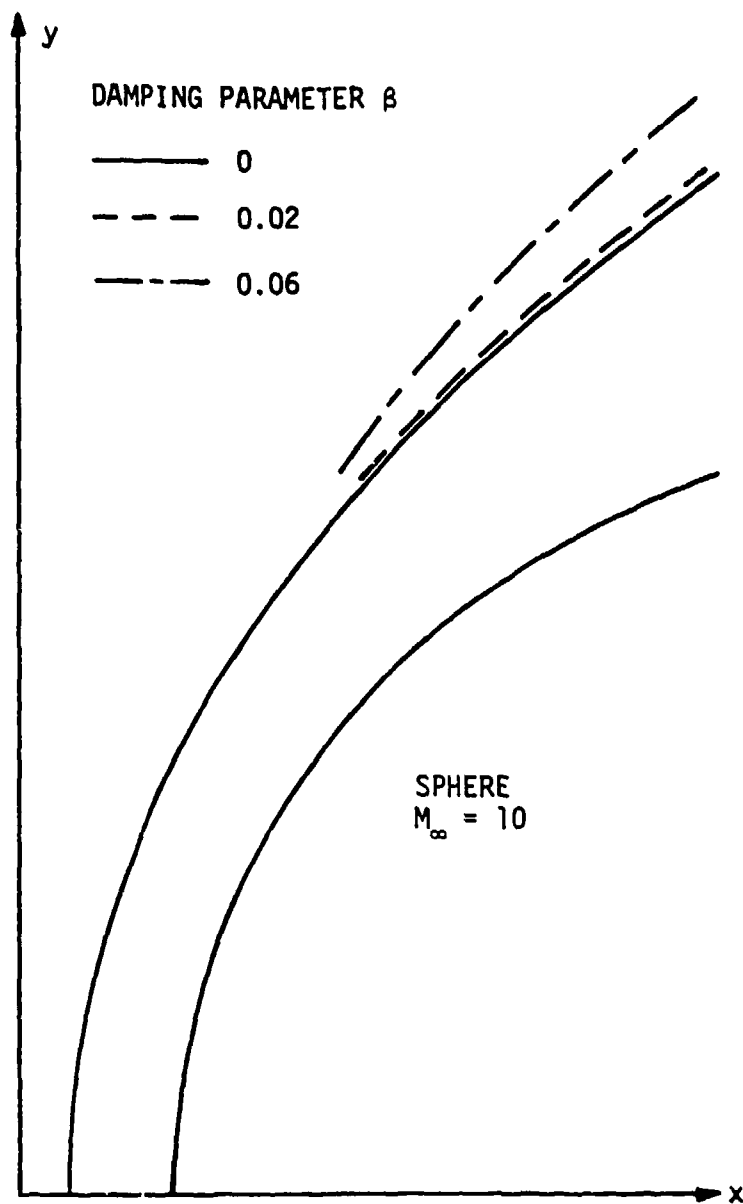


FIGURE 4.6. EFFECT OF DAMPING ON SHOCK SHAPE PREDICTIONS WITH CONSERVATION SCHEME

Another comparison of the two shock-capturing approaches under consideration has been made for the Mildly Indented Body (MIB), another of the axisymmetric shapes considered by Reeves, Todisco, Lin, and Pallone²⁰. Figure 4.7 shows the bow shock shape for this indented body (on which an embedded shock does form) as predicted by the two shock-capturing schemes compared to the data obtained at $M_\infty = 9$. (In Reference 20, the Mach number for the MIB tests was given as 12; recalibration of AEDC Tunnel F has indicated the true Mach number was approximately 9.) The λ -scheme has produced a converged solution for this case (1000 steps), while the conservation solution shown (400 steps) has not converged; in fact the oscillations arising in the conservation solution from the smeared embedded shock are growing and the solution is diverging. Control of these oscillations requires application of a level of numerical damping that grossly distorts the predicted bow shock shape.

As is evident from Figure 4.7, the λ -differencing scheme produces fair agreement with the data, but locates the triple point (where the embedded shock intersects the bow shock) too far downstream and the downstream bow shock too far away from the body. These discrepancies arise because of the lack of accurate modeling of the shock intersection point and the assumption of isentropic flow across the embedded shock.

In an attempt to combine the beneficial features of both the λ -differencing and conservation approaches to embedded shock predictions, conservation calculations were made for the MIB using second-order accurate upwind differences in regions of supersonic flow. Although slightly reducing the amount of numerical damping required to obtain a

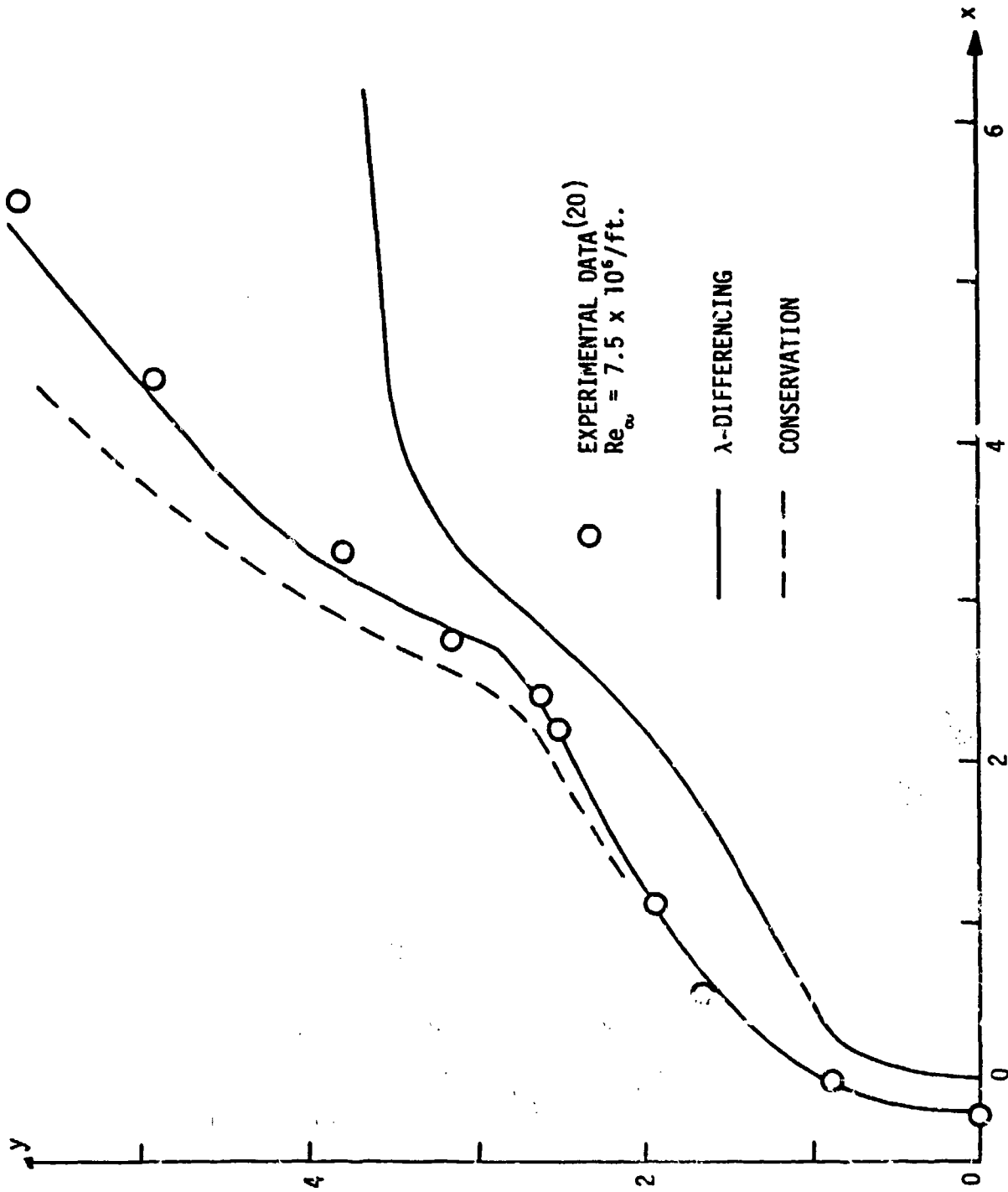


FIGURE 4.7. SHOCK SHAPE PREDICTIONS FOR MIB AT $M_\infty = 9$

solution, this modified conservation approach did not produce any significant improvement in the conservation results depicted in Figure 4.7.

This case serves as an example of the ability of the λ -differencing scheme to compute inviscid time-dependent flows with embedded shocks in a straight-forward manner without resorting to the artifice of numerical damping, thus avoiding the problem of inconsistency of the damped finite difference equations with the inviscid flow equations.

It should be noted that frequently many attempts are required to produce a "good" conservation solution, the problem being to find the smallest possible amount of damping that will sufficiently control the oscillations to allow the solution to proceed without failure, without overly distorting the flow being computed. In some cases, no such value of the damping parameter has been found for the conservation procedure developed in this research.

Based on a number of comparisons of the λ -differencing and conservation solutions, of which the comparisons presented in this section are only a sample, it is concluded that the λ -differencing scheme offers a significant advantage over the conservation solution of the embedded shock problem. Since the λ -scheme does not produce oscillations in the solution as it "captures" an embedded shock, as does the conservation formulation, numerical damping is not required, and the question of consistency of the problem being solved numerically with the inviscid problem does not arise. Furthermore, the λ -scheme has been found to be far more efficient to apply to a given problem, generally requiring only

one calculation, where many conservation solution attempts are typically required to determine the optimum value of the damping parameter. Because of these comparisons, the λ -differencing scheme is the approach to the embedded shock problem that has been selected for extension to the three-dimensional problem.

It must be remembered, however, that the λ -differencing scheme can, at best, only approximate the structure of flows with embedded shocks because of its assumption of isentropic flow. As the strength of the embedded shock grows, this approximate embedded shock solution can be expected to become less accurate. Improving the accuracy of embedded shock calculations will require strict enforcement of the Rankine-Hugoniot conditions, necessitating a shock-fitting, instead of a shock-capturing, approach.

4.4 λ -DIFFERENCING SCHEME IN THREE DIMENSIONS

The extension of the axisymmetric λ -differencing scheme described in Section 4.2 to three dimensions requires the determination of characteristic slopes in the Z-T, Y-T, and X-T reference planes. These six characteristic slopes may be written as:

$$\lambda_{Z1} = A - aGZ_{\eta} v_Z \quad (4.31)$$

$$\lambda_{Z2} = A + aGZ_{\eta} v_Z \quad (4.32)$$

$$\lambda_{Y1} = B - aGY_{\xi} v_Y \quad (4.33)$$

$$\lambda_{Y2} = B + aGY_{\xi} v_Y \quad (4.34)$$

$$\lambda_{X1} = X_{\theta}(w-a)/y \quad (4.35)$$

$$\lambda_{X2} = X_{\theta}(w+a)/y \quad (4.36)$$

where

$$v_Z = [1 + Z_\xi^2/Z_\eta^2 + (\epsilon_\phi Z_\xi/Z_\eta + \eta_\phi + Z_\theta/Z_\eta)^2/G^2 y^2]^{1/2}$$

$$v_Y = [1 + (\epsilon_\phi + Y_\theta/Y_\xi)^2/G^2 y^2]^{1/2}$$

In the λ -differencing scheme the continuity and momentum equations described in Section 3.4 (Equations (3.69)-(3.72)) are rewritten in a form that allows accurate modeling of the domain of dependence of each point. The resulting three-dimensional time-dependent equations become

$$\begin{aligned} P_T + \frac{1}{2} (\lambda_{Z1} P_{Z1} + \lambda_{Z2} P_{Z2}) + \frac{1}{2} (\lambda_{Y1} P_{Y1} + \lambda_{Y2} P_{Y2}) \\ + \frac{1}{2} (\lambda_{X1} P_{X1} + \lambda_{X2} P_{X2}) + \frac{1}{2} \gamma (\lambda_{Y2} u_{Y2} - \lambda_{Y1} u_{Y1}) / a v_Y \\ + \frac{1}{2} \gamma (\lambda_{Z2} v_{Z2} - \lambda_{Z1} v_{Z1}) / a v_Z + \frac{1}{2} \gamma (\lambda_{X2} w_{X2} - \lambda_{X1} w_{X1}) / a \\ + \gamma G (Z_\xi u_Z + E + V/Gy) + \gamma [(\epsilon_\phi Y_\xi + Y_\theta) w_Y \\ + (\epsilon_\phi Z_\xi + \eta_\phi Z_\eta + Z_\theta) w_Z] / y = 0 \end{aligned} \quad (4.37)$$

$$\begin{aligned} u_T + A u_Z + \frac{1}{2} (\lambda_{Y1} u_{Y1} + \lambda_{Y2} u_{Y2}) + C u_X + v G D \\ + v w F / y - \tilde{S} w^2 / y + G p Z_\xi P_Z / \rho \\ + \frac{1}{2} a (\lambda_{Y2} P_{Y2} - \lambda_{Y1} P_{Y1}) / \gamma v_Y = 0 \end{aligned} \quad (4.38)$$

$$\begin{aligned} v_T + \frac{1}{2} (\lambda_{Z1} v_{Z1} + \lambda_{Z2} v_{Z2}) + B v_Y + C v_X - u G D \\ - u w F / y - \tilde{C} w^2 / y + \frac{1}{2} a (\lambda_{Z2} P_{Z2} - \lambda_{Z1} P_{Z1}) / \gamma v_Z = 0 \end{aligned} \quad (4.39)$$

$$\begin{aligned}
& w_T + Aw_Z + Bw_Y + \frac{1}{2} (\lambda_{X1} w_{X1} + \lambda_{X2} w_{X2}) + w(u\bar{S} + v\bar{C})/y \\
& + p [(Z_\xi \epsilon_\phi + Z_\eta \eta_\phi + Z_\theta) P_Z + (\epsilon_\phi Y_\xi + Y_\theta) P_Y] / \rho y \\
& + \frac{1}{2} a (\lambda_{X2} P_{X2} - \lambda_{X1} P_{X1}) / \gamma = 0 \qquad (4.40)
\end{aligned}$$

The coefficients appearing in the above equations are those defined in Section 3.4.

As with the axisymmetric version of the λ -scheme, the energy equation (conservation of entropy along streamlines) is unaltered in the λ -differencing formulation. Centerline points are treated using the special forms of the governing equations derived in Section 3.6.

SECTION 5

NUMERICAL PROCEDURES

5.1 TIME-ASYMPTOTIC SOLUTION & INITIALIZATION

The approach selected for the solution of this steady inviscid flow problem is the time-asymptotic relaxation method. In this approach, the steady flow solution is sought as the limit of a time-dependent flow with time invariant boundary conditions as $t \rightarrow \infty$. Because the time-dependent equations are hyperbolic, this method allows solution of the steady flow problem, which is a boundary value problem, as a mixed initial-boundary value problem with a forward-marching (in time) numerical technique.

Implicit in this approach is the assumption that a steady flow limit exists and is unique. Purely unsteady flows, with an oscillating bow shock, can occur on severely indented nosetips, as analyzed by Reeves²⁸. In principle, a time-dependent numerical technique can compute such oscillatory flows. However, such flows are dominated by viscous separation effects, and thus are not considered in the inviscid problem being addressed.

To properly pose the initial value problem, it is necessary to completely define the flow field at some arbitrary instant of time, $t = 0$. Theoretically, any estimate of the flow field at this instant will suffice, with the solution eventually converging to the (assumed) unique steady state. In practice, however, it is best to use as reasonable an initial flow field estimate as possible, for grossly inaccurate initializations produce large gradients in the flow that the numerical scheme is incapable of handling. Additionally, estimates of

the initial state that are reasonable estimates of the final steady flow field tend to accelerate convergence of the time-dependent technique.

Initial data is generated for this nosetip flow field technique by neglecting the effects of circumferential flow variation. First, an estimate of the shock stand-off distance at the centerline is obtained from

$$\Delta_0 = R_N [0.6137/(M_\infty^2 - 1) + 0.13] \quad (5.1)$$

which is a curve fit of numerical results for spheres at zero angle of attack. From this shock point at the centerline, estimates of the shock shape in each meridional plane can be obtained using a correlation for shock slope on a sphere in terms of the equivalent body angle θ_b from Abbett and Davis²⁹ as:

$$\sigma = 0.5236 + 0.3333\theta_b + 0.2122\theta_b^2 \quad (5.2)$$

where the equivalent body angle is defined as

$$\theta_b = \tan^{-1} \left[\frac{\partial y_b}{\partial x} - \alpha \cos \phi - \beta \sin \phi \right] \quad (5.3)$$

thus including some effects of angle of attack and sideslip. Strictly speaking, the correlation given by Equation (5.2) applies along a body-normal; for this application it is assumed valid along $\xi = \text{constant}$ curves.

Given all of the shock points, the shock slopes c_ξ and c_θ may then be evaluated using finite-difference expressions. From the shock slopes and freestream conditions the downstream shock properties are then evaluated from the Rankine-Hugoniot conditions.

Next, the flow conditions at the body are approximated. From the modified Newtonian impact theory, the surface pressure may be expressed as

$$p = p_0 \sin^2 \theta_b \quad (5.4)$$

where the equivalent body angle is given by Equation (5.3) and p_0 is the normal shock stagnation pressure. Assuming that the normal shock value of entropy applies at the body surface (see Section 3.1), the static enthalpy $h(p,s)$ can then be evaluated from the thermodynamic state relations. Since the total enthalpy H is constant for a steady inviscid flow and

$$H = h + \frac{1}{2} q^2 = h + \frac{1}{2} (u^2 + v^2 + w^2) \quad (5.5)$$

the total velocity V at the body surface can be found. Neglecting crossflow ($w = 0$) and imposing the kinematic boundary condition results in

$$u = V / (1 + b_\xi^2)^{1/2} \quad (5.6)$$

$$v = u b_\xi \quad (5.7)$$

To complete the specification of the initial flow field, linear distributions of $P, s, v,$ and w in η are assumed between the body and shock along $\xi = \text{constant}$ lines. The final velocity component u is assigned from the total enthalpy relation, Equation (5.5).

From this assumed initial state the time-dependent equations can be integrated forward in time to the steady state solution. The problem still remains, however, of determining when a solution is sufficiently converged to be considered an adequate representation of the steady solution.

Convergence of an iterative solution can be defined in terms of variations of the dependent variables; i.e., when the percentage change from step to step of all dependent variables at all mesh points is less than some ϵ , the solution can be assumed converged. The nature of the inviscid nosetip time-dependent problem does, however, conveniently provide other parameters that can be used as a measure of convergence.

During the course of a time-dependent calculation the bow shock position continuously adjusts from its assumed initial position to its final (converged) steady state position. Thus, the root-mean-square of the velocities of the shock points used in the calculation serves as a convenient measure of the convergence of the solution. Additionally, the motion of the bow shock during the calculation provides another criterion for convergence: the conservation of total enthalpy. Unlike the steady case, the total enthalpy is not conserved across a moving shock; thus the total enthalpy will vary throughout the flow field during a time-dependent calculation. The variation of the total enthalpy from its known freestream value then serves as a direct measure of convergence of the calculation, since this difference in total enthalpy will diminish only if all shock velocities are diminishing. Details on the actual convergence criteria used to judge the merits of a calculation are provided in Section 6.2.

5.2 NON-CONSERVATION FIELD POINT TREATMENT

At field points (i.e., all computational grid points not located either on the body or the shock), the governing time-dependent equations in non-conservation form are solved using the MacCormack ⁷ finite-difference scheme, with some variations. This widely used numerical technique is a two-step predictor-corrector scheme and maintains second order accuracy in both mesh spacing and time.

To illustrate the MacCormack technique, consider the simple hyperbolic equation

$$f_t + Af_x = 0 \quad (5.8)$$

where f may represent either a scalar or a vector quantity, and f_n^k represents $f(t_0 + k\Delta t, x_0 + n\Delta x)$. In the predictor stage, the spatial derivative is approximated as a forward difference

$$f_x = (f_{n+1}^k - f_n^k)/\Delta x \quad (5.9)$$

and the predicted value of f_n at $t = t_0 + (k+1)\Delta t$, denoted by \tilde{f}_n^k , is obtained from

$$\tilde{f}_n^k = f_n^k - A \Delta t (f_{n+1}^k - f_n^k)/\Delta x \quad (5.10)$$

In the corrector stage, f_x is approximated using backward differences of the predicted data:

$$f_x = (\tilde{f}_n^k - \tilde{f}_{n-1}^k)/\Delta x \quad (5.11)$$

Overall second order accuracy is achieved by obtaining the final corrected value from

$$f_n^{k+1} = \frac{1}{2} [f_n^k + \tilde{f}_n^k - A \Delta t (\tilde{f}_n^k - \tilde{f}_{n-1}^k) / \Delta x] \quad (5.12)$$

Assuming the coefficient (or coefficient matrix) to be constant, a truncation error analysis shows the leading order error of this scheme to be $-1/6 [f_{ttt}(\Delta t)^2 + Af_{xxx}(\Delta x)^2]$ for the simple equation considered here.

The standard MacCormack scheme is not used consistently throughout non-conservation calculations, however. As noted by Moretti¹⁷, the standard scheme is inappropriate for the approximation of convective derivatives; i.e., Lagrangian derivatives should be approximated using upwind differences only. To maintain second order accuracy for these cases in the context of a predictor-corrector scheme, the standard MacCormack scheme can be modified by replacing Equation (5.9) with

$$f_x = (2f_n^k - 3f_{n-1}^k + f_{n-2}^k) / \Delta x \quad (5.13)$$

when backward differences are required, or by replacing Equation (5.11) with

$$f_x = (-\tilde{f}_{n+2}^k + 3\tilde{f}_{n+1}^k - 2\tilde{f}_n^k) / \Delta x \quad (5.14)$$

when forward differences are required. Use of either of the above modifications retains the overall order of accuracy of the calculation with a truncation error of $1/6 f_{ttt}(\Delta t)^2 + 1/3 Af_{xxx}(\Delta x)^2$. This convective differencing version of the MacCormack predictor-corrector scheme is used in the non-conservation form of the governing equations

for the entropy derivatives in Equation (3.73) and for the derivatives in the convective terms in the momentum Equations (3.70)-(3.72).

Because the MacCormack scheme is explicit, limitations on the time step to be taken must be imposed to prevent unstable calculations. According to the Courant-Friedrichs-Lewy (CFL)³⁰ criterion for stability, the time step must be selected such that the numerical domain of dependence does not exceed the physical domain of dependence of the point being computed. The allowable time step may be evaluated as the minimum value at all points of Δt computed as

$$\Delta t = \min(\Delta x, \Delta y) / [\sqrt{2}\{(u^2 + v^2 + w^2)^{1/2} + a\}] \quad (5.15)$$

This form assumes that the circumferential spacing ($y\Delta\phi$) will not be the controlling length scale, a reasonable assumption for the ablated nosetip geometries usually encountered.

5.3 BODY POINT TREATMENT

Special computational procedures are required at the boundary points of the computational region (i.e., body points and bow shock points), where the governing partial differential equations must be solved in conjunction with the boundary conditions that are to be imposed.

At the body points, the Kentzer-Moretti predictor-corrector scheme is used to accurately model the physics of the flow at the impermeable boundary. In this scheme, the discretization of the boundary conditions suggested by Kentzer¹³ was extended to the predictor-corrector format by Moretti and Pandolfi⁹. The parallels between this scheme and the numerical method of characteristics solution at the body point have been examined by Hall¹⁴.

In the application of the Kentzer-Moretti scheme to the three-dimensional time-dependent problem, the continuity relation given by Equation (3.69) is replaced by the characteristic compatibility condition expressed by Equation (3.99). The circumferential momentum relation, Equation (3.72), is used directly, and the surface entropy is assigned as the normal shock value of the entropy, as discussed in Section 3.1. (DeNeef³¹ has recently published an efficient method of coding the compatibility condition.)

To complete the specification of the body point procedure, two more relations are required.

The kinematic boundary condition, Equation (3.97), provides one of these relations. The other may be obtained from a linear combination of the ξ - and η - momentum equations, given in computational coordinates by Equations (3.70) and (3.71). Defining a "tangential" velocity component \tilde{v} as

$$\tilde{v} = u + b_{\xi} v \quad (5.16)$$

a time-dependent "tangential" momentum equation may be written as

$$\tilde{v}_T = u_T + b_{\xi} v_T \quad (5.17)$$

with u_T and v_T being evaluated from Equations (3.70) and (3.71).

The solution at a body point is obtained by solving Equations (3.99), (3.72), and (5.17) with the standard MacCormack scheme, except that Z-derivatives must always be approximated as forward differences, requiring the use of Equation (5.14) in the corrector stage. Once new values of \tilde{v} and w have been computed, the other velocity components can

be determined from Equation (5.16) and the kinematic boundary condition to be

$$v = \frac{\nabla b_{\xi} - w(\eta_{\phi} - \xi_{\phi} b_{\xi} - b_{\theta})/G\gamma}{1 + b_{\xi}^2} \quad (5.18)$$

$$u = \tilde{v} - vb_{\xi} \quad (5.19)$$

It was discovered during the formulation of this body point procedure that the form of the "tangential" momentum equation described above, where \tilde{v}_T is a linear combination of u_T and v_T determined from Equations (3.70) and (3.71), respectively, must be used when convective Y-differences are taken. In Moretti's¹⁷ original axisymmetric formulation of this scheme, Equation (5.17) was written as

$$\tilde{v}_T = B(\tilde{v}_Y - vb_{\xi\xi}) + \dots \quad (5.20)$$

which follows analytically from

$$\tilde{v}_Y = u_Y + b v_Y + vb_{\xi\xi} \quad (5.21)$$

In theory, this approach is entirely equivalent to the result obtained from the linear combination of Equations (3.70) and (3.71), namely

$$\tilde{v}_T = Bu_Y + b_{\xi}Bv_Y + \dots \quad (5.22)$$

However, when convective Y-differences are used for \tilde{v}_Y in Equation (5.20) and for u_Y and v_Y in Equation (5.22), the resulting finite difference expressions are not equivalent. A truncation error analysis shows that second order accurate convective differencing for \tilde{v}_Y at $Y = m\Delta Y$ produces

$$\tilde{v}_Y = u_Y + b_{\xi_{m-1}} v_Y + v b_{\xi \xi_m} + O(\Delta Y) \quad (5.23)$$

which does not produce an accurate representation of $u_Y + b_{\xi_m} v_Y$. Thus, the form for \tilde{v}_T given by Equation (5.17) is the preferred form for this approach, and has been shown to produce more accurate solutions, in the sense of producing smaller errors in total enthalpy at the body when the solution has converged to the steady state.

5.4 BOW SHOCK POINT TREATMENT

The Kentzer-Moretta predictor-corrector scheme, described in the previous section, is also used for the computation of bow shock points. Unlike the body point procedure, however, the use of this scheme at bow shock points produces an equation for the shock acceleration derived from a characteristic compatibility condition, which can be integrated twice in time to compute the shock velocity and position. The procedure outlined below is essentially that developed and used extensively by Moretti; e.g., as in Reference 17; application of this method has recently been simplified by deNeef³¹.

Derivation of the equation for the shock acceleration starts with the characteristic compatibility condition given by Equation (3.95). The normal freestream velocity component relative to the moving shock may be written as

$$\tilde{u}_\infty = u_\infty N_1 + (v_\infty - c_T/G) N_2 + w_\infty N_3 \quad (5.24)$$

where

$$u_{\infty} = V_{\infty} [\bar{C} \cos\beta \cos\alpha + \bar{S}(\sin\beta \sin\theta + \cos\beta \sin\alpha \cos\theta)] \quad (5.25)$$

$$v_{\infty} = V_{\infty} [-\bar{S} \cos\beta \cos\alpha + \bar{C}(\sin\beta \sin\theta + \cos\beta \sin\alpha \cos\theta)] \quad (5.26)$$

$$w_{\infty} = V_{\infty}(\sin\beta \cos\theta - \cos\beta \sin\alpha \sin\theta) \quad (5.27)$$

and α and β are the angles of attack and sideslip, respectively. The unit normal to the shock is

$$\hat{n}_s = N_1 \hat{i} + N_2 \hat{j} + N_3 \hat{k} \quad (5.28)$$

where

$$N_1 = -Gc_{\xi}/v \quad (5.29)$$

$$N_2 = G/v \quad (5.30)$$

$$N_3 = (\eta_{\phi} - \epsilon_{\phi} c_{\xi} - c_{\theta})/yv \quad (5.31)$$

and

$$v = [G^2(1 + c_{\xi}^2) + (\eta_{\phi} - \epsilon_{\phi} c_{\xi} - c_{\theta})^2/y^2]^{1/2} \quad (5.32)$$

The normal downstream velocity component relative to the moving shock is

$$\tilde{u} = uN_1 + (v - c_T/G)N_2 + wN_3 \quad (5.33)$$

and the downstream velocity components may be written as

$$u = u_{\infty} + (\tilde{u} - \tilde{u}_{\infty})N_1 \quad (5.34)$$

$$v = v_{\infty} + (\tilde{u} - \tilde{u}_{\infty})N_2 \quad (5.35)$$

$$w = w_{\infty} + (\tilde{u} - \tilde{u}_{\infty})N_3 \quad (5.36)$$

The time derivatives that appear in Equation (3.95) can now be replaced with expressions involving the shock acceleration by differentiating the Rankine-Hugoniot conditions to obtain P_T , $\tilde{u}_{\infty T}$, and \tilde{u}_T , and thus also u_T , v_T , and w_T from Equations (5.34)-(5.36).

The final equation for the shock acceleration may then be written as

$$c_{TT} = \left[\sum_{i=1}^4 \lambda_i R_i - T_2 - T_3 \right] / T_1 \quad (5.37)$$

where

$$T_1 = C_3 + \lambda_2 C_9 + \lambda_3 C_{11} + \lambda_4 C_{13} \quad (5.38)$$

$$T_2 = \lambda [P_Z + \lambda_2 u_Z + \lambda_3 v_Z + \lambda_4 w_Z] \quad (5.39)$$

$$T_3 = C_4 + \lambda_2 C_{10} + \lambda_3 C_{12} + \lambda_4 C_{14} \quad (5.40)$$

The Z-derivatives in Equation (5.39) must be evaluated with backward differences, using Equation (5.13) in the predictor calculation. The coefficients in the above expressions are derived in the Appendix.

In the predictor stage, Equation (5.37) can be integrated to yield

$$\tilde{c}_T = c_T^k + c_{TT} \Delta T \quad (5.41)$$

$$\tilde{c} = c^k + c_T^k \Delta T \quad (5.42)$$

The final values of the shock speed and position are obtained in the corrector stage of the calculation from

$$c_T^{k+1} = \frac{1}{2} (c_T^k + \tilde{c}_T + c_{TT} \Delta T) \quad (5.43)$$

$$c^{k+1} = \frac{1}{2} (c^k + \tilde{c} + c_T^{k+1} \Delta T) \quad (5.44)$$

Once the new shock positions have been determined (predictor or corrector), the shock slopes c_ξ and c_θ may be evaluated from

$$c_\xi = c_Y Y_\xi \quad (5.45)$$

and

$$c_\theta = c_X X_\theta + c_Y Y_\theta \quad (5.46)$$

where c_Y and c_X are evaluated from difference formulas. At most shock points, c_Y is evaluated at $Y = m\Delta Y$ from a standard four point formula as

$$c_Y = (c_{m-2} - 6c_{m-1} + 3c_m + 2c_{m+1})/6\Delta Y \quad (5.47)$$

At the last two points in each θ -plane, the expression

$$c_Y = (-2c_{m-3} + 9c_{m-2} - 18c_{m-1} + 11c_m)/5\Delta Y \quad (5.48)$$

is used, while at the point adjacent to the centerline the form used is

$$c_Y = (-2c_{m-1} - 3c_m + 6c_{m+1} - c_{m+2})/6\Delta Y \quad (5.49)$$

c_X is evaluated at $X = 2\Delta X$ using the centered two-point difference formula:

$$c_X = (c_{2+1} - c_{2-1})/2\Delta X \quad (5.50)$$

The other shock derivatives required, $c_{\xi T}$ and $c_{\theta T}$, are determined using the difference formulas given above, but using c_T , the shock velocity, in place of c .

Knowing the shock slopes and velocities, the properties downstream of the shock are determined directly from the Rankine-Hugoniot conditions:

$$\rho \tilde{u} = \rho_\infty \tilde{u}_\infty \quad (5.51)$$

$$p + \rho \tilde{u}^2 = p_\infty + \rho_\infty \tilde{u}_\infty^2 \quad (5.52)$$

$$h + \frac{1}{2} \tilde{u}^2 = h_\infty + \frac{1}{2} \tilde{u}_\infty^2 \quad (5.53)$$

For an ideal gas, these equations can be solved analytically for p , ρ , and \tilde{u} ; for an equilibrium real gas an iterative solution is required. To avoid this time-consuming iteration for real gas calculations, a table of shock properties as a function of \tilde{u}_∞ is created at the start

of the calculation, thus requiring only interpolation to determine the downstream properties at any shock point during the computation. Once \bar{u} has been determined, the downstream velocity components can be computed from Equations (5.34)-(5.36).

5.5 CENTERLINE POINT TREATMENT

Modifications of the numerical procedures described in the preceding sections are required for computational grid points located on the singular centerline. These special procedures required at the centerline are made necessary by the special forms of the governing equations derived in Section 3.6, in which the equations at the centerline are written with terms evaluated only in the planes $\phi = 0, \pi/2, \pi,$ and $3\pi/2$.

Within any ϕ plane, only forward differences in Y are possible at the centerline. In order to maintain a two-sided predictor-corrector sequence for the Y -differences at the centerline, terms in the governing equations are evaluated in the $\phi = 0$ and $\phi = \pi/2$ planes in the predictor stage, and in the $\phi = \pi$ and $\phi = 3\pi/2$ planes in the corrector stage. The resulting numerical scheme thus utilizes information from all directions, in the spirit of the finite difference scheme used at points not located on the centerline.

At field points along the centerline, the equations to be solved with this procedure are given by Equations (3.108)-(3.112). A difficulty arises, however, in the application of this technique when the coordinate transformation to (ξ, η, θ) space is not axisymmetric. In this case, variations in the complex scaling factor g along the centerline among the ϕ planes result in the non-correspondence of the

computational grid points in physical space. In other words, even though the computational grid points at the centerline are equally spaced in Z for all ϕ planes, grid points with the same Z value in different ϕ planes may represent different points in physical space. These differences are minimized by the use of the stretching parameter a_k in the coordinate transformation defined in Section 3.2, and thus linear interpolation procedures can be used to resolve the differences without any noticeable effect on accuracy.

Calculations of the body and shock points along the centerline do not, of course, experience this difficulty, thus simplifying the numerical approach at these points. Details on the modifications required for the characteristic slopes and compatibility conditions at these boundary points are provided in Section 3.6.

A special procedure is required for the calculation of shock slopes at the centerline, where accuracy requires a formulation that utilizes information from more than one ϕ plane. In particular, the calculation of c_ξ in some plane ϕ_1 also requires information about the shock shape from the plane $\phi_1 + \pi$. A standard difference procedure cannot be used, however, when an asymmetric mapping is invoked; i.e., when the mesh spacings $\Delta\xi$ and the transformed shock locations c are not necessarily equal in the ϕ_1 and $\phi_1 + \pi$ planes.

At the centerline, $\tilde{S} = 1$ and $\tilde{C} = 0$ for all ϕ planes. It then follows that, with $()_1$ denoting the ϕ_1 plane and $()_2$ denoting the $\phi_1 + \pi$ plane,

$$(dn/G)_1 = (dn/G)_2 \quad (5.54)$$

and, in the limit as $y \rightarrow 0$,

$$(d\xi/G)_1 = (d\xi/G)_2 \quad (5.55)$$

Using these relations, a four-point difference formula for c_ξ can be derived for unequally spaced base points;

$$c_\xi = Ac_0 + Bc_1 + Cc_2 + Dc_{-1} \quad (5.56)$$

where

$$c_0 = c(0, \phi_1)$$

$$c_1 = c(\Delta\xi_1, \phi_1)$$

$$c_2 = c(2\Delta\xi_1, \phi_1)$$

$$c_{-1} = c_0 + [c(\Delta\xi_2, \phi_1 + \pi) - c(0, \phi_1 + \pi)] G_1/G_2$$

Defining

$$\alpha = G_1\Delta\xi_2/G_2\Delta\xi_1 \quad (5.57)$$

where $\Delta\xi_1$ and $\Delta\xi_2$ are the mesh spacings in the respective ϕ planes, the coefficients in Equation (5.56) are given by

$$A = (\alpha^2 - 5\alpha + 2)/2\Delta\xi_1\alpha(\alpha+1) \quad (5.58)$$

$$B = 2/\Delta\xi_1(\alpha+1) \quad (5.59)$$

$$C = -\alpha/2\Delta\xi_1(\alpha+2) \quad (5.60)$$

$$D = 2/\Delta\xi_1\alpha(\alpha^2 + 3\alpha + 2) \quad (5.61)$$

The derivative $c_{\xi T}$ is evaluated at the centerline using the same approach. For the case of an axisymmetric mapping with $\alpha = 1$, the difference formula given by Equation (5.56) reduces to the standard four-point formula given by Equation (5.47).

Once the solution at a centerline point has been obtained within any one ϕ plane, the solution within other ϕ planes will also have been determined. Thermodynamic properties, such as P and s , correspond directly, but a change in the value of ϕ requires a rotation of the velocity components. The transformed velocity components within any ϕ plane can be written in terms of the known components in some plane $\phi = \phi_1$ from

$$\begin{aligned} u(\phi) &= u(\phi_1)[\cos\phi\cos\phi_1 + \sin\phi\sin\phi_1] \\ &\quad + w(\phi_1)[\sin\phi\cos\phi_1 - \cos\phi\sin\phi_1] \end{aligned} \quad (5.62)$$

$$v(\phi) = v(\phi_1) \quad (5.63)$$

$$\begin{aligned} w(\phi) &= u(\phi_1)[\cos\phi\sin\phi_1 - \sin\phi\cos\phi_1] \\ &\quad + w(\phi_1)[\cos\phi\cos\phi_1 + \sin\phi\sin\phi_1] \end{aligned} \quad (5.64)$$

Similarly, the shock slope c_ξ at the centerline within any ϕ plane may be expressed in terms of the slopes in the $\phi = 0$ and $\phi = \pi/2$ planes as

$$c_\xi(\phi) = c_\xi(\phi=0)\cos\phi + c_\xi(\phi=\frac{\pi}{2})\sin\phi \quad (5.65)$$

The transformed centerline shock velocities may also be related from the condition that the quantity c_T/G , which corresponds to the physical shock velocity, is the same for all ϕ planes; thus

$$c_T(\phi) = G(\phi)c_T(\phi_1)/G(\phi_1) \quad . \quad (5.66)$$

5.6 CONSERVATION FIELD POINT TREATMENT

The conservation law approach to shock-capturing, described in Section 4.1, is one of two methods investigated for the calculation of embedded shocks within inviscid shock layers on reentry vehicle nosetips. This approach requires the solution of the governing equations written in conservation form at all field points using a version of the MacCormack finite difference scheme described in Section 5.2. After each integration step, the conservation solution may be damped and smoothed, as required.

One change has been made in the MacCormack scheme for application to the conservation calculations. Because the oscillations inherent in conservation calculations near a discontinuity arise from approximating derivatives across the discontinuity, the modification made to the MacCormack scheme is designed to minimize the number of differences taken across the discontinuity. This is accomplished by more closely aligning the numerical domain of dependence of any given field point with the probable orientation of an embedded shock within the computational mesh.

To illustrate this point, consider the numerical domain of dependence of a point $Y = m\Delta Y$ and $Z = n\Delta Z$. Defining the numerical domain of dependence of a point as all grid points that can effect the solution at that point in one time step, the standard MacCormack scheme produces the domain of dependence (in the Y - Z plane) shown in Figure 5.1.

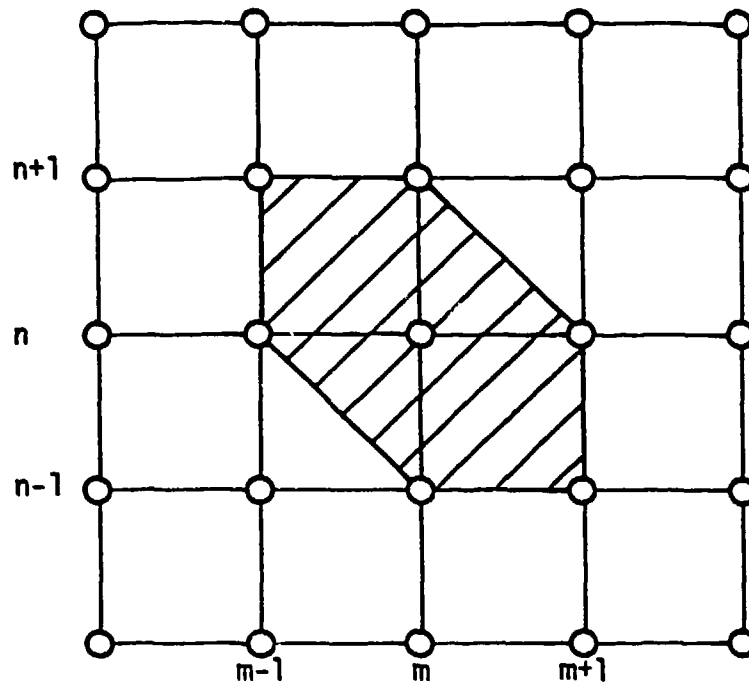


FIGURE 5.1. NUMERICAL DOMAIN OF DEPENDENCE FOR REGULAR MACCORMACK SCHEME

Since the Y-coordinate direction is nearly normal to the body, an embedded shock can be expected to be aligned within the Y-Z mesh as shown in Figure 5.2. Note that the orientation of the shock in the Y-Z mesh is counter to that of the numerical domain of dependence for the regular MacCormack scheme. By changing the orientation of the numerical domain of dependence to be more consistent with the expected shock orientation, a smaller portion of the numerical domain of dependence of a point near the shock will lie across the discontinuity from that point.

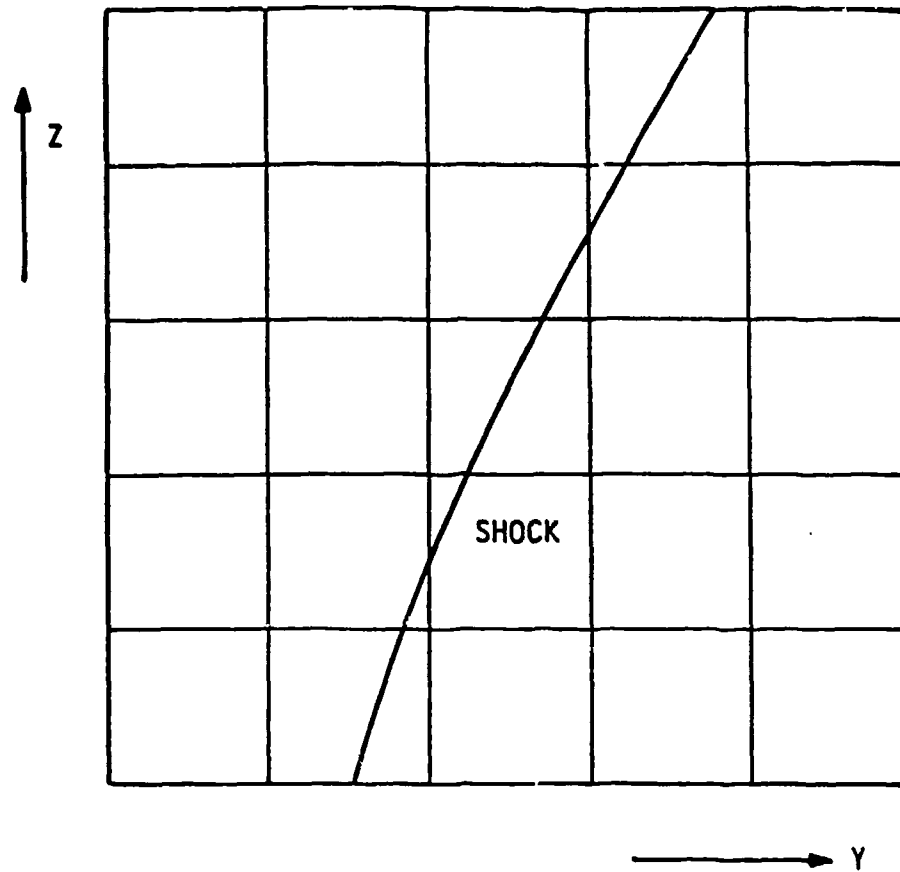


FIGURE 5.2. TYPICAL ALIGNMENT OF EMBEDDED SHOCK IN Y-Z COORDINATE MESH

The numerical domain of dependence is reoriented by reversing the directions of the Z-derivative approximations in the predictor and corrector stages of the MacCormack scheme; i.e., backward differences in the predictor stage and forward differences in the corrector stage. The resulting numerical domain of dependence for this variation on the MacCormack scheme is shown in Figure 5.3.

While this modification to the numerical scheme cannot eliminate the oscillations inherent in conservation calculations of discontinuities, it will, in some circumstances, decrease the magnitude of the oscillations.

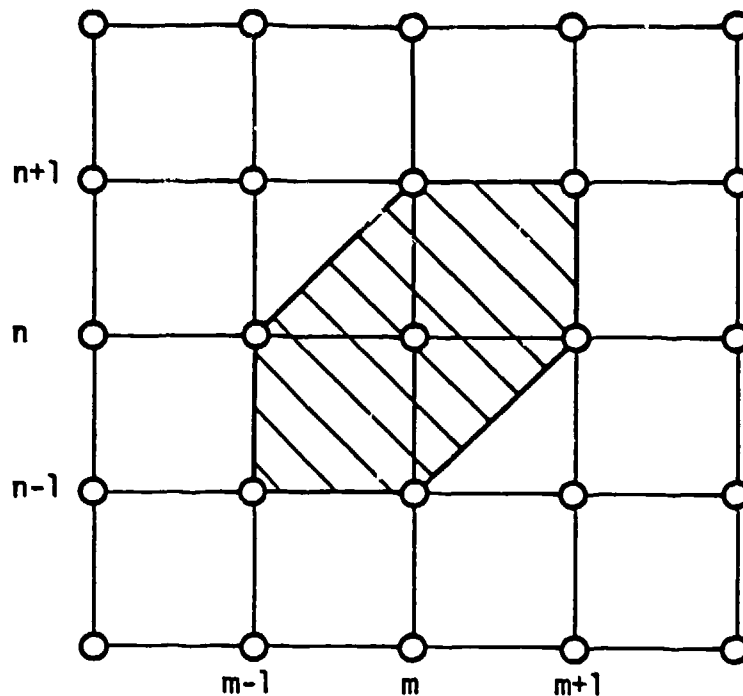


FIGURE 5.3. NUMERICAL DOMAIN OF DEPENDENCE FOR MACCORMACK SCHEME INVERTED IN Z DIRECTION

5.7 λ -DIFFERENCING FIELD POINT TREATMENT

The second method examined in this effort for the automatic calculation of embedded shocks is the λ -differencing scheme, described in Section 4.2. In this approach to the embedded shock problem, the governing equations are written in non-conservation form and certain terms are written in "split" forms that allow accurate modeling of the domain of dependence. For example, the term AP_z would be approximated as $1/2(\lambda_{z_1}P_{z_1} + \lambda_{z_2}P_{z_2})$ with this scheme, where the particular finite difference expressions used for P_{z_1} and P_{z_2} would be dependent on the signs of λ_{z_1} and λ_{z_2} , respectively.

In each "split" term, both the $()_1$ and $()_2$ derivatives are approximated using a second-order accurate, one-sided, predictor-corrector finite difference scheme. For either derivative, if the corresponding coefficient λ_i is positive, backward differences are employed; conversely, if the coefficient is negative, forward differences are used. Backward differences are formed using Equations (5.13) and (5.11) in the predictor and corrector stages, respectively, while forward differences are formed using Equations (5.9) and (5.14), as described in Section 5.2.

It will be noted in the λ -differencing forms of the governing equations, described in Sections 4.2 (axisymmetric) and 4.4 (three dimensional), that some terms are not split. These unsplit terms are those that arise from the computational transformation to (X,Y,Z,T) space and are generally small. The derivatives appearing in these terms are approximated using convective differences, as described in Section 5.2, maintaining the overall second-order accuracy of the scheme.

SECTION 6

VALIDATION OF SOLUTION

6.1 LIMITATIONS OF TECHNIQUE

In this analysis a time-dependent algorithm has been developed for the computation of steady inviscid flows over ablated reentry vehicle nosetips with uniform supersonic or hypersonic freestream conditions. This procedure has been formulated in a new coordinate system that is capable of being closely aligned with any nosetip geometry, and includes a technique for the approximate calculation of embedded shocks. The primary limitation that exists for this technique is the assumption of isentropic flow downstream of the bow shock.

Because of the inviscid flow assumption, the validity of this analysis is limited to those high Reynolds number cases where the thin boundary layer assumption and weak interaction theory apply. Fortunately, for the flight conditions of reentry vehicles with ablated nosetips, for which this analysis was undertaken, viscous effects are generally confined to a thin boundary layer adjacent to the vehicle surface, and the inviscid flow field may be determined independently of the boundary layer.

This inviscid assumption fails, however, when the nosetip geometry produces separation of the shock layer flow. Prediction of the separated flow region must include viscous effects, for which the present analysis is unsuitable.

As discussed in Section 1.0, inviscid theory has been shown to produce accurate aerodynamic predictions for the flight conditions of interest for all aerodynamic coefficients, with the exception of the

axial force coefficient, which can be significantly affected by viscous shear and induced pressure effects. Thus, an inviscid aerodynamic prediction procedure, such as developed here, can be a valuable tool for both the pre-flight and post-flight evaluation efforts relating to reentry vehicle design and performance.

Other limitations apply to the numerical procedure developed in this research that are common to all numerical fluid flow computational procedures. Fundamentally, it is required for accurate results that the discrete grid points used in the numerical calculations be spaced so as to be able to resolve all pertinent features of the body geometry and the surrounding flow field. In particular, a finer mesh will be required in regions of large flow gradients to avoid wiggles in the numerical solution. (The appearance of wiggles in a numerical solution is indicative of inadequate mesh resolution for the case being computed, or of some other error in the formulation or application of the numerical technique. This point is discussed more fully by Moretti³².) Criteria for the selection of appropriate mesh spacings for an earlier transonic code were developed by Hall, Kyriakos, Truncellito, and Martellucci⁴; these criteria are equally valid for the procedure developed in this report.

Inconsistencies between the mesh point spacing and flow gradients can, of course, be eliminated simply by using more mesh points in the finite difference calculation. More core storage will also be required for the computer code with an increased number of mesh points; the only limitations on the use of this analysis in this regard is the available core storage on the computer and the economics of a calculation with a large number of mesh points.

6.2 CONVERGENCE PROPERTIES

The time-dependent approach to solving the steady transonic problem is an iterative technique in which advancement of the solution at any given iteration is defined using the time-dependent equations of motion. In theory, as time increases to infinity, the steady-state flow field solution is approached. The time variable used in the time-dependent technique is directly analogous to the iteration number in other iterative numerical techniques. In any iterative technique, it is necessary to define criteria for accepting a solution as being converged. This section defines convergence criteria that have been developed for time-dependent techniques in Reference 4. These criteria are defined in terms of fluid dynamic phenomena that arise in the course of calculating the shock layer about a body in supersonic flow.

The criteria detailed below are sufficient to determine convergence; i. e., when they are satisfied, the convergence of that particular solution is ensured. Cases frequently arise, however, when a satisfactory solution (from the standpoint of accurate aerodynamic predictions) can be obtained without satisfying all of the convergence criteria. Acceptance of such solutions requires judgement on the part of the user. (In other words, the criteria presented here represent sufficient, but not necessary, conditions for an acceptable solution.)

For a numerical method to be an accurate solution to a problem, it must not only converge, but the numerical scheme must be consistent with the problem being solved. The consistency of the time-dependent technique used in this analysis is based on its discretization of the inviscid Euler equations, and its use of non-dissipative

differencing schemes. Thus, the validity of a solution obtained with this procedure may be examined solely upon the degree of convergence of the solution (assuming that the mesh spacing selected by the user is adequate to define the details of the body geometry).

The convergence criteria developed in the previous study will be summarized below, and then discussed in more detail. These criteria are:

1. The "stagnation" pressure must have converged to an essentially constant value. If the actual stagnation point is known to lie exactly on a mesh point in the finite-difference grid, the computed value of stagnation pressure should be within 0.5% of the known theoretical value of p_0 .
2. The "stand-off distance" of the shock, Δ_0 , must have converged to a constant value.
3. The root-mean-square (rms) of the shock velocities, $(c_T/G)_{rms}$, must be converging (decreasing in value) or have converged and, in magnitude, must satisfy the relation $(c_T/G)_{rms} \leq 0.004 V_\infty$.
4. The total enthalpy at every point in the flow being computed must be within 5% of the known steady-state total enthalpy.

In a three-dimensional calculation, the flow stagnation point does not usually correspond exactly to a computational grid point; thus, for the first two criteria listed above, " p_0 " is taken as the pressure occurring at the centerline body point and " Δ_0 " is taken as the distance between the body point and the bow shock point at

the centerline. To illustrate the convergence of these quantities, Figures 6.1 and 6.2 provide examples of convergent and non-convergent time histories of p_0 .

In the time-dependent technique an initial shock shape is assumed and is allowed to adjust its position during the course of the calculation. Theoretically, for a solution that has converged to a steady state, the shock velocity will have vanished at all shock points to within some "epsilon" of the freestream velocity. On a more practical basis, the criterion described above ($(c_T/G)_{rms} \leq 0.004 V_\infty$) is sufficient to determine a satisfactorily converged solution, provided that the magnitude of $(c_T/G)_{rms}$ is decreasing from step to step (i.e., is not diverging) when the criterion is only marginally satisfied. Samples of converging and diverging time-histories of $(c_T/G)_{rms}$ are illustrated in the plots shown in Figures 6.3 and 6.4. One caveat is required in the assessment of $(c_T/G)_{rms}$. Since $(c_T/G)_{rms}$ is, in a sense, an average of individual shock velocities, it is possible that the criterion on $(c_T/G)_{rms}$ be satisfied, while one or two individual shock velocities are relatively large. Thus, judicious assessment of convergence based on shock velocity should include examination of the individual shock velocities as well as the value of $(c_T/G)_{rms}$.

The final criterion for convergence is based upon the conservation of total enthalpy. Since the total enthalpy is not constant in an unsteady flow, an indication of the convergence and accuracy of a time-dependent solution can be obtained by examining the difference between the computed total enthalpy at each point and the known steady state value (which is equal to the freestream total enthalpy).

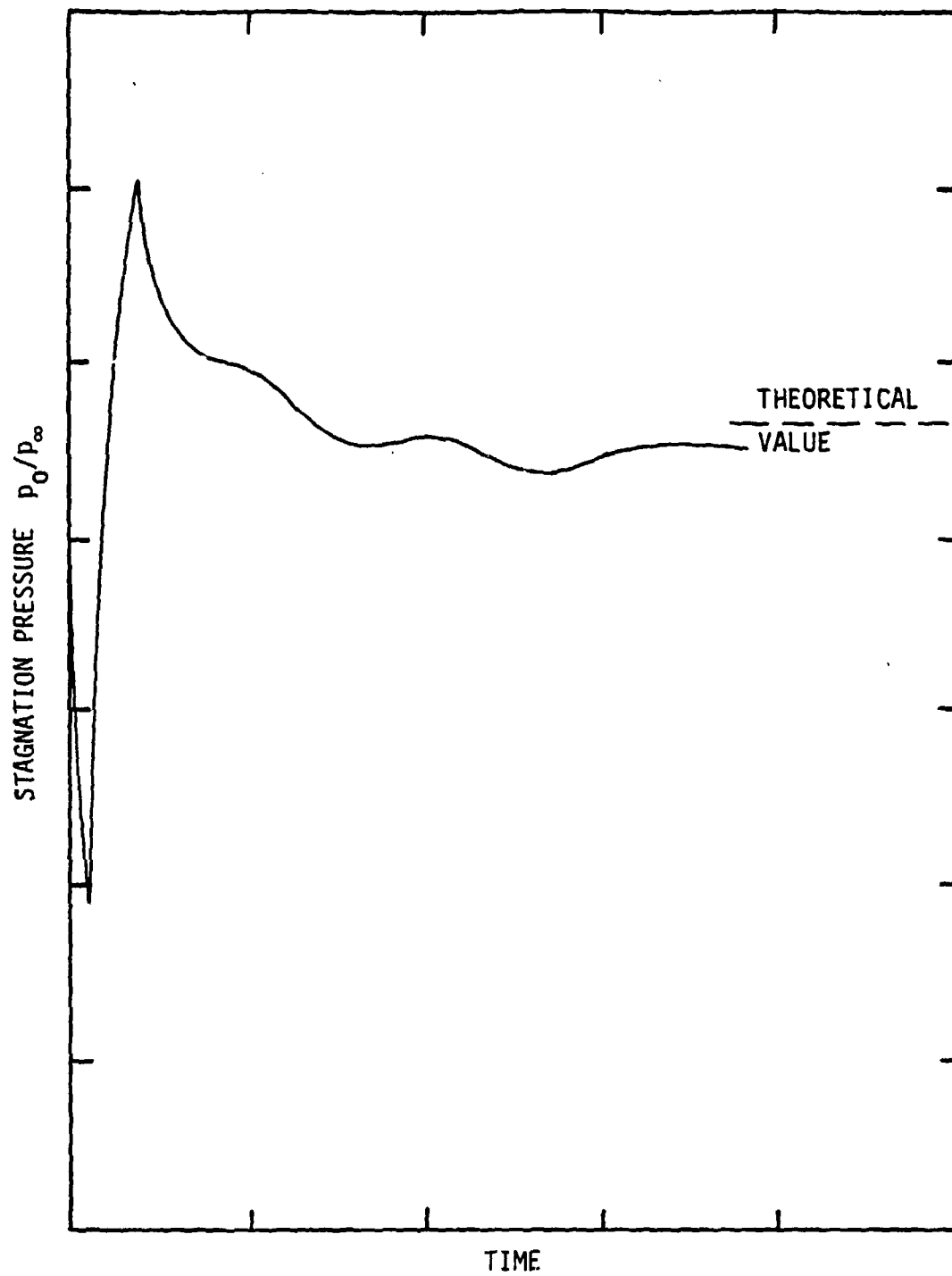


FIGURE 6.1. TYPICAL p_0 HISTORY (CONVERGED)

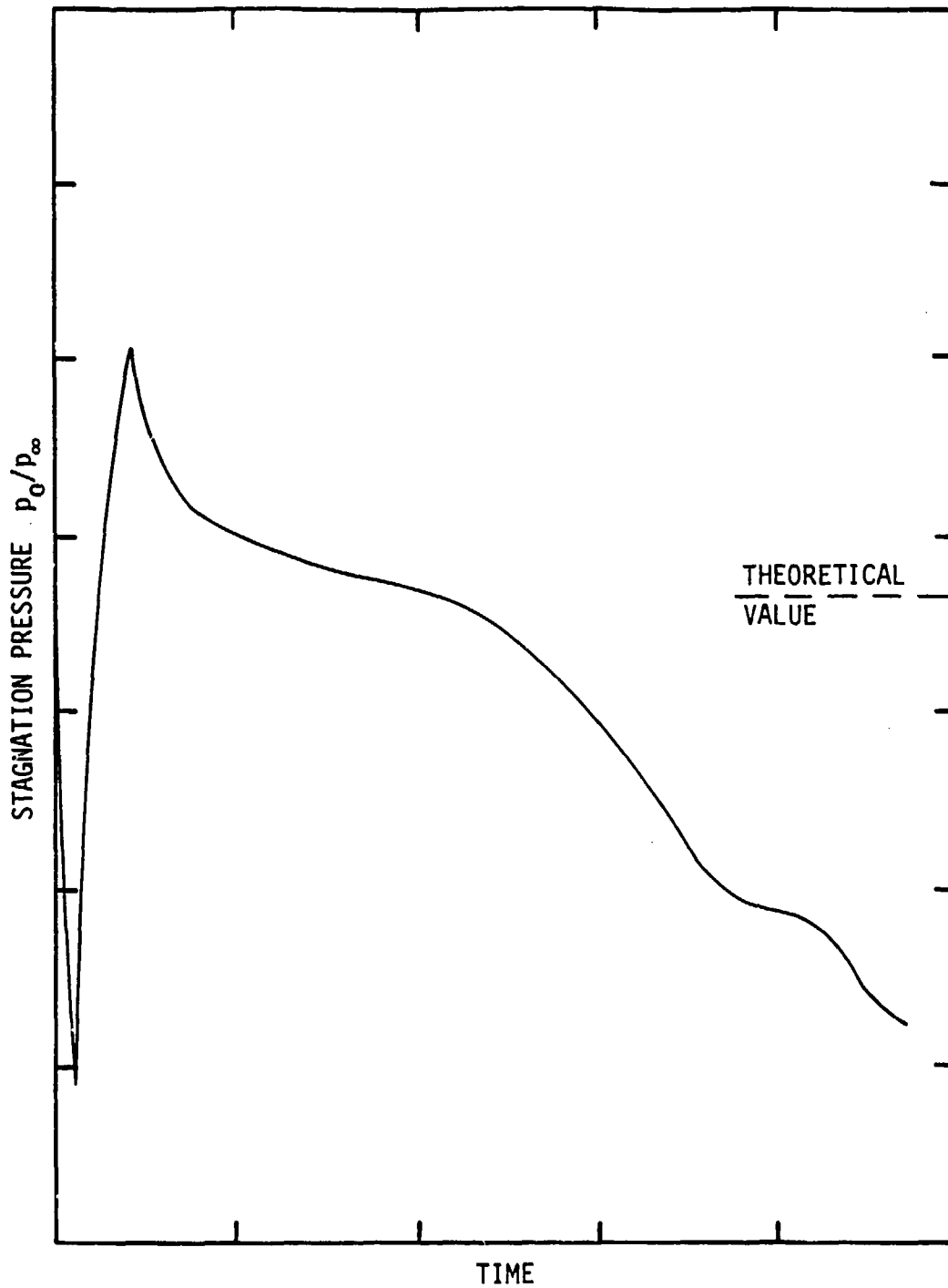


FIGURE 6.2. TYPICAL p_0 HISTORY (NOT CONVERGED)

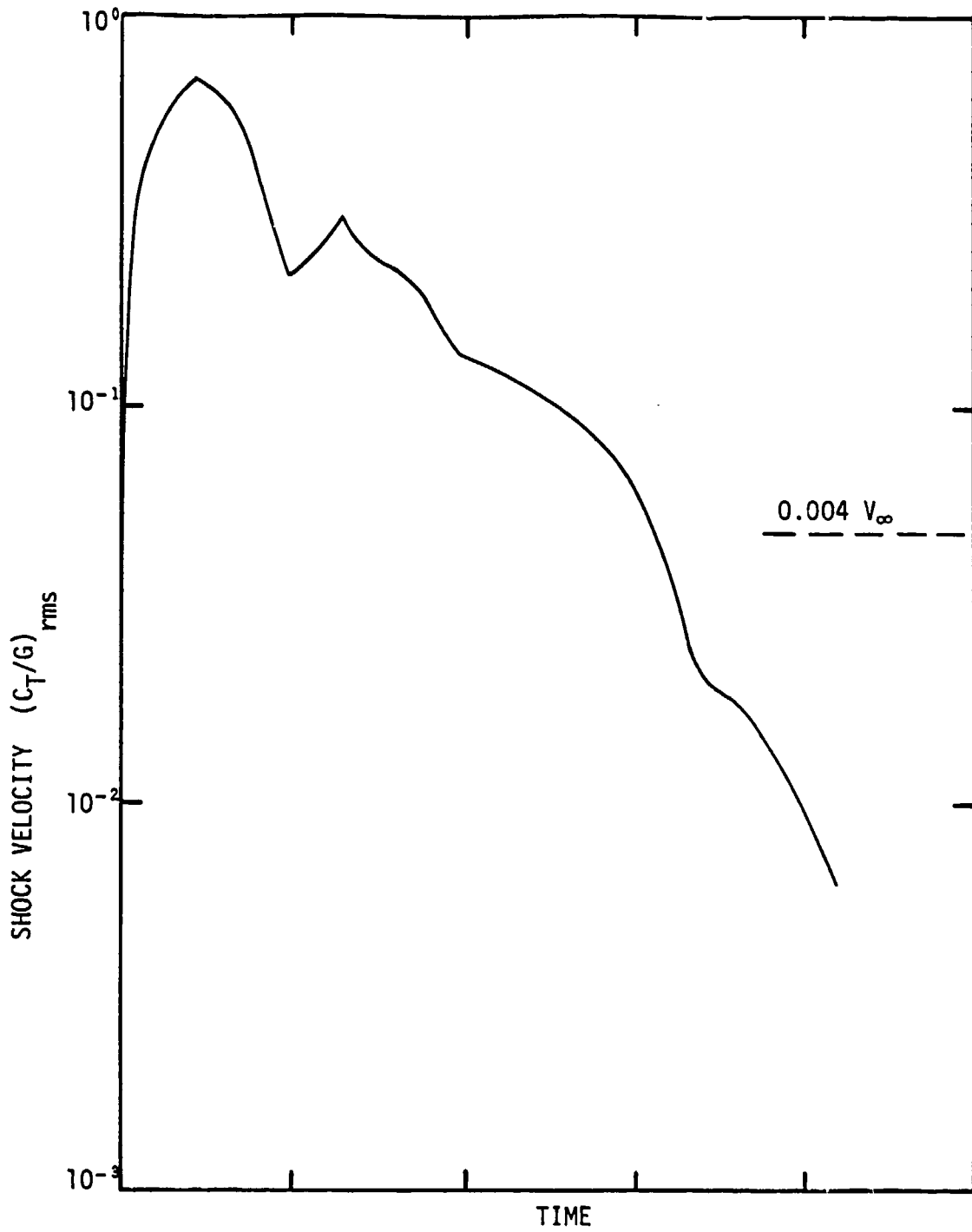


FIGURE 6.3. TYPICAL $(c_T/G)_{rms}$ HISTORY (CONVERGED)

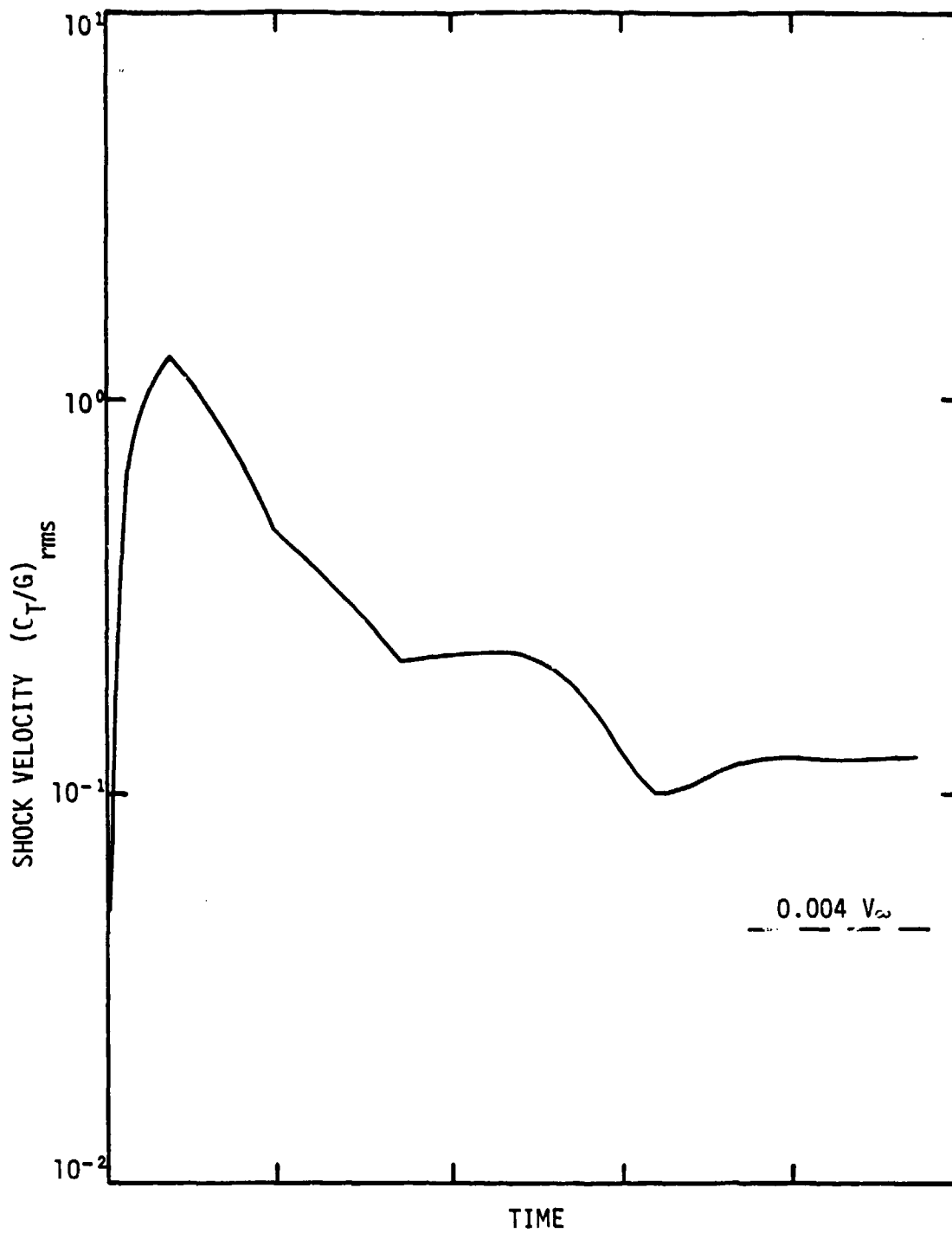


FIGURE 6.4. TYPICAL (c_T/G)_{rms} HISTORY (NOT CONVERGED)

Defining

$$\Delta H = (H - H_{\infty}) / H_{\infty} \quad (6.1)$$

a suitable criterion for convergence has been found to be

$$|\Delta H| \leq 0.05 \quad (6.2)$$

The question of convergence of the time-dependent solution can be summarized as follows: when a time-dependent solution satisfies the convergence criteria described above, it can be used with confidence to provide accurate and reliable aerodynamic predictions, provided that the mesh adequately resolves the important details of the body geometry and of the surrounding flow field.

6.3 VALIDATION OF NOSETIP SOLUTION

In this section the numerical procedures developed in this research are validated by comparisons of predictions to experimental data and, where appropriate, predictions obtained with other numerical techniques. The validation process described in this section pertains only to the noisetip solution procedures; the ability of these transonic procedures, when coupled to a steady supersonic afterbody code, to make accurate determinations of total vehicle inviscid aerodynamics is demonstrated in Section 6.4.

Two versions of the three-dimensional time-dependent inviscid code formulated in the new coordinate system (based on a series of conformal transformations) have been developed in this effort. The basic version, which is denoted by CM3DT(NC), is formulated in terms of the non-conservation dependent variables and is incapable of treating

embedded shocks. The version based on the λ -differencing scheme, providing a method for treating embedded shocks, is denoted by CM3DT(λ).

The first step in the validation process is the demonstration of the ability of the new coordinate system to permit accurate calculations of the inviscid flow over a wide variety of body shapes, including shapes that could not previously be treated with transonic codes formulated in standard coordinate systems (e.g., spherical). Use of this new coordinate system does not, however, reduce the accuracy of calculations for shapes that are well-suited to analysis using a standard coordinate system.

To illustrate the ability of the new coordinate system to treat shapes that are well-suited to calculations using a standard coordinate system, Figures 6.5 and 6.6 present predictions of the bow shock shape and surface pressure distribution for a sphere in equilibrium air at an altitude of 100 KFT with a freestream velocity of 20,000 ft/sec. Two predictions are made with the CM3DT(NC) technique, using both a coarse mesh (6 x 9; i.e., six points across the shock layer and nine points along the body) and a fine mesh (11 x 17). The other predictions shown for this flow have been obtained from the inverse technique of Lomax and Inouye³³ and from the technique developed by Kyriss and Harris⁸, which is an explicit time-dependent finite-difference code formulated in a spherical coordinate system. (The method of Kyriss and Harris has been extensively validated by comparisons to experimental data, e.g., by Hall, Kyriss, Truncellito, and Martellucci⁴ and by Hall and Nowlan⁵.)

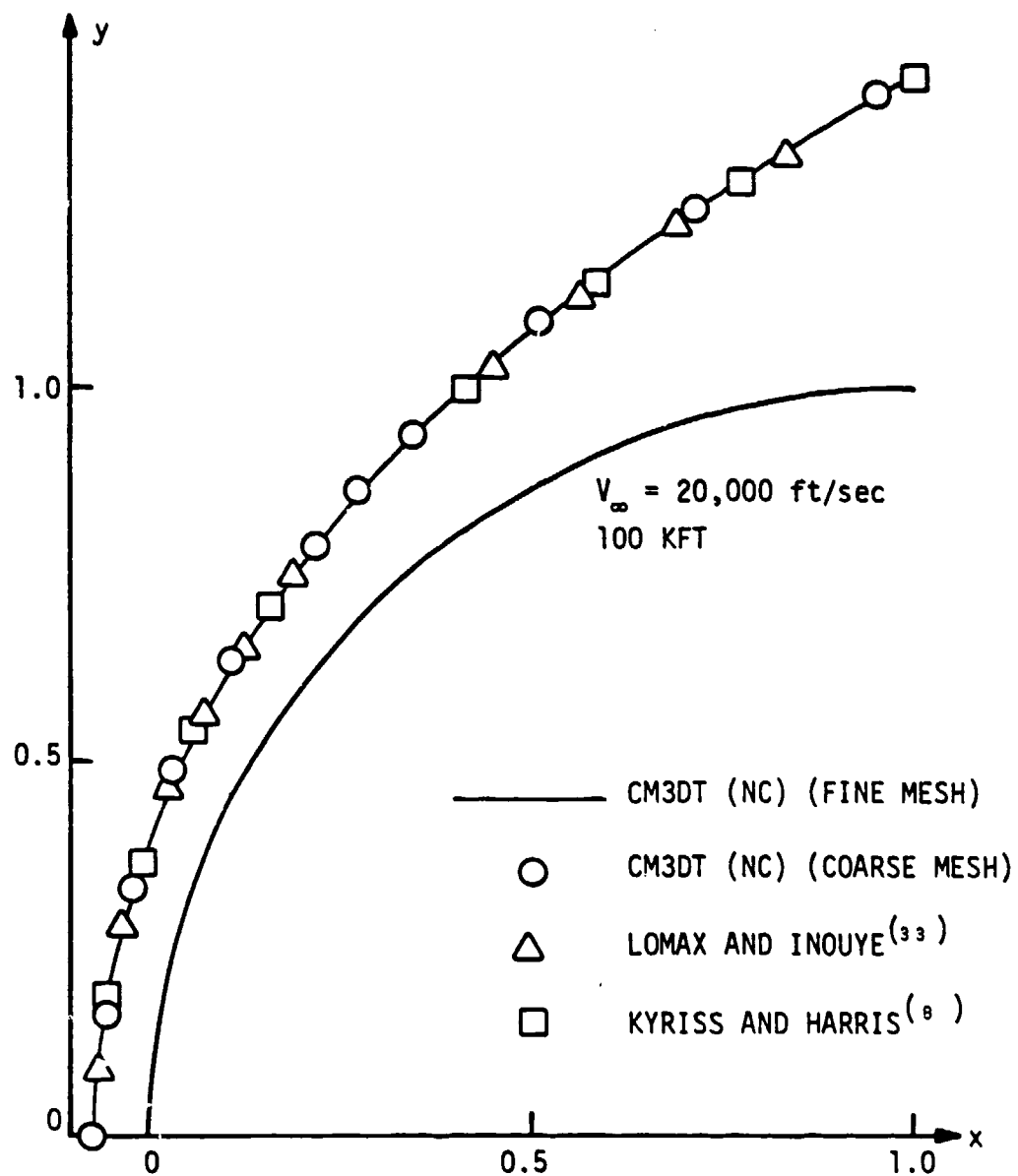


FIGURE 6.5. SHOCK SHAPE PREDICTIONS FOR A SPHERE IN EQUILIBRIUM REAL GAS

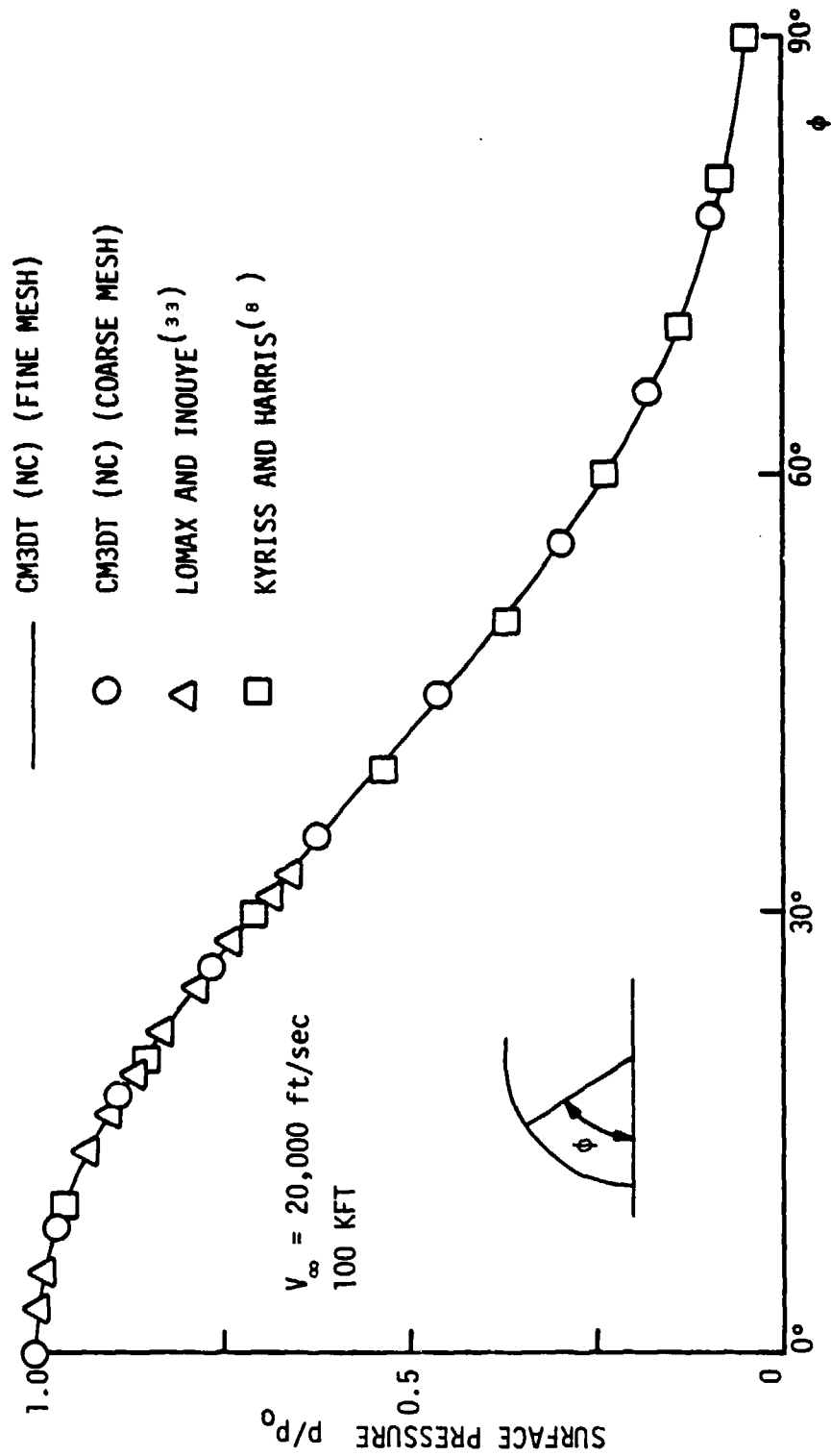


FIGURE 6.6. PREDICTIONS OF SURFACE PRESSURE DISTRIBUTION FOR A SPHERE IN EQUILIBRIUM REAL GAS

The results obtained with the CM3DT(NC) code show excellent agreement with the other predictions for this case and, furthermore, are also seen to be invariant with refinement of the mesh, verifying the consistency of the numerical approximations. This case also serves to illustrate the real gas thermodynamic capabilities of the CM3DT procedure.

The ability of the new coordinate system to treat less regular shapes is shown in Figures 6.7-6.10, which present comparisons of bow shock shape and surface pressure distribution predictions for the axisymmetric PANT Triconic (described by Jackson and Baker in Reference 21) to experimental data at $M_\infty = 5$ and $\alpha = 0^\circ$. (Although an indented shape, no embedded shock forms on this configuration at these flow conditions.) Figure 6.7 presents the surface pressure distribution predicted with the CM3DT(NC) procedure for this configuration, which has a small radius corner at the shoulder leading back to an aft cone, as evident in Figure 6.10. The agreement between the prediction and the data is seen to be good in Figure 6.7, except for oscillations arising in the vicinity of the corner. These oscillations are the result of inadequate resolution of the finite difference grid in the vicinity of the corner, as discussed and illustrated by Hall, Kyriss, Truncellito, and Martellucci¹⁴. The influence of this sharp corner is made more evident by the results obtained from a similar calculation, in which the sharp corner and cone were removed. As shown in Figure 6.8, no oscillations appear in the CM3DT(NC) prediction of surface pressure when the sharp corner is eliminated.

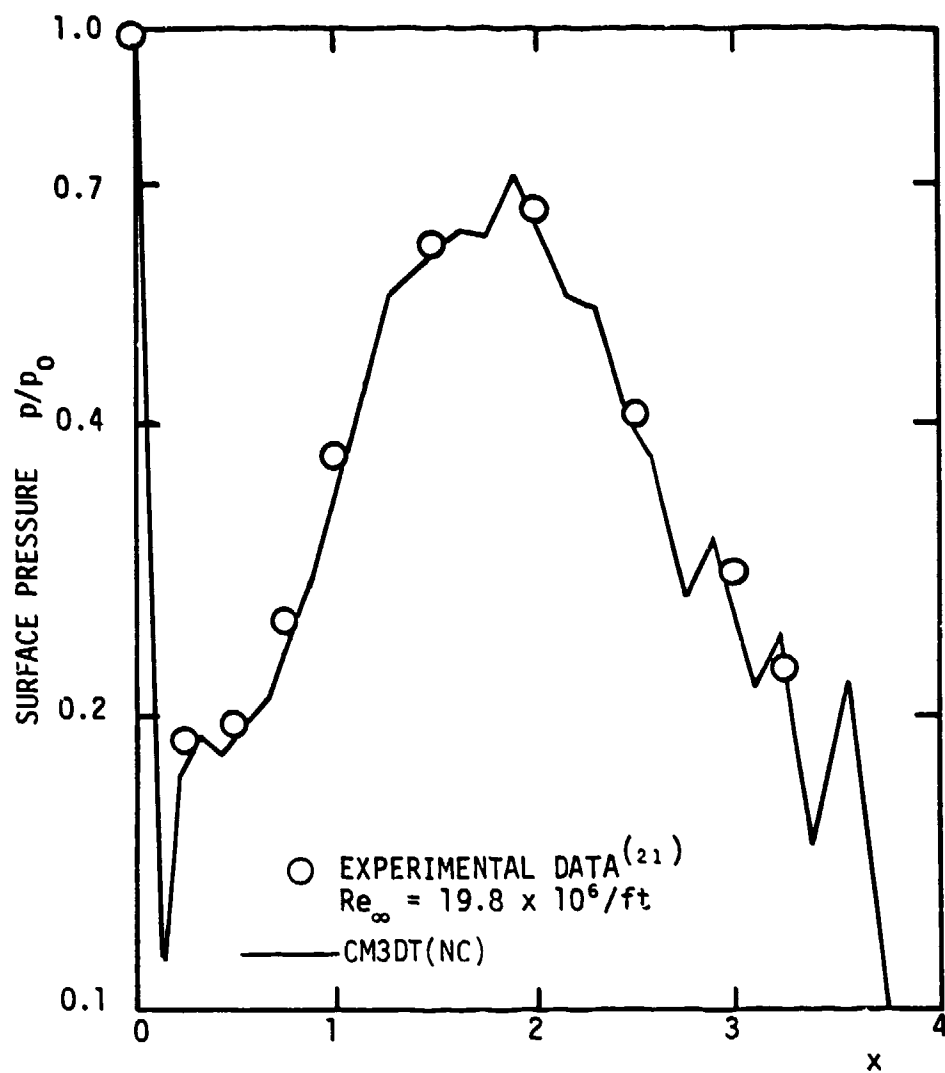


FIGURE 6.7. CM3DT (NC) PREDICTION OF SURFACE PRESSURE DISTRIBUTION FOR THE PANT TRICONIC (WITH CONE) AT $M_\infty = 5$, $\alpha = 0^\circ$

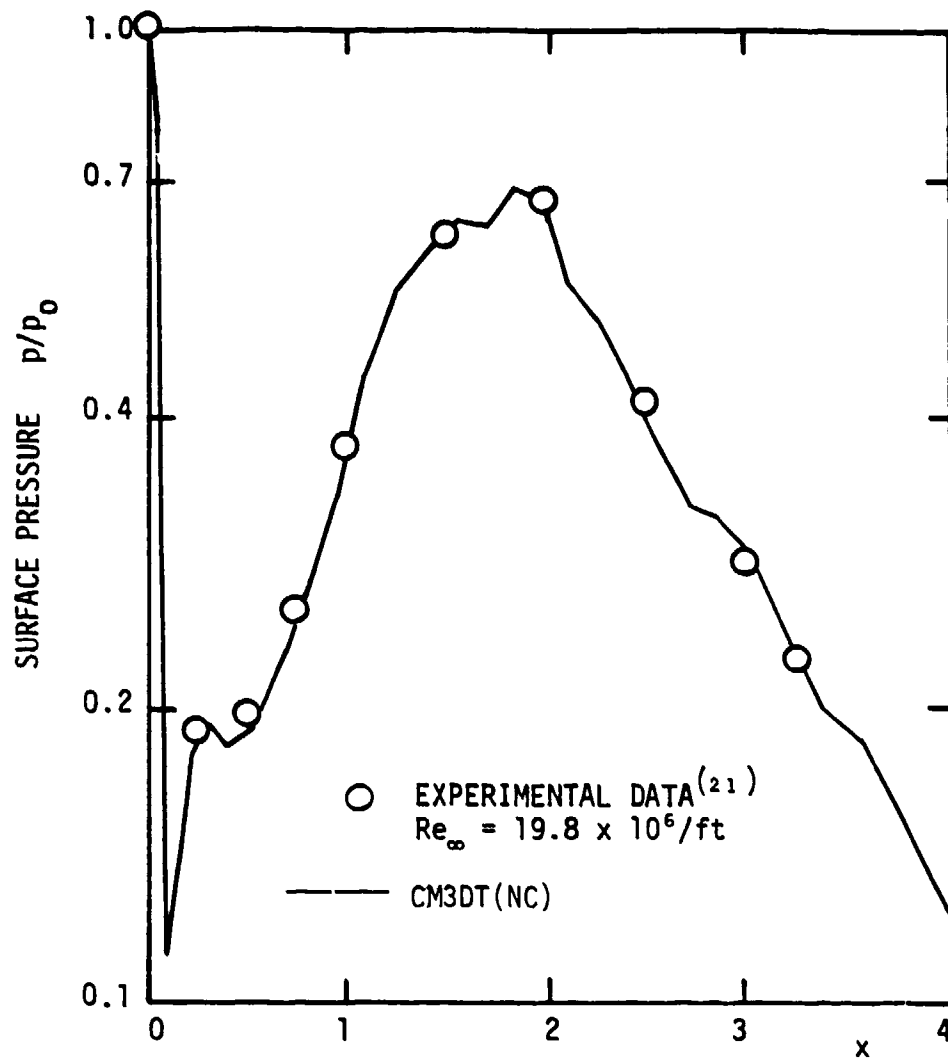


FIGURE 6.8. CM3DT (NC) PREDICTION OF SURFACE PRESSURE DISTRIBUTION FOR THE PANT TRICONIC (WITHOUT CONE) AT $M_\infty = 5$, $\alpha = 0^\circ$

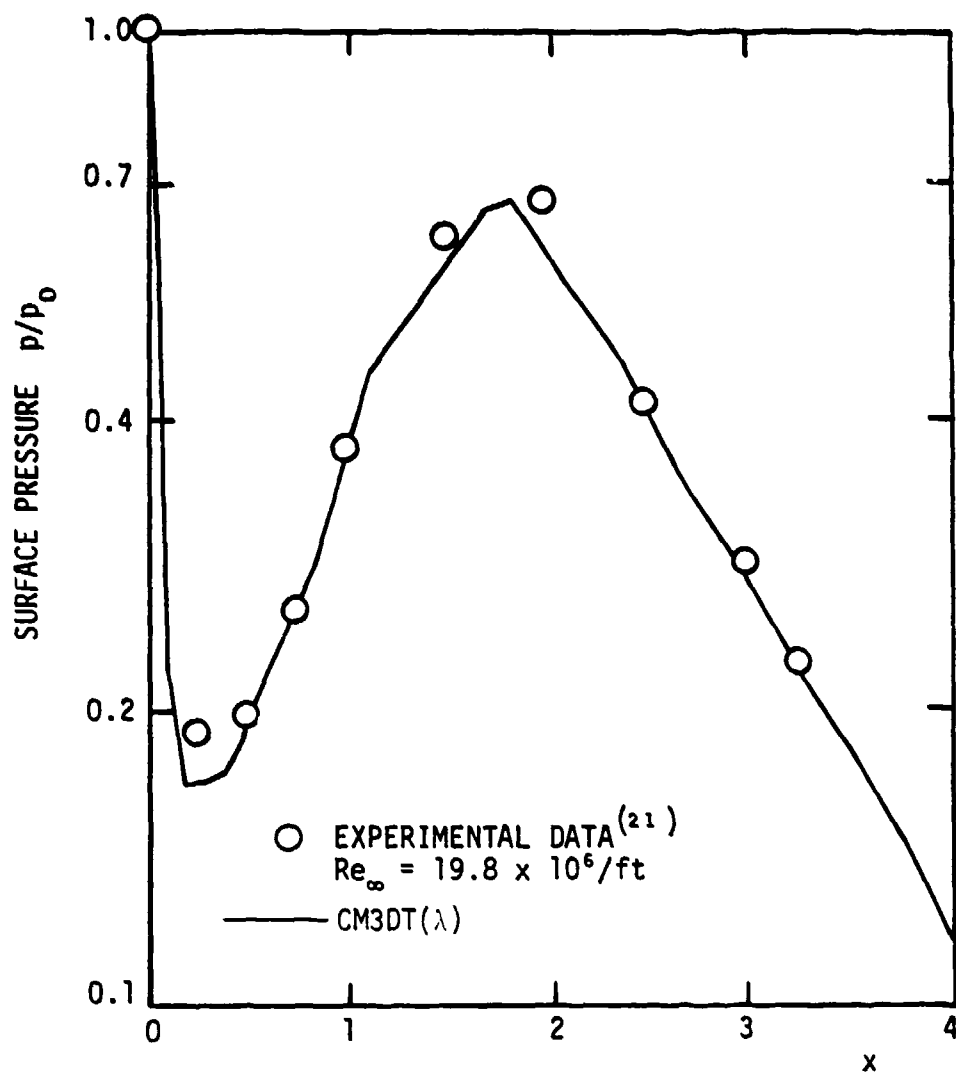


FIGURE 6.9. CM3DT (λ) PREDICTION OF SURFACE PRESSURE DISTRIBUTION FOR THE PANT TRICONIC (WITH CONE) AT $M_{\infty} = 5$, $\alpha = 0^{\circ}$

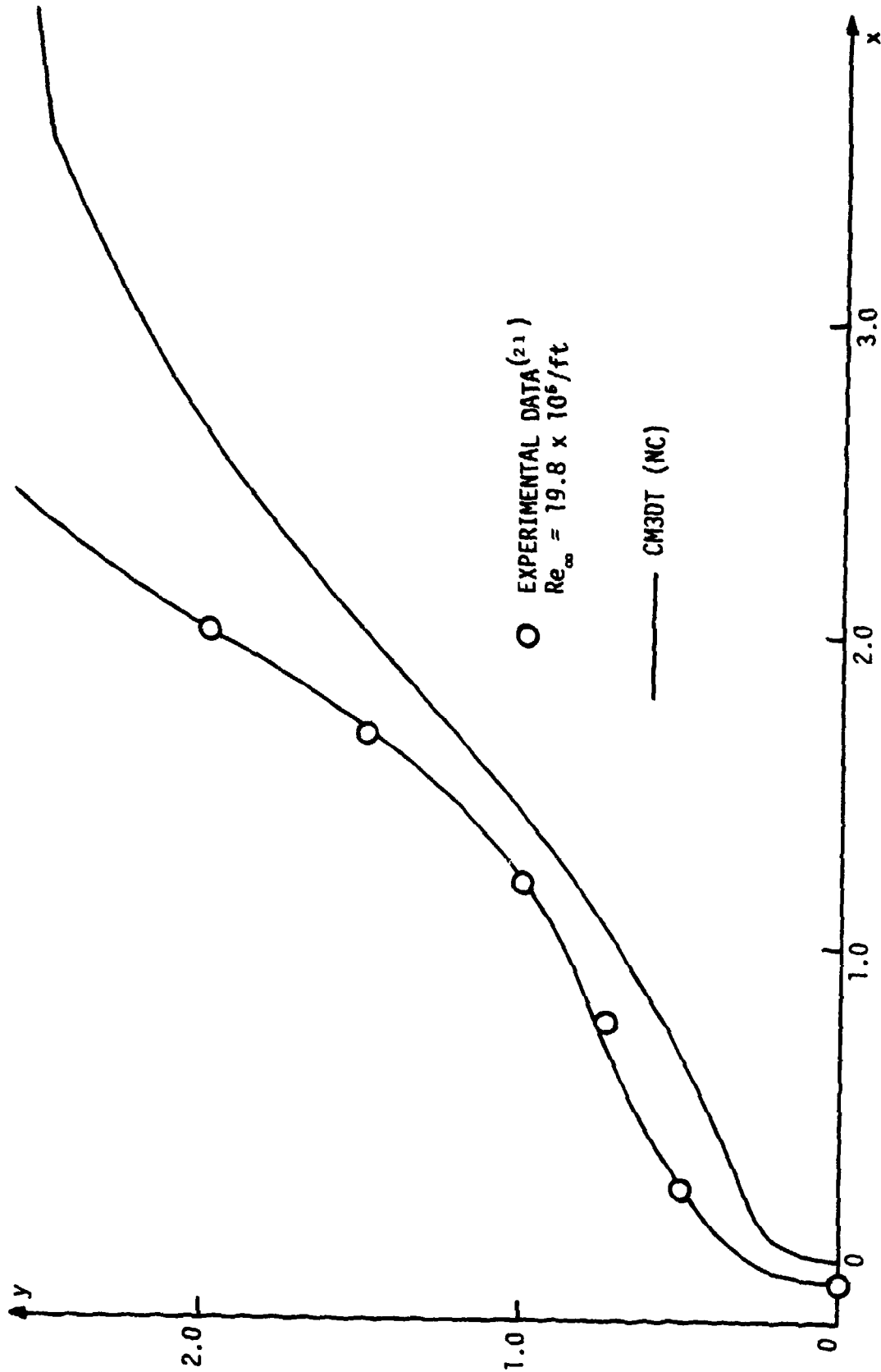


FIGURE 6.10. CM3DT SHOCK SHAPE PREDICTION FOR THE PANT TRICONIC AT $M_{\infty} = 5$, $\alpha = 0^\circ$

It was discovered during the course of this research that the λ -differencing scheme, in addition to its shock-capturing capability, has the additional ability of eliminating the spurious oscillations that arise at such sharp corners. This capability is illustrated in Figure 6.9, which depicts the surface pressure distribution for the PANT Triconic (with the sharp corner and conical aft section included) as predicted by the CM3DT(λ) procedure. The lack of oscillations in this calculation is a manifestation of the ability of the λ -differencing scheme to accurately model the physical domain of dependence, preventing oscillations from propagating upstream in supersonic flow.

The final comparison for the PANT Triconic predictions is shown in Figure 6.10, demonstrating the agreement between predictions and experimental data for the bow shock shape. (All CM3DT predictions, both with and without the sharp corner, for the bow shock shape are essentially equivalent.)

It should be noted that attempts at computing this slender shape with the technique of Kyriss and Harris⁸, which is formulated in a spherical coordinate system, were unsuccessful, because of the inability of the spherical coordinate system to be closely aligned with the body geometry.

Further evidence of the abilities of the new coordinate system is provided in Figure 6.11, which presents a comparison of surface pressure predictions and experimental data for the PANT Simple Biconic (described by Jackson and Baker²¹) at $M_\infty = 5$ and $\alpha = 5^\circ$. This axisymmetric configuration is a 45° sphere-cone nosetip, with a rounded shoulder leading to a 6° aft cone. As seen in this figure, the

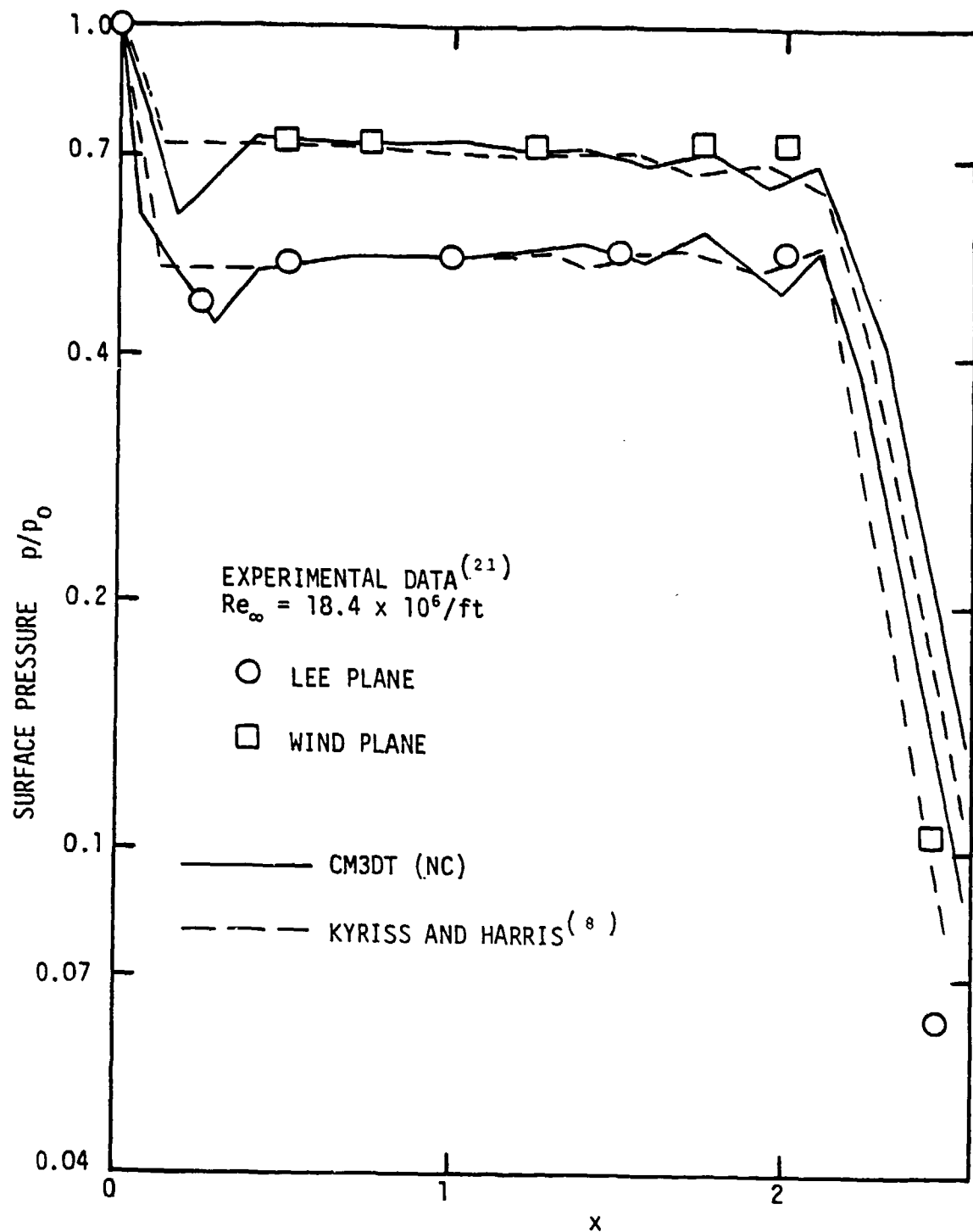


FIGURE 6.11. SURFACE PRESSURE PREDICTIONS FOR THE PANT SIMPLE BICONIC AT $M_\infty = 5$, $\alpha = 5^\circ$

predictions of both CM3DT(NC) and the technique of Kyriss and Harris² show good agreement with the data, except for the oscillations created by the lack of adequate resolution at the shoulder. Not apparent from this figure, however, is the improved convergence behavior obtained with the new transonic technique. After 400 time steps, using the same number of grid points, and computing approximately the same elapsed physical time, the root-mean-squares of the shock velocities, which, as discussed in Section 6.2, are reliable indicators of convergence, differ by an order of magnitude. For CM3DT(NC), $(c_T/G)_{rms}/V_\infty = 0.004$, while the equivalent quantity for the other technique is 0.056, which does not satisfy the convergence criterion.

Another good indicator of convergence for a time-dependent technique is the maximum error in computed total enthalpy. For CM3DT(NC), the maximum error is 8.6% for this case, compared to a maximum error of 28.5% for the technique of Kyriss and Harris, further illustrating the benefits of the new coordinate system.

The ability of the CM3DT(NC) code to treat asymmetric shapes at angle of attack using the new coordinate system is illustrated in Figure 6.12, showing predictions of the bow shock shape for the Blunt-1 shape at $M_\infty = 13.4$ and $\alpha = 3^\circ$. (This asymmetric nosetip shape was derived in a nosetip reconstruction analysis described by Hall and Nowlan⁵.) The predicted shock shape is seen to agree well with that predicted using the technique of Kyriss and Harris⁸.

The final step in the validation process for the nosetip solution is the demonstration of the ability of the CM3DT(λ) procedure to predict flows over shapes that produce an embedded shock. In Figure

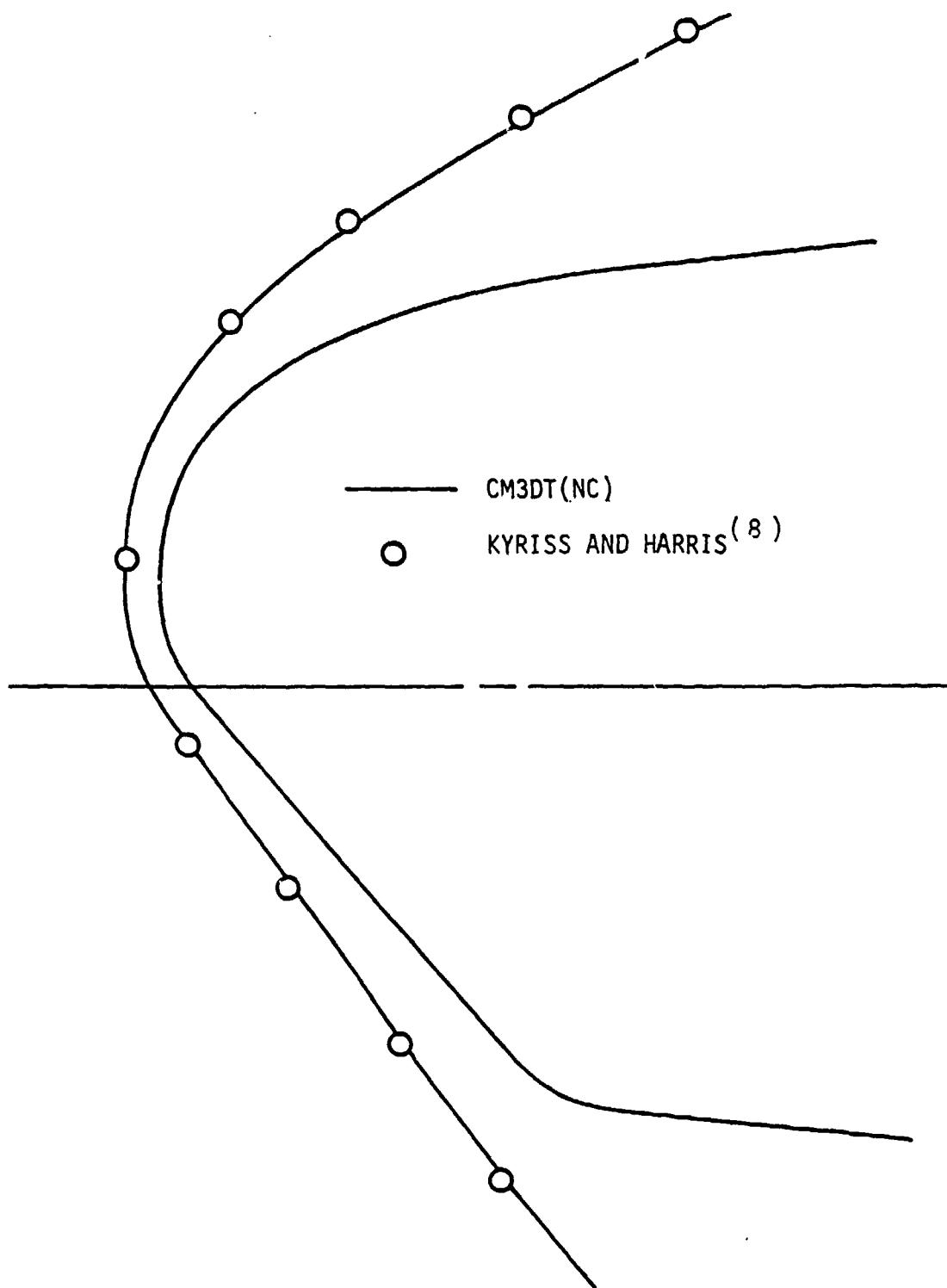


FIGURE 6.12. BOW SHOCK SHAPE PREDICTIONS FOR THE BLUNT-1 SHAPE AT $M_\infty = 13.4$, $\alpha = 3^\circ$

6.13, a comparison is shown of the predicted surface pressure distribution and the experimental data for the PANT Triconic at $M_\infty = 5$ and $\alpha = 10^\circ$; the agreement is seen to be excellent. Schlieren photographs of this configuration at this angle of attack, which may be found in Reference 21, clearly indicate the presence of an embedded shock in the lee plane. This comparison serves to illustrate the capability of the three dimensional version of the λ -differencing scheme to compute inviscid nosetip flow fields with embedded shocks. (The capabilities of the axisymmetric version of the λ -differencing scheme have been demonstrated in Section 4.)

6.4 PREDICTION OF TOTAL VEHICLE INVISCID AERODYNAMICS

In the preceding section the ability of the CM3DT technique to accurately predict inviscid flow fields over ablated reentry vehicle nosetips has been demonstrated. To complete the validation process for this technique, it remains only to demonstrate the capability of the CM3DT nosetip code, when coupled with an existing supersonic afterbody code, to make accurate predictions of total vehicle inviscid aerodynamics. For this validation effort, the CM3DT code has been coupled to the supersonic afterbody code of Kyriss and Harris⁹, which is a steady, forward marching finite difference technique formulated in a cylindrical coordinate system. (Coupling of the nosetip and afterbody codes requires interpolation on the nosetip solution to determine the flow variables in the initial data plane of the afterbody solution and an integration to determine the forces and moments acting on the nosetip.)

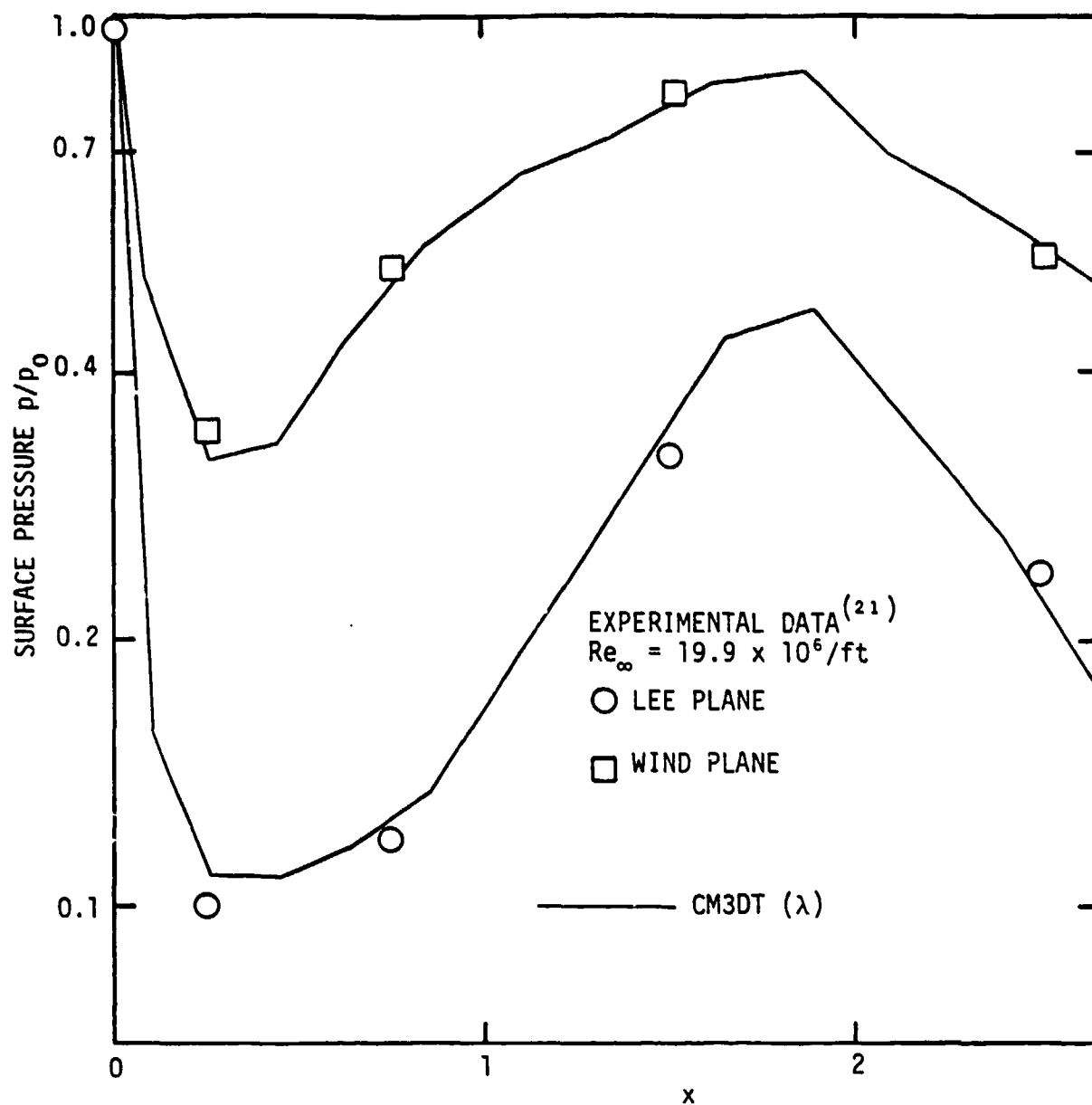


FIGURE 6.13. SURFACE PRESSURE PREDICTIONS FOR THE PANT TRICONIC AT $M_{\infty} = 5$, $\alpha = 10^{\circ}$

In the calculation of total vehicle aerodynamics it is of critical importance to accurately model the influence of the nosetip shape on the afterbody flow field, and thus on the resulting forces and moments acting on the vehicle. For example, the importance of the downstream influence of an asymmetric nosetip in the determination of the trim angle of attack (α_T) for a ballistic reentry vehicle has been demonstrated by Hall and Nowlan⁵. Direct coupling of numerical flow field calculations for nosetips with afterbody procedures will automatically include the nosetip's influence on the afterbody flow field.

The first validation case for the CM3DT code coupled to the afterbody solution is presented in Figure 6.14. This figure depicts a comparison of predictions of the normal force coefficient (C_N) and the pitching moment coefficient (C_m) as a function of angle of attack for a 9° cone with a spherical nose, with a vehicle bluntness ratio (R_N/R_B) of 15%, at $M_\infty = 20$ in ideal gas ($\gamma = 1.4$) with no sideslip ($\beta = 0^\circ$). The prediction labeled CM3DT was obtained using the CM3DT(NC) code to provide the initial data required for the Kyriss and Harris⁸ afterbody code; the other prediction was obtained using an axisymmetric calculation of the spherical nosetip flow field (in wind-fixed coordinates), with the required initial data being obtained by suitable rotations of the spherical solution, as described in Reference 8. The accuracy of the Kyriss and Harris afterbody code, and of the Kyriss and Harris axisymmetric and three-dimensional transonic codes for blunt, convex nosetips, has been extensively demonstrated through comparisons of predictions to wind tunnel data, as shown, for example, in References

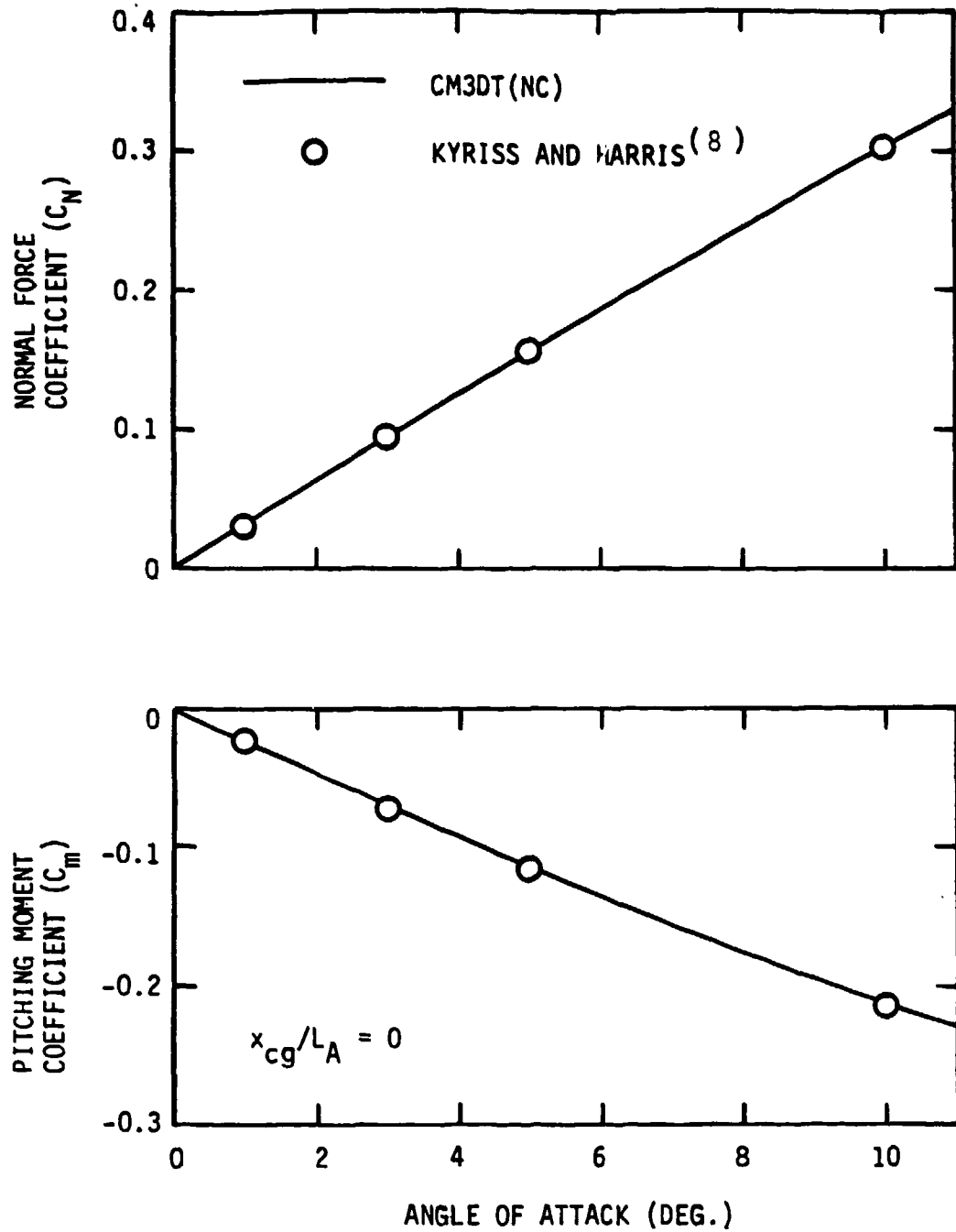


FIGURE 6.14. NORMAL FORCE AND PITCHING MOMENT COEFFICIENTS VS. ANGLE OF ATTACK FOR 9° SPHERE-CONE OF 15% BLUNTNES AT $M_\infty = 20$, $\beta = 0^\circ$

4, 5, and 8. As is evident in Figure 6.14, the agreement between the predictions of $C_N(\alpha)$ and $C_m(\alpha)$ is excellent.

The comparison of aerodynamic predictions for spherically blunted cones obtained with these two techniques is continued in Figure 6.15. This figure illustrates the excellent agreement obtained between the two predictions of pitch center of pressure as a function of bluntness ratio for the 9° sphere-cone at $M_\infty = 20$ and $\alpha = 5^\circ$. (The pitch center of pressure is defined as $x_{cp}/L_A = x_{cg}/L_A - C_m/C_N$ when the reference length used in the non-dimensionalization of the pitching moment is the virtual cone length.)

The ability of CM3DT to provide accurate initial data to the afterbody calculation for spherically-nosed vehicles is further demonstrated in Figure 6.16. This comparison is similar to that shown in Figure 6.14, in that predictions are obtained for $C_N(\alpha)$ and $C_m(\alpha)$ for a 15% blunt 9° sphere-cone at $M_\infty = 20$, except that the vehicle is at a constant sideslip angle (β) of 5° . The agreement between the two predictions is again seen to be excellent, and serves to verify the ability of the CM3DT to compute flow fields on nosetips in both pitch and yaw.

Figures 6.17 and 6.18 present a comparison of inviscid aerodynamic predictions obtained for a vehicle with a blunt asymmetric nosetip. The vehicle is a 6° cone with a nominal bluntness ratio of 25%; the nosetip is the Blunt-1 shape (illustrated in Figure 6.12), which was derived in a nosetip shape reconstruction effort described by Hall and Nowlan⁵. (In Reference 5, the Blunt-1 shape was selected as a plausible nosetip shape for an actual flight vehicle at 20 KFT, based on actual recession

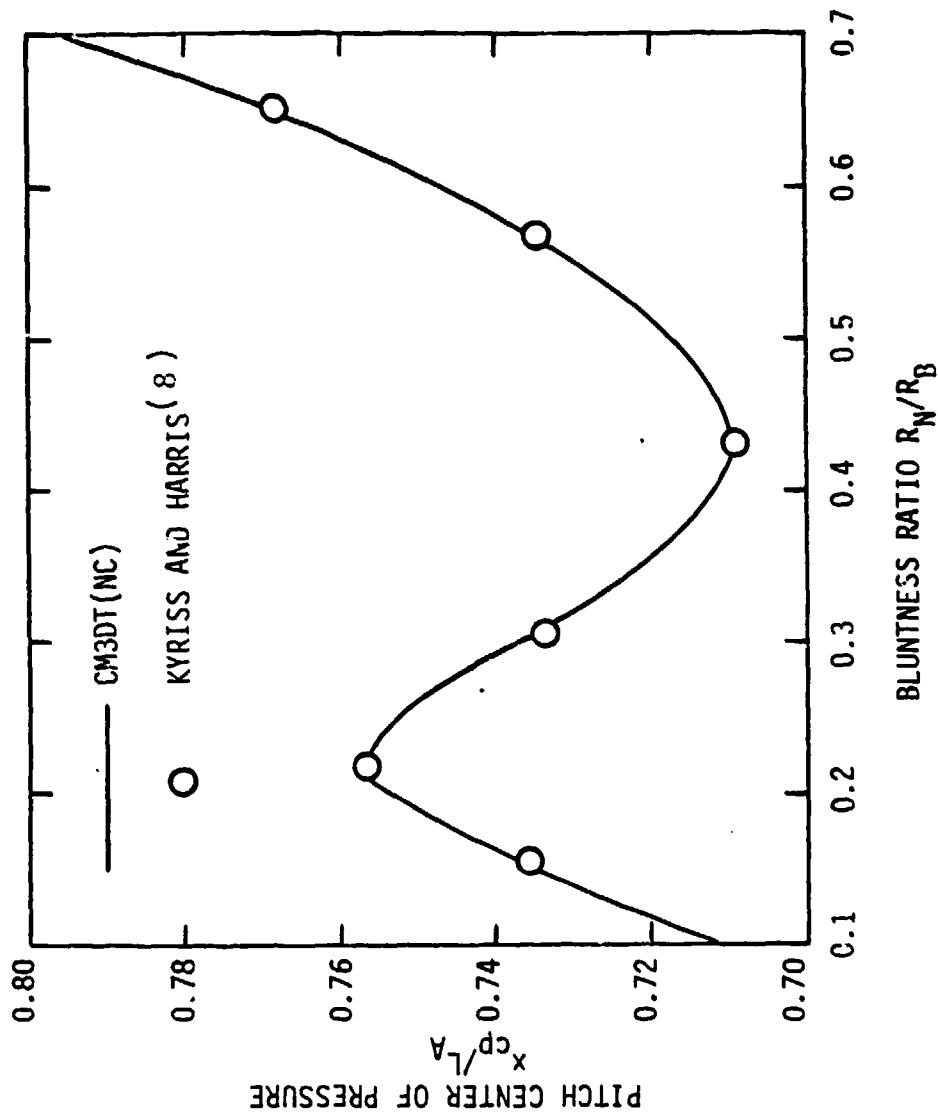


FIGURE 6.15. PITCH CENTER OF PRESSURE VS. BLUNTNES RATIO FOR 9° SPHERE-CONE AT $M_\infty = 20$, $\alpha = 5^\circ$, $\beta = 0^\circ$

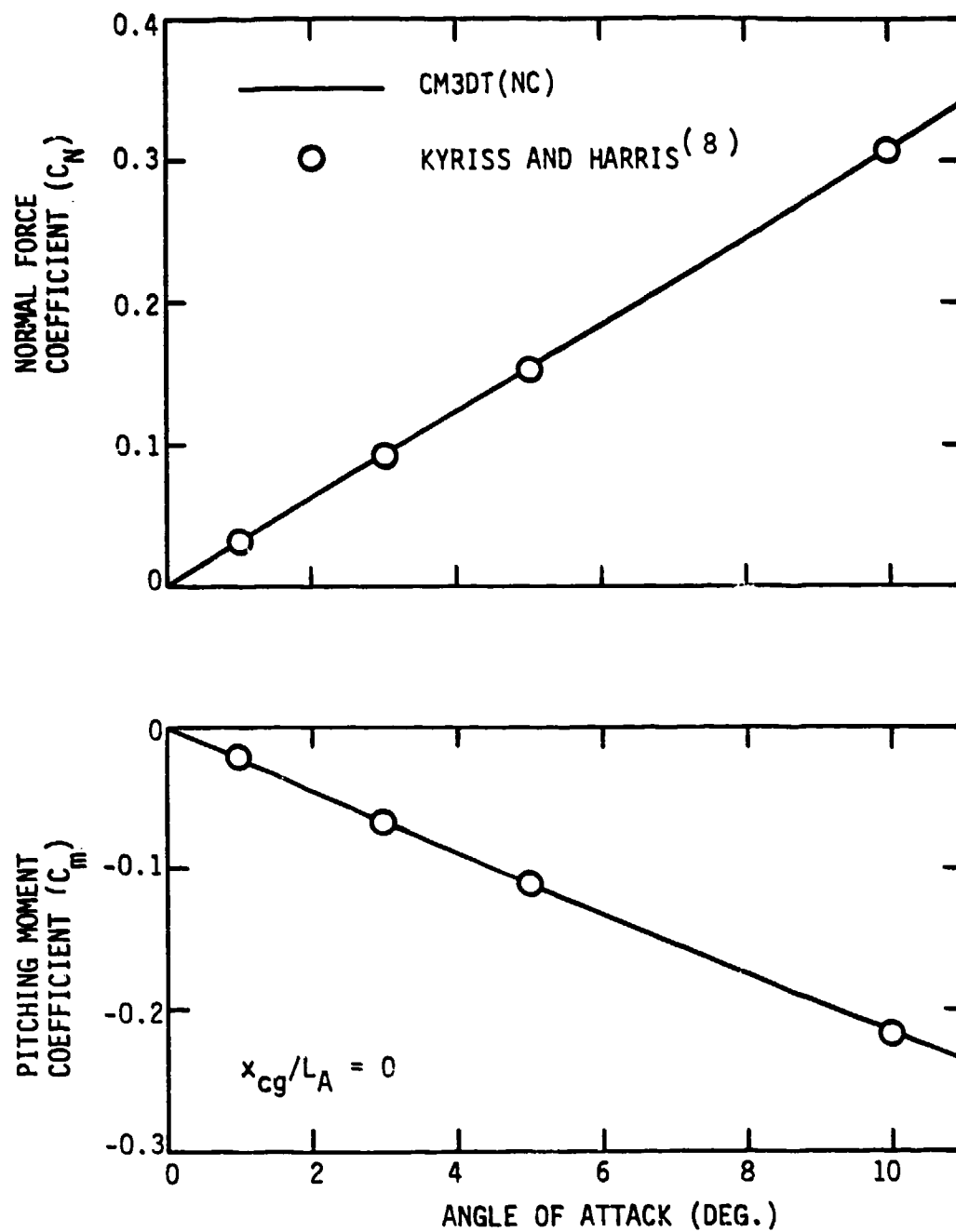


FIGURE 6.16. NORMAL FORCE AND PITCHING MOMENT COEFFICIENTS VS. ANGLE OF ATTACK FOR 9° SPHERE-CONE OF 15% BLUNTNES AT $M_\infty = 20$, $\beta = 5^\circ$

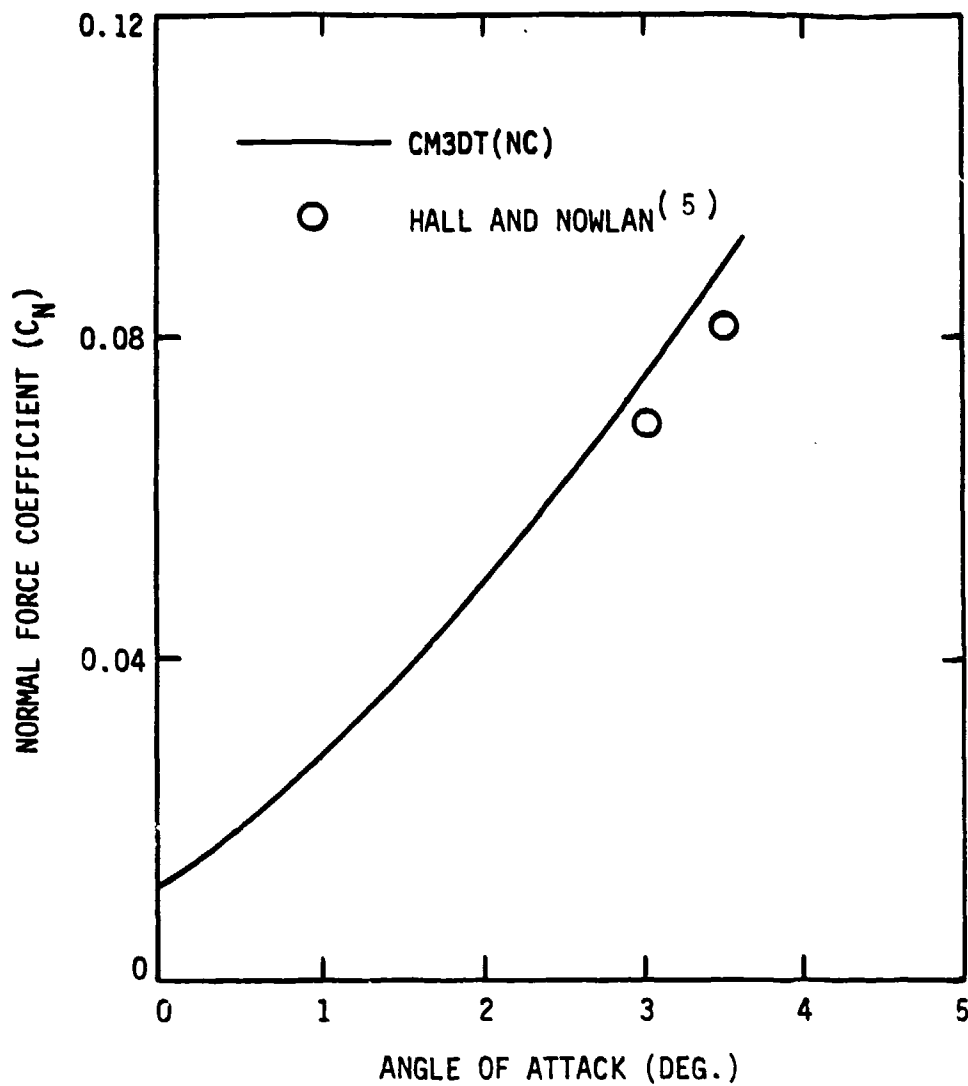


FIGURE 6.17. NORMAL FORCE COEFFICIENT VS. ANGLE OF ATTACK FOR BLUNT-1 CONFIGURATION AT $M_\infty = 13.4$, 20 KFT ALTITUDE

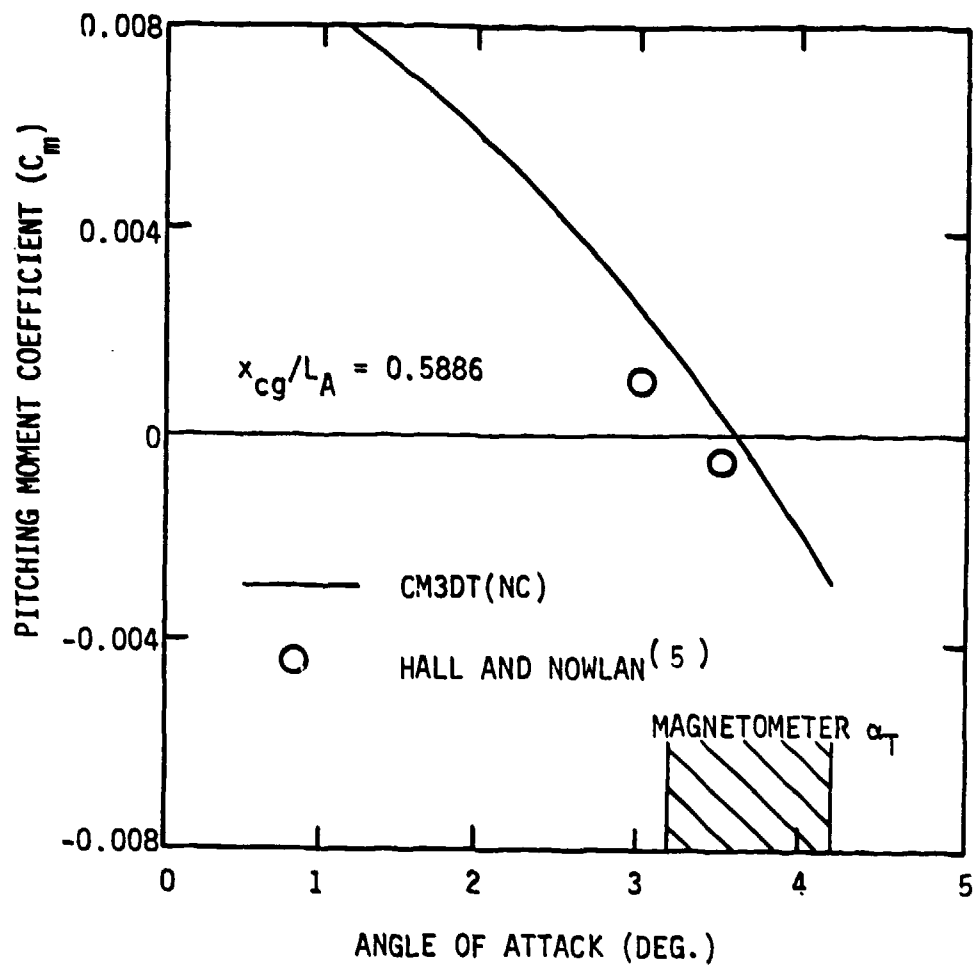


FIGURE 6.18. PITCHING MOMENT COEFFICIENT VS. ANGLE OF ATTACK FOR BLUNT-1 CONFIGURATION AT $M_\infty = 13.4$, 20 KFT ALTITUDE

measurements and on the consistency of aerodynamic characteristics derived from motion data with those computed with the transonic nosetip and supersonic afterbody codes of Kyriss and Harris⁹. The computed trim angle of attack, $\alpha_T = 3.35^\circ$, was consistent with that measured by an onboard magnetometer, as indicated in Figure 6.18.)

A comparison of $C_N(\alpha)$ predictions for this configuration is presented in Figure 6.17, and fair agreement is evident between the predictions obtained with the CM3DT(NC) technique and with the three-dimensional transonic code of Kyriss and Harris. Similar agreement is seen in the $C_m(\alpha)$ predictions shown in Figure 6.18. The CM3DT predictions indicate a trim angle of attack of 3.58° , which is within the α_T range measured by the magnetometer.

The above comparisons have demonstrated the ability of the CM3DT code to produce nosetip flow field solutions and afterbody solution initial data for spherical and blunt convex nosetip shapes with an accuracy equivalent to that of the extensively validated transonic technique of Kyriss and Harris⁹. Because the CM3DT code has been developed to extend the range of nosetip geometries for which accurate numerical inviscid aerodynamic predictions can be made, however, the remaining validation cases to be documented in this section must rely on comparisons of CM3DT solutions with wind tunnel data for complete reentry vehicles, rather than with other numerical solutions.

The first case to be considered in this comparison of numerical predictions and experimental data is the N8 nosetip, shown in Figure 6.19, mounted on a 6.3° cone, with a nominal bluntness of 25%.

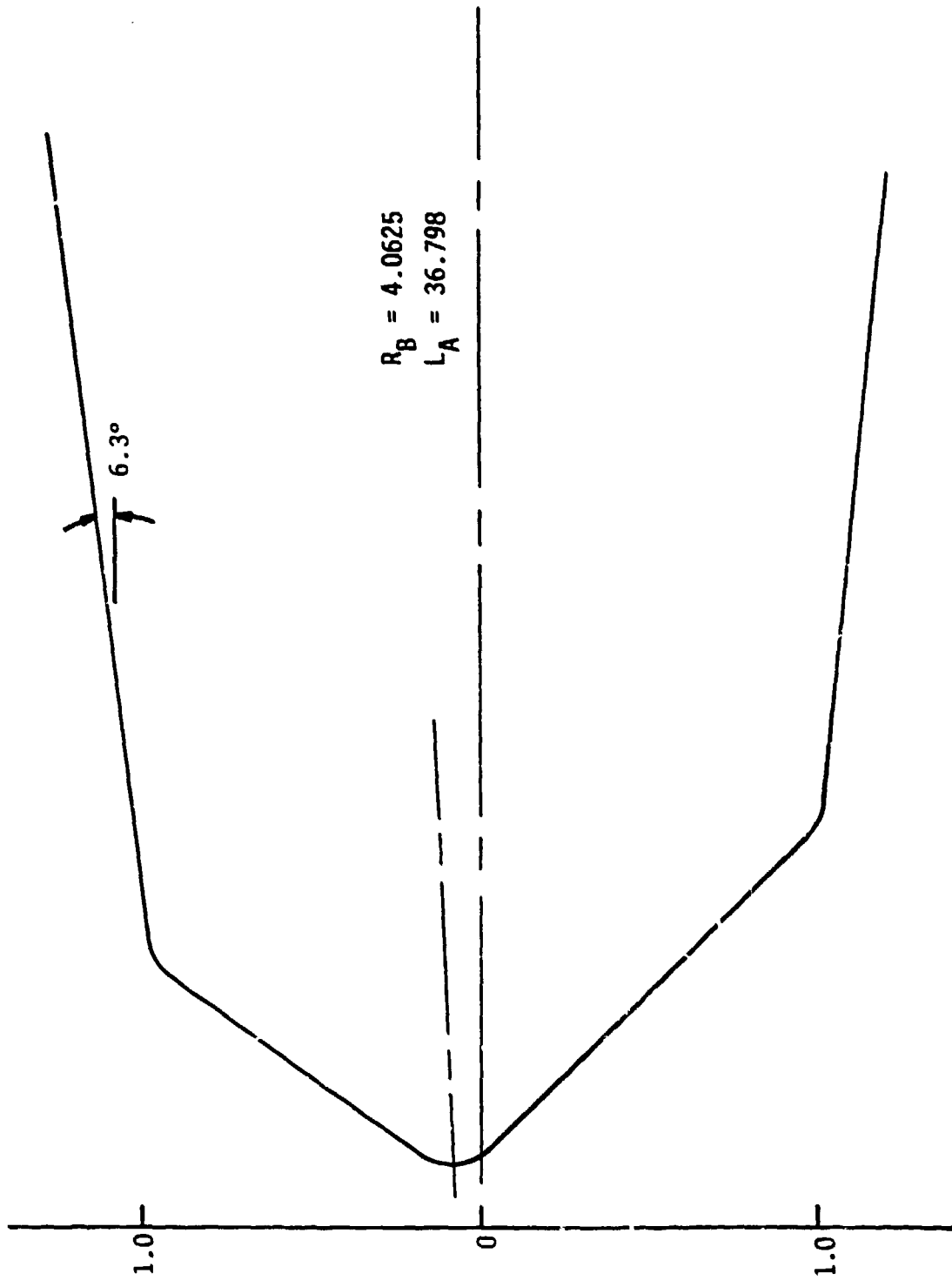


FIGURE 6.19. N8 CONFIGURATION

Experimental data were obtained at Mach 8 in Tunnel B at the Arnold Engineering Development Center (AEDC); details of the tests and the resulting data are described by Hahn and Little³⁴. The N8 nosetip is a "tilted cone" shape, with relatively small shoulder radii, and is intended to simulate an asymmetric shape that could result from turbulent ablation on the nose. Because of the fairly sharp corners on this shape, the CM3DT(λ) code was used to generate the nosetip flow field solution, since the λ -differencing scheme has been found to eliminate wiggles arising at sharp corners, as discussed in Section 6.3.

Comparisons of the predictions of the normal force and pitching moment coefficients to the experimental data are shown in Figures 6.20 and 6.21, respectively. These comparisons show good agreement between the predictions and the data. Also, the CM3DT technique has accurately computed the trim angle of attack to be 3.86° (based on a linear interpolation between values of C_m computed at $\alpha = 2^\circ$ and $\alpha = 4^\circ$), compared to the experimentally determined value of 3.52° (based on a linear interpolation between data points at $\alpha = 3^\circ$ and $\alpha = 4^\circ$).

The final validation cases to be presented in this section involve comparisons between predictions and tunnel measurements of aerodynamic forces and moments for a 6° cone (25% nominal bluntness) with two axisymmetric indented nosetips. The tests were conducted in Tunnel F at AEDC at a Mach number of 11.6 and are described by Boudreau, Crain, and Edenfield³⁵. The nosetips tested were the Very Mildly Indented Body (VMIB) and the Mildly Indented Body (MIB), described by Reeves, Todisco, Lin, and Pallone²⁰, and illustrated in Figures 4.4 and 4.7, respectively.

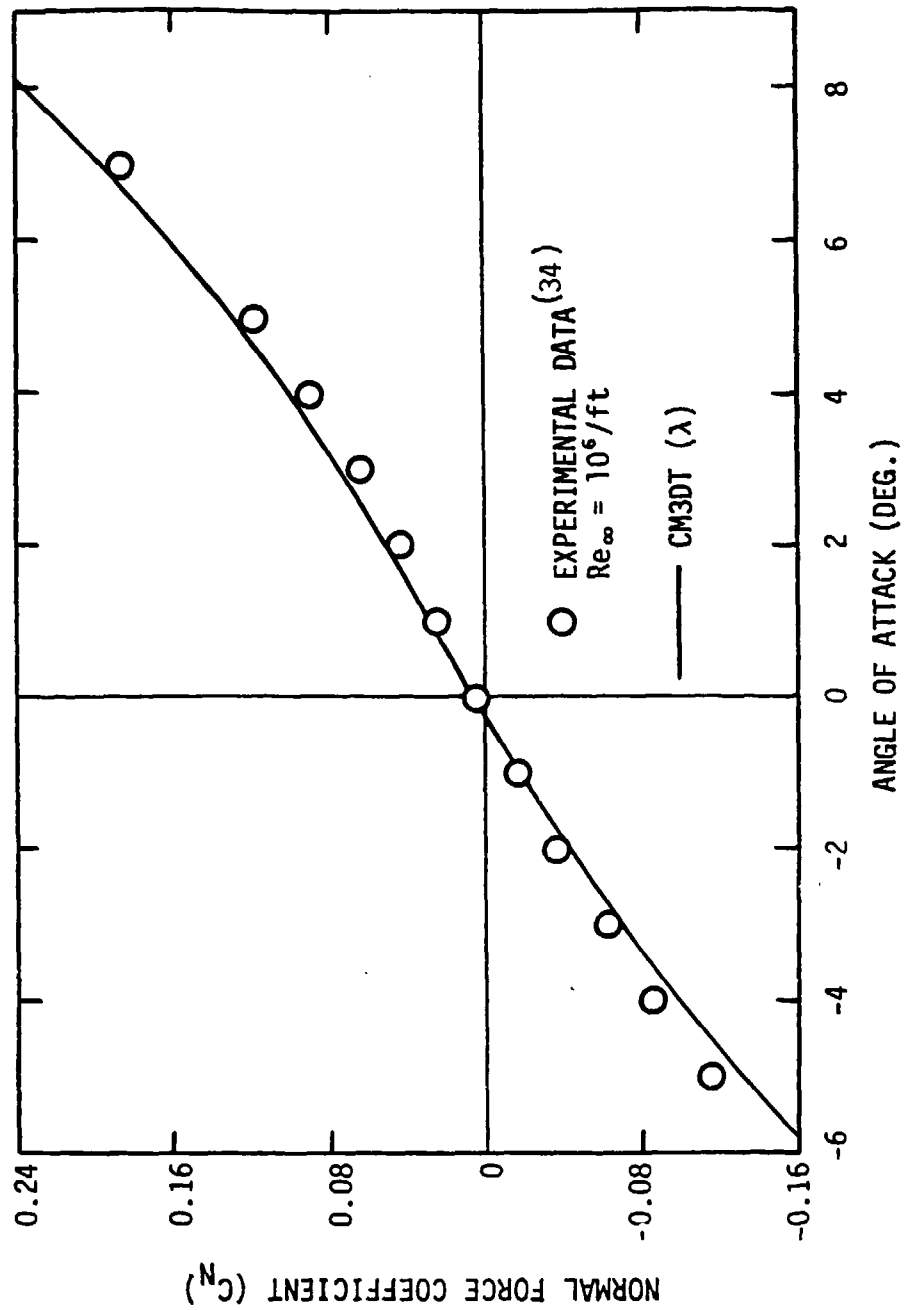


FIGURE 6.20. NORMAL FORCE COEFFICIENT VS. ANGLE OF ATTACK
 FOR N8 CONFIGURATION AT $M_\infty = 8$

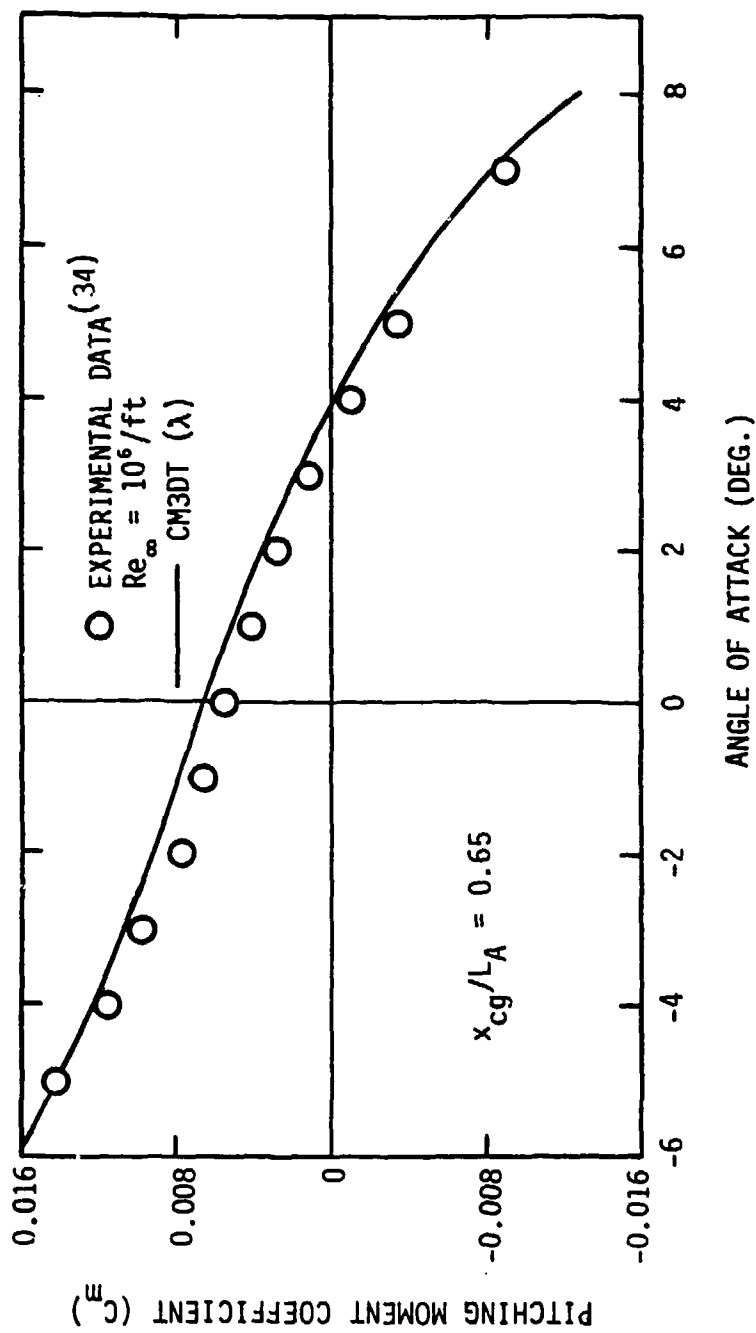


FIGURE 6.21. PITCHING MOMENT COEFFICIENT VS. ANGLE OF ATTACK FOR N8 CONFIGURATION AT $M_\infty = 8$

Since both the VMIB and MIB nosetips are indented and tests were conducted at non-zero angles of attack, it was necessary to use the CM3DT(λ) code because of the shock-capturing capability of the λ -differencing scheme for the treatment of embedded shocks. Figures 6.22 and 6.23 present comparisons of $C_N(\alpha)$ and $C_m(\alpha)$ predictions to the data, respectively, for the VMIB nosetip, and the agreement is seen to be excellent.

The same comparisons are presented in Figures 6.24 and 6.25 for the vehicle with the MIB nosetip. Again, the overall agreement between the predictions and the data is seen to be good. (Discrepancies are apparent, however, between the predicted and measured values of C_N and C_m at $\alpha = 4^\circ$ for this configuration. The validity of the CM3DT calculation at this angle of attack, as measured by the convergence of the computation, is comparable to that of the calculations at other angles of attack, where good agreement between predictions and data is evident.)

Further validation of the VMIB and MIB calculations is presented in Figure 6.26, which depicts the predicted pitch center of pressure locations compared to the experimental center of pressure data presented in Reference 8. The agreement is seen to be excellent.

In conclusion, the ability of the CM3DT(λ) code to compute inviscid flow fields on indented nosetips at angle of attack, when coupled with a supersonic afterbody code, has resulted in a technique that is capable of producing accurate aerodynamic predictions for reentry vehicles with realistic ablated nosetip shapes, as demonstrated above. This capability represents a significant extension of the applicability of numerical techniques to the evaluation of reentry vehicle inviscid aerodynamics.

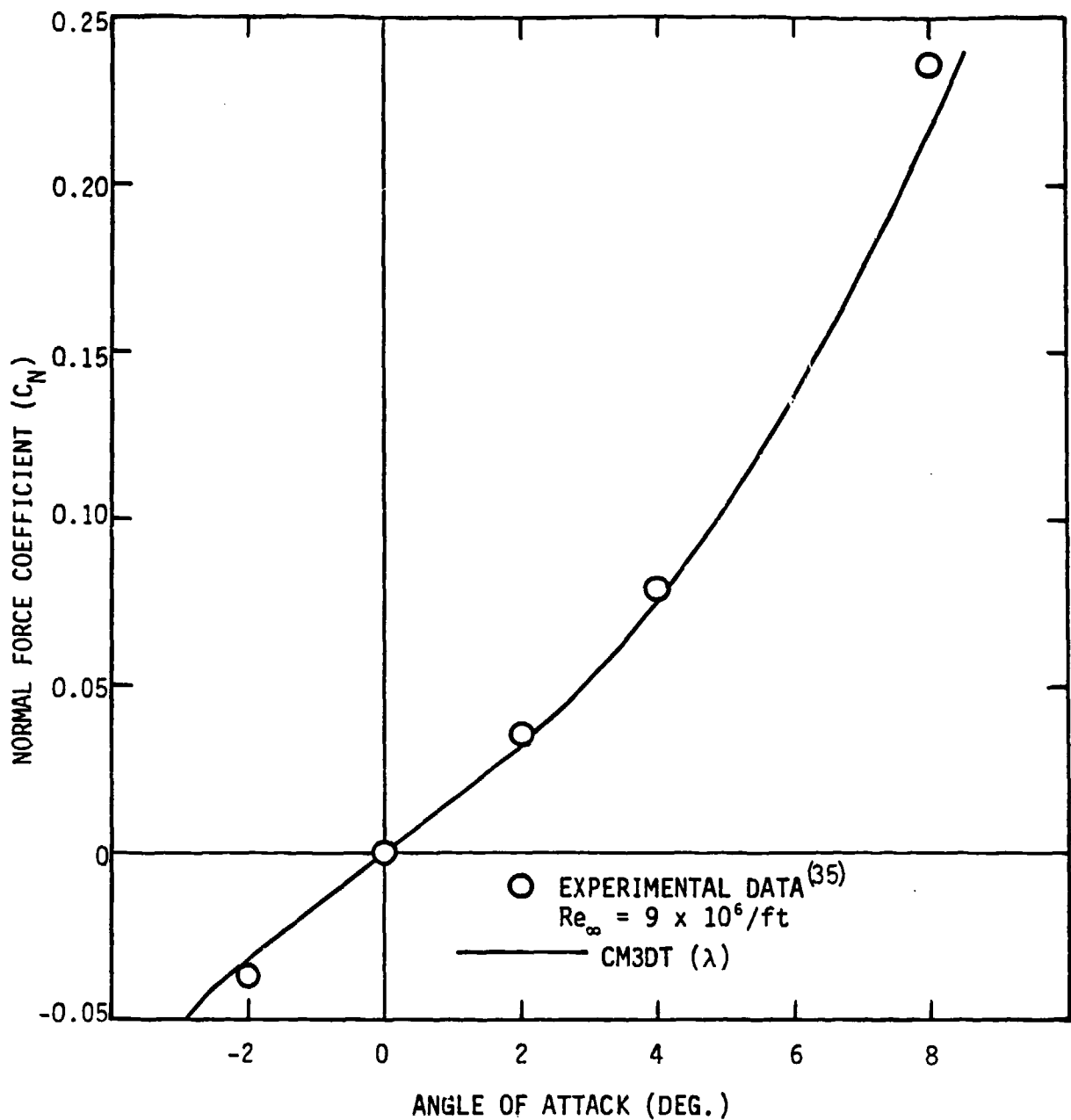


FIGURE 6.22. NORMAL FORCE COEFFICIENT VS. ANGLE OF ATTACK FOR VMIB CONFIGURATION AT $M_\infty = 11.6$

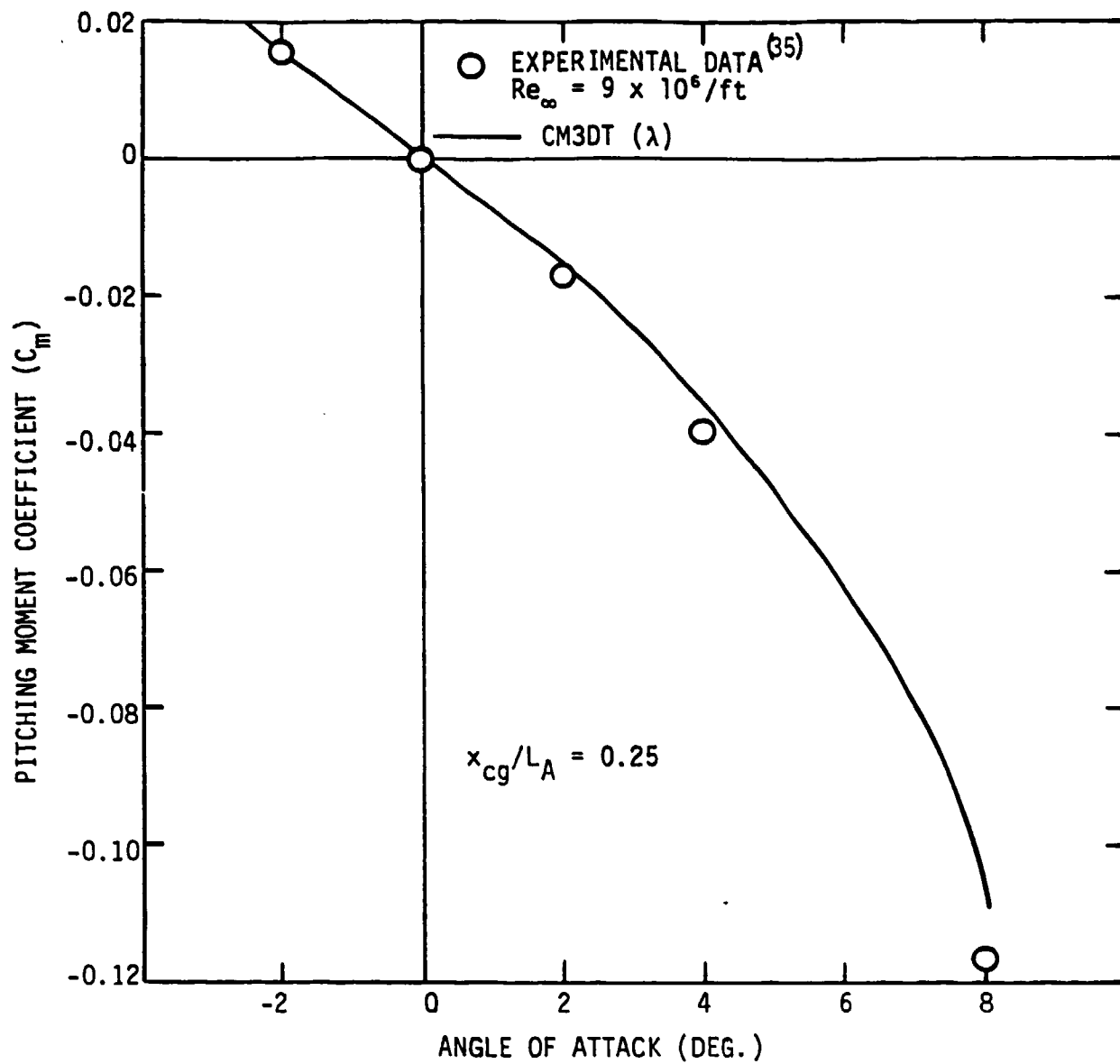


FIGURE 6.23. PITCHING MOMENT COEFFICIENT VS. ANGLE OF ATTACK FOR VMIB CONFIGURATION AT $M_{\infty} = 11.6$

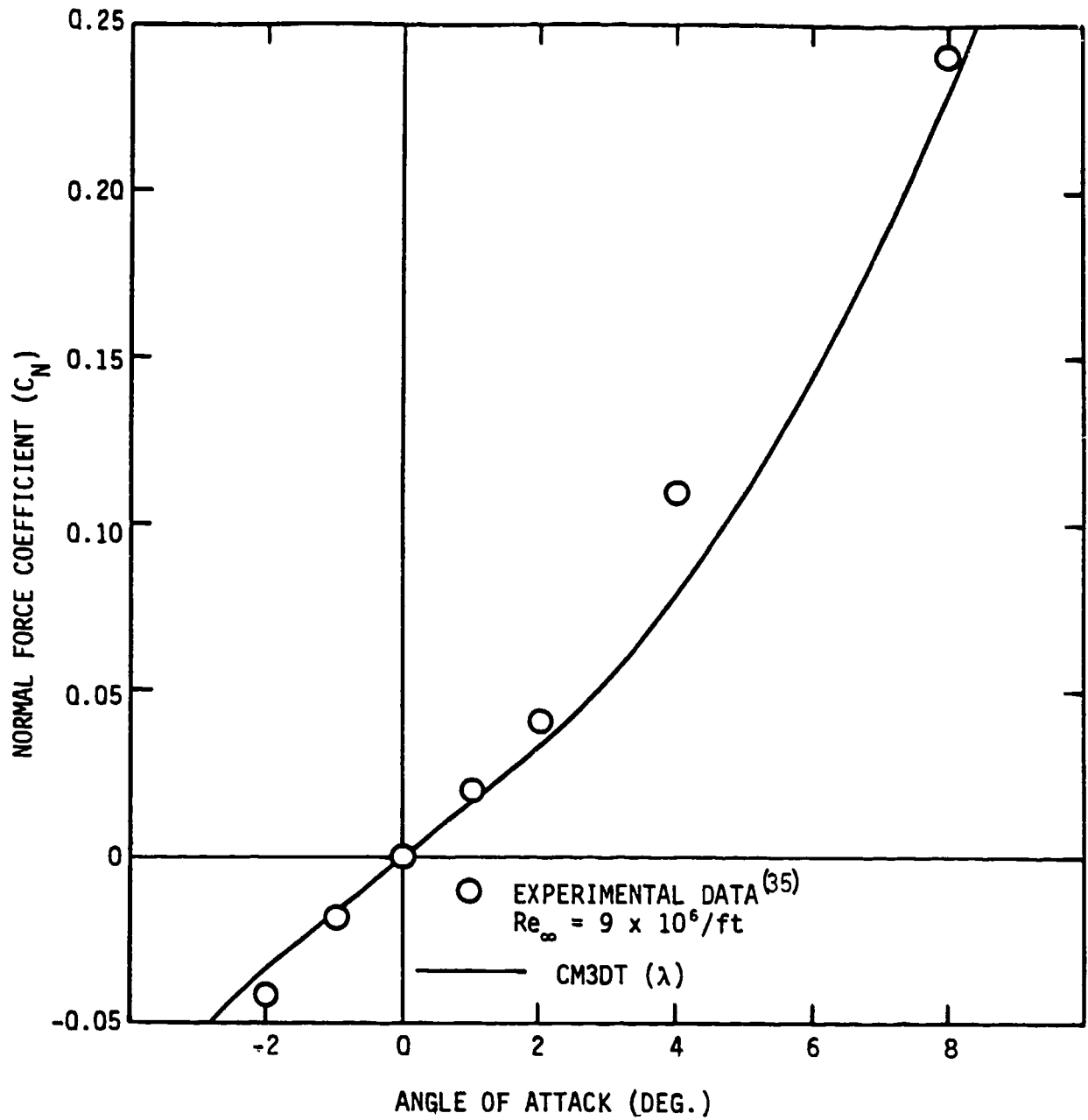


FIGURE 6.24. NORMAL FORCE COEFFICIENT VS. ANGLE OF ATTACK FOR MIB CONFIGURATION AT $M_\infty = 11.6$

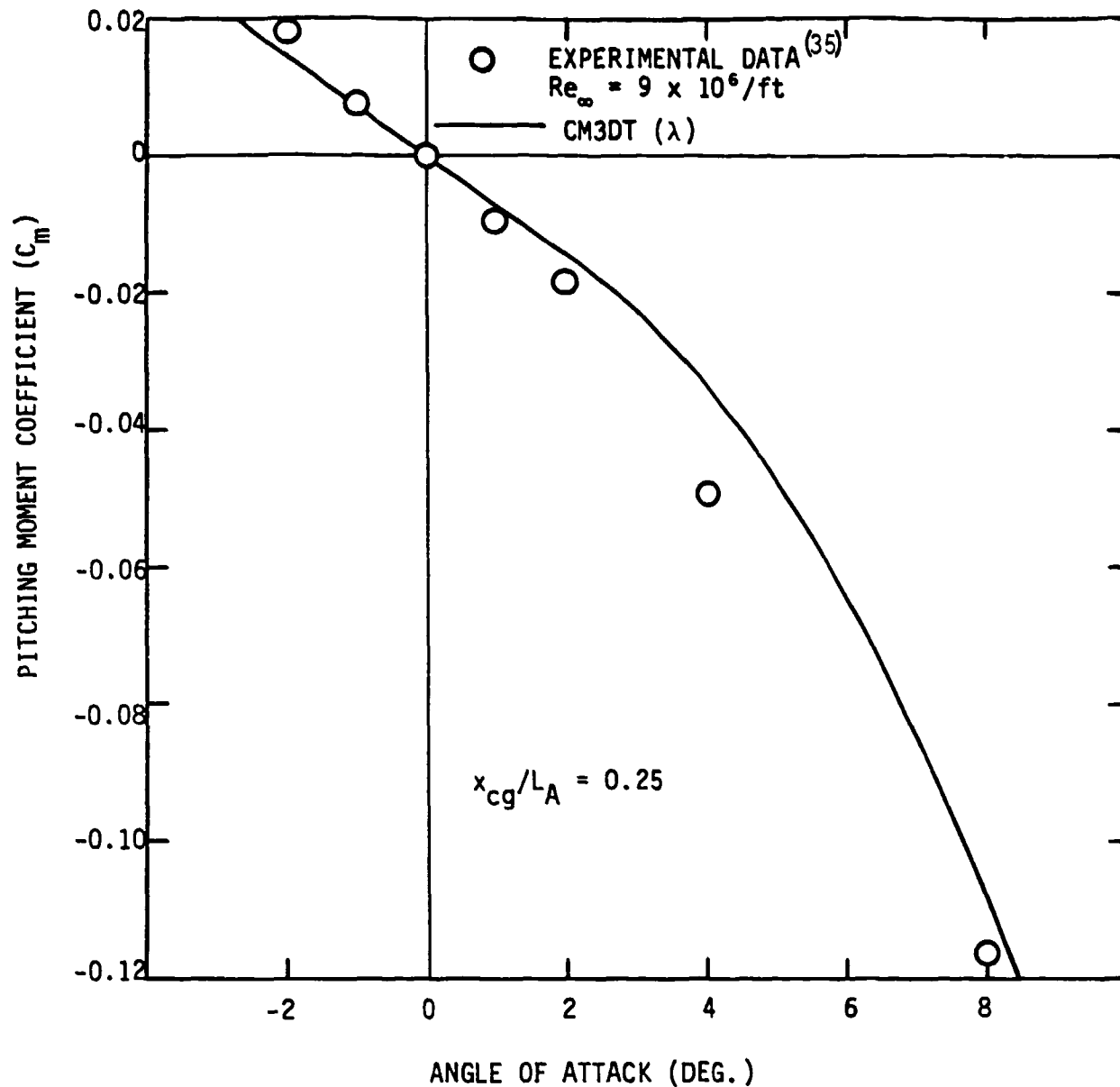


FIGURE 6.25. PITCHING MOMENT COEFFICIENT VS. ANGLE OF ATTACK FOR MIB CONFIGURATION AT $M_\infty = 11.6$

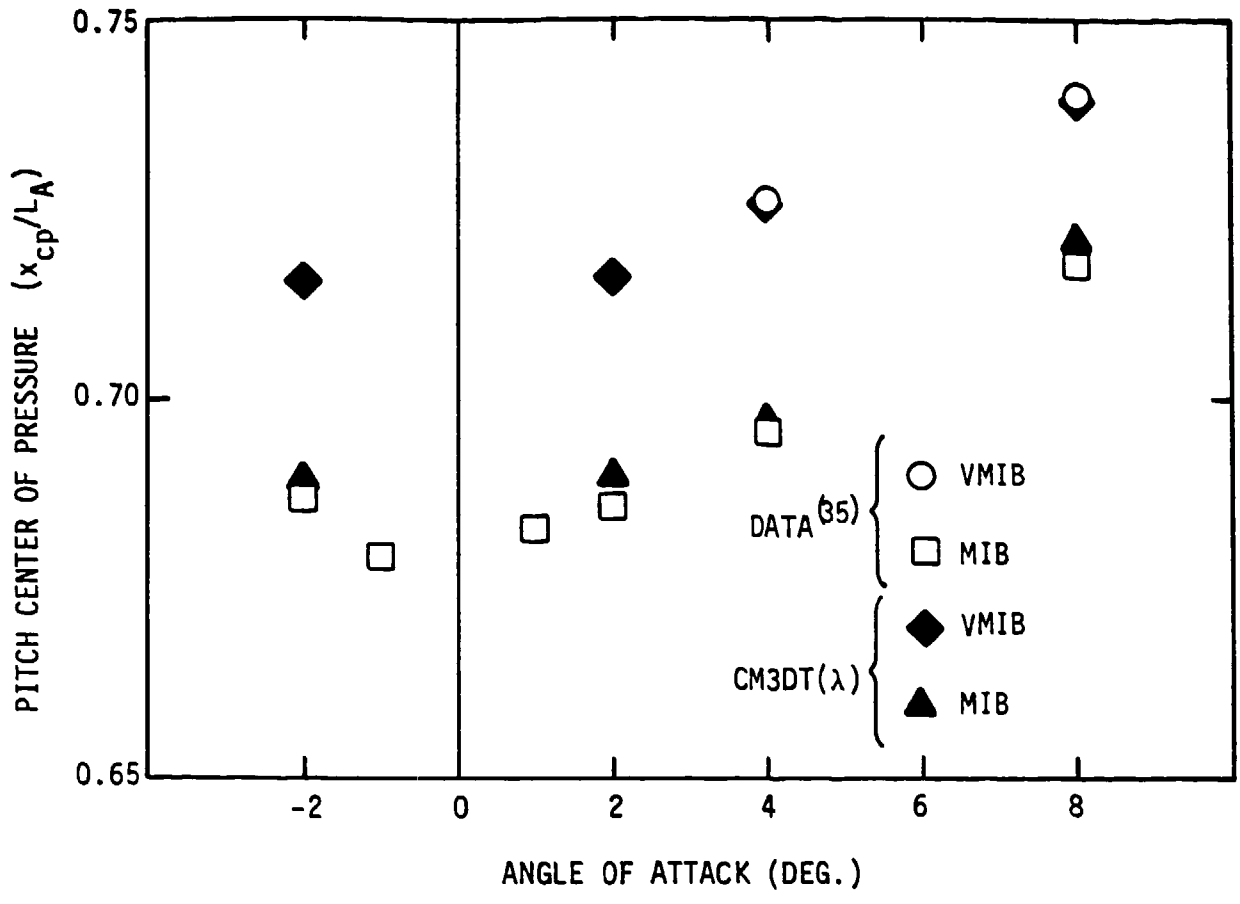


FIGURE 6.26. PITCH CENTER OF PRESSURE VS. ANGLE OF ATTACK FOR VMIB AND MIB CONFIGURATIONS AT $M_\infty = 11.6$

SECTION 7

CONCLUSIONS

The goal of this research effort has been the development of a computational technique for the prediction of inviscid flow fields about ablated reentry vehicle nosetips. The development of this capability has required the elimination of two major deficiencies in existing supersonic blunt body flow field procedures. First, a coordinate system has been developed that is capable of being closely aligned with ablated nosetip shapes, producing coordinate surfaces that are either nearly parallel or nearly normal to the nosetip surface. Second, an approximate capability has been developed for the calculation of embedded shocks on indented nosetips.

The new three-dimensional coordinate system is based on sequences of conformal transformations that are carried out independently in each meridional plane. The conformal transformations developed for this effort are defined in terms of "hinge points", which are discrete points selected such that the body contours are modeled in an approximate manner.

A three-dimensional blunt body code has been developed using this new coordinate system, with the governing equations written in non-conservation form. A second-order accurate, explicit procedure has been used to integrate the time-dependent equations, with the steady state solution being sought as the asymptotic limit of an unsteady flow. Body points and bow shock points are computed using special algorithms that are based on the method of characteristics.

This new three-dimensional blunt body code has extended the range of nosetip geometries for which inviscid flows can be successfully computed. For ablated nosetips without embedded shocks, this technique has demonstrated excellent agreement with experimental data and (for sufficiently regular shapes) with other numerical techniques.

As a first step in treating the embedded shock problem on ablated nosetips, two shock-capturing techniques have been examined for the axisymmetric problem. These two procedures, the conservation formulation and the λ -differencing approach, can only approximate discrete embedded shocks, but do not require special logic to detect the embedded shocks or to treat their movement through the coordinate mesh during the time-dependent calculation. Comparisons of these two techniques have been carried out by developing two axisymmetric time-dependent blunt body codes, using the new coordinate system developed in the first part of this effort.

The conservation formulation, in which the dependent variables used are derived from the integral conservation laws, was found to require numerical damping to control the oscillations produced when capturing a shock. This artificial damping has been demonstrated to have the potential of distorting the shock layer being computed, leading to smooth but inaccurate results.

In the λ -differencing approach, in which the non-conservation form of the governing equations is solved using a finite difference scheme that accurately models the domain of dependence of each mesh point, no numerical damping was required. In general, the λ -differencing scheme has been found to produce better agreement with experimental data for nosetips with embedded shocks than the conservation approach.

The λ -differencing scheme is at best, however, an approximate embedded shock solution, since there is no mechanism for an increase in entropy across the "captured" embedded shock.

Based on this comparison of axisymmetric shock-capturing techniques, the λ -differencing scheme was selected for extension to the three-dimensional problem, using the new coordinate system. (This effort is the first use of the λ -differencing scheme for a three-dimensional, time-dependent problem.) The three-dimensional λ -differencing scheme has produced good agreement with experimental data for indented nosetips at angle of attack.

In addition to its shock-capturing abilities, the λ -differencing scheme has also demonstrated an ability to eliminate oscillations that appear in other blunt body solutions at sharp corners in supersonic flow. This capability arises from the accurate modeling of the domain of dependence of each grid point by the λ -differencing scheme, preventing disturbances from propagating upstream in supersonic flow. The capabilities of the λ -differencing scheme are evidence of the importance of considering the physics of the flow when developing a numerical simulation.

The codes developed in this effort have significantly increased the range of ablated nosetip geometries for which inviscid aerodynamic predictions can be obtained. Coupling these nosetip codes to an existing supersonic afterbody code has provided a unique capability for the determination of inviscid aerodynamic performance for an entire reentry vehicle, both for pre-flight aerodynamic predictions and for post-flight performance analyses. The utility of these codes is enhanced by their relative efficiency, with a

typical nosetip flow field calculation requiring approximately three minutes on the CDC Cyber 176 computer, allowing the use of these codes on a routine basis for design and evaluation efforts.

Extension of the current effort would require the development of a procedure for treating embedded shocks as discrete discontinuities. Such a shock-fitting technique, in which the Rankine-Hugoniot conditions are strictly enforced across the embedded shocks, would remove the approximations inherent in the isentropic λ -differencing scheme. The development of a shock-fitting algorithm will be simplified by the use of the λ -differencing scheme since the λ -scheme provides a convenient, reliable method for the detection of shocks. Coupled with the generalized coordinate system developed in this effort, a shock-fitting technique would represent the ultimate capability for flow field predictions for ablated reentry vehicle nosetips, subject to the limitations inherent in the assumption of inviscid flow.

SECTION 8

REFERENCES

1. Dirling, R. B., Jr., "Asymmetric Nosetip Shape Change During Atmospheric Entry," AIAA Paper No. 77-779, June, 1977.
2. Pettus, J. J., Larmour, R. A., and Palmer, R. H., "A Phenomenological Framework for Reentry Dispersion Source Modeling," AIAA Paper 77-1152, August, 1977.
3. Hayes, W. D. and Probstein, R. F., *Hypersonic Flow Theory*, 1st edition, Academic Press, New York, 1959.
4. Hall, D. W., Kyriss, C. L., Truncellito, N. T., and Martellucci, A., "Nose Trim Study, Volume II. An Evaluation of the G.E. Three-Dimensional Flow Field Program for Ballistic Reentry Vehicles with Asymmetric Noses," SAMSO TR-77-46, September, 1976.
5. Hall, D. W. and Nowlan, D. T., "Aerodynamics of Ballistic Reentry Vehicles with Asymmetric Nosetips," *J. Spacecraft and Rockets*, 15, 1, 55-61, Jan.-Feb., 1978.
6. Moretti, G. and Salas, M., "The Blunt Body Problem for a Viscous Rarefied Gas Flow," AIAA Paper 69-139, January, 1969.
7. McCormack, R. W., "The Effect of Viscosity in Hypervelocity Impact Cratering," AIAA Paper 69-354, January, 1969.
8. Kyriss, C. L. and Harris, T. B., "A Three-Dimensional Flow Field Computer Program for Maneuvering and Ballistic Reentry Vehicles," presented at the 10th USN Aeroballistics Symposium, July, 1975.
9. Moretti, G. and Pandolfi, M., "Entropy Layers," Polytechnic Institute of Brooklyn, PIBAL Report 71-33, November, 1971.
10. Kutler, P., Reinhardt, W. A., and Warming, R. F., "Numerical Computation of Multi-Shocked, Three-Dimensional Supersonic Flow Fields with Real Gas Effects," *AIAA J.*, 11, 5, 657-664, May, 1973.
11. Marconi, F., Salas, M., and Yaeger, L., "Development of a Computer Code for Calculating the Steady Super/Hypersonic Inviscid Flow Around Real Configurations. Volume I - Computational Technique," NASA CR-2675, April, 1976.
12. Solomon, J. M., Ciment, M., Ferguson, R. E., Bell, J. B., Wardlaw, A. B., Jr., "A Program for Computing Steady Inviscid Three-Dimensional Supersonic Flow on Reentry Vehicles, Volume I: Analysis and Programming," NSWC/WOL/TR 77-28, February, 1977.
13. Kentzer, C. P., "Discretization of Boundary Conditions on Moving Discontinuities," Second International Conference on Numerical Methods in Fluid Dynamics, University of California, Berkeley, September 15-19, 1970.

14. Hall, D. W., "The Influence of Boundary Point Procedures on Accuracy and Efficiency in Flow Field Calculations," General Electric Co., TIS 77SDR016, March, 1977.
15. Moretti, G., "Calculation of the Three-Dimensional, Supersonic, Inviscid, Steady Flow Past an Arrow-Winged Airframe," Polytechnic Institute of New York, POLY-AE/AM Report No. 76-8, May, 1976.
16. Moretti, G., "Conformal Mappings for Computations of Steady, Three-Dimensional, Supersonic Flows," *Numerical/Laboratory Computer Methods in Fluid Mechanics*, ed. A. A. Poring and V. I. Shah, ASME, New York, 1976.
17. Moretti, G., "Computation of Shock Layers about Ablated, Blunt-Nosed Bodies," Polytechnic Institute of New York, POLY-M/AE Report No. 77-14, August, 1977.
18. Kutler, P., Chakravarthy, S., and Lombard, C., "Supersonic Flow over Ablated Nosed Tips Using an Unsteady, Implicit Numerical Procedure," AIAA Paper 78-213, January, 1978.
19. Moretti, G., "An Old Integration Scheme for Compressible Flow Revisited, Refurbished, and Put to Work," Polytechnic Institute of New York, POLY-M/AE Report No. 78-22, September, 1978.
20. Reeves, B. L., Todisco, A., Lin, T. C., and Pallone, A., "Hypersonic Flow over Indented Nosed Tips - STREET-A IV Experiments and Data Analysis," SAMSO TR-76-69, Volume X, April, 1976.
21. Jackson, M. D. and Baker, D. L., "Interim Report - Passive Nosed Tip Technology (PANT) Program, Volume IV. Heat Transfer and Pressure Distribution on Ablated Shapes - Part I. Experimental Data," SAMSO TR-74-86, Volume IV, Part I, January, 1974.
22. Swigart, R. J., "A Theory of Asymmetric Hypersonic Blunt Body Flows," *AIAA J.*, 1, 5, 1034-1042, May, 1963.
23. Xerikos, J. and Anderson, W. A., "An Experimental Study of the Entropy Layer Surrounding a Blunt Body at Angle of Attack," NASA CR 94481, October, 1967.
24. Rusanov, V. V., "A Blunt Body in a Supersonic Stream," *Annual Review of Fluid Mechanics*, Volume 8, ed. M. VanDyke and W. G. Vincente, Annual Reviews, Inc., Palo Alto, California, 1976.
25. MacCormack, R. W. and Paullay, A. J., "The Influence of the Computational Mesh on Accuracy for Initial Value Problems with Discontinuous or Nonunique Solutions," *Computers and Fluids*, 2, 339-361, 1974.
26. Vinokur, M., "Conservation Equations of Gasdynamics in Curvilinear Coordinate Systems," *J. Comp. Physics*, 14, 105-125, 1974.

27. Lax, P. and Wendroff, B., "Systems of Conservation Laws," *Comm. Pure Appl. Math.*, 13, 2, 217-237, May, 1960.
28. Reeves, B. L., "Analysis of Unsteady Flow Separation over Severely Indented Nosedips," SAMSO TR-75-269, Vol. VI, September, 1975.
29. Abbett, M. J. and Davis, J. E., "Interim Report, Passive Nosedip Technology (PANT) Program, Volume IV. Heat Transfer and Pressure Distribution on Ablated Shapes, Part II. Data Correlation and Analysis," SAMSO TR-74-86, Volume IV, Part II, January, 1974.
30. Courant, R., Friedrichs, K. and Lewy, H., "On the Partial Difference Equations of Mathematical Physics," *Math. Ann.*, 100, 32-74, 1928; reprinted in *IBM Journal*, March, 1967.
31. deNeef, T., "Treatment of Boundaries in Unsteady Inviscid Flow Computations," Delft University of Technology, Report LR262, February, 1978.
32. Moretti, G., "A Pragmatical Analysis of Discretization Procedures for Initial and Boundary Value Problems in Gas Dynamics and Their Influence on Accuracy or, Look Ma, No Wiggles!," Polytechnic Institute of New York, POLY-AE/AM Report No. 74-15, September, 1974.
33. Lomax, H. and Inouye, M., "Numerical Analysis of Flow Properties about Blunt Bodies Moving at Supersonic Speeds in an Equilibrium Gas," NASA Technical Report TR R-204, July, 1974.
34. Hahn, J. S. and Little, H. R., "Force and Pressure Tests on Cones with Simulated Ablated Noses at Mach Numbers 8 and 16," Arnold Engineering Development Center, AEDC-TR-72-52, April, 1972.
35. Boudreau, A. H., Crain, W. K., and Edenfield, E. E., "Force, Pressure, and Heat-Transfer Measurements on a Family of Ablated Shapes at Mach 8 and 12," Arnold Engineering Development Center, AEDC-TR-76-96, June, 1976.

APPENDIX

COEFFICIENTS FOR THE SHOCK ACCELERATION EQUATION

In Section 5.4, a form of the characteristic compatibility condition for bow shock points written in terms of the shock acceleration c_{TT} is given by Equation (5.36). Because of the complexity of the resulting equation, the shock acceleration is written for convenience in terms of a number of coefficients, which are derived in this Appendix.

First, it is necessary to find the time variation of the unit shock normal by differentiating Equations (5.29)-(5.31), resulting in

$$N_{2T} = -N_2(\phi_2 c_T + v_T/v) \quad (A.1)$$

$$N_{1T} = -c_\xi N_{2T} - N_2 c_{\xi T} \quad (A.2)$$

$$N_{3T} = -N_3(\tilde{C}c_T/Gy + v_T/v) + [c_T(G_\phi/G + c_\xi \omega_\phi) - \xi_\phi c_{\xi T} - c_{\theta T}]/y\nu \quad (A.3)$$

where

$$\begin{aligned} v_T = & N_2 [G\{-\phi_2 c_T (1+c_\xi^2) + c_\xi c_{\xi T}\} \\ & - \tilde{C}c_T (\eta_\phi - \xi_\phi c_\xi - c_\theta)^2 / G^2 y^3 \\ & + \{c_T(G_\phi/G + c_\xi \omega_\phi) - \xi_\phi c_{\xi T} - c_{\theta T}\} (\eta_\phi - \xi_\phi c_\xi - c_\theta) / Gy^2] \quad (A.4) \end{aligned}$$

Defining

$$\tilde{u}_{\infty T} = C_1 c_{TT} + C_2 \quad (A.5)$$

and differentiating Equation (5.24) results in

$$C_1 = -N_2/G \quad (A.6)$$

$$C_2 = \phi_1 c_T (-v_\infty N_1 + u_\infty N_2) - c_T^2 \phi_2 N_2/G \\ + u_\infty N_{1T} + (v_\infty - c_T/G) N_{2T} + w_\infty N_{3T} \quad (A.7)$$

where it has been noted that

$$u_{\infty T} = -v_\infty \phi_1 c_T$$

$$v_{\infty T} = u_\infty \phi_1 c_T$$

Other required time derivatives are defined as

$$P_T = C_3 c_{TT} + C_4 \quad (A.8)$$

$$\tilde{u}_T = C_5 c_{TT} + C_6 \quad (A.9)$$

which are to be evaluated from

$$P_T = \frac{\partial P}{\partial \tilde{u}_\infty} \tilde{u}_{\infty T} \quad (A.10)$$

$$u_T = \frac{\partial \tilde{u}}{\partial \tilde{u}_\infty} u_{\infty T} \quad (A.11)$$

resulting in

$$C_3 = \frac{\partial P}{\partial \tilde{u}_\infty} C_1 \quad (A.12)$$

$$C_4 = \frac{\partial P}{\partial \tilde{u}_\infty} C_2 \quad (A.13)$$

$$C_5 = \frac{\partial \tilde{u}}{\partial \tilde{u}_\infty} C_1 \quad (A.14)$$

$$C_6 = \frac{\partial \tilde{u}}{\partial \tilde{u}_\infty} C_2 \quad (A.15)$$

The derivatives $\partial P/\partial \bar{u}_\infty$ and $\partial \bar{u}/\partial \bar{u}_\infty$ may be evaluated by straightforward differentiation of the well-known Rankine-Hugoniot conditions for an ideal gas; for equilibrium real gas thermodynamics, where the Rankine-Hugoniot conditions must be solved by iteration, these derivatives may be evaluated numerically from tables of shock properties as functions of \bar{u}_∞ .

Velocity components downstream of the shock, given by Equations (5.34)-(5.36) may be differentiated to give

$$u_T = C_9 c_{TT} + C_{10} \quad (\text{A.16})$$

$$v_T = C_{11} c_{TT} + C_{12} \quad (\text{A.17})$$

$$w_T = C_{13} c_{TT} + C_{14} \quad (\text{A.18})$$

where

$$C_9 = (C_5 - C_1) N_1 \quad (\text{A.19})$$

$$C_{10} = -v_\infty \phi_1 c_T + (C_6 - C_2) N_1 + (\bar{u} - \bar{u}_\infty) N_{1T} \quad (\text{A.20})$$

$$C_{11} = (C_5 - C_1) N_2 \quad (\text{A.21})$$

$$C_{12} = u_\infty \phi_1 c_T + (C_6 - C_2) N_2 + (\bar{u} - \bar{u}_\infty) N_{2T} \quad (\text{A.22})$$

$$C_{13} = (C_5 - C_1) N_3 \quad (\text{A.23})$$

$$C_{14} = (C_6 - C_2) N_3 + (\bar{u} - \bar{u}_\infty) N_{3T} \quad (\text{A.24})$$

The coefficients C_7 and C_8 are defined for convenience as

$$C_7 = C_5 - C_1 \quad (A.25)$$

$$C_8 = C_6 - C_2 \quad (A.26)$$

DISTRIBUTION LIST

Ballistic Missile Office
BMO/SYDT

Attn: Maj. K. Yelmgren (2)
Norton AFB, CA 92409

Defense Technical Information Center (2)
Cameron Station
Alexandria, VA 22314

Air University Library
Maxwell AFB, AL 36112

TRW DSSG
Attn: W. Grabowsky (2)
P. O. Box 1310
San Bernardino, CA 92402

TRW Systems Group (2)
Attn: J. Ohrenberger
M. Gyetvay
1 Space Park
Redondo Beach, CA 92078

Headquarters, Arnold Engineering
Development Center
Arnold Air Force Station
Attn: Library/Documents
Tullahoma, TN 37389

Armament Development and Test Center
Attn: Technical Library, DLOSL
Eglin AFB, FL 32542

Air Force Wright Aeronautical Laboratories (3)
Air Force Systems Command
Attn: M. Buck (AFWAL/FIM)
R. Neumann (AFWAL/FIMG)
V. Dahlem (AFWAL/FIMG)
Wright-Patterson AFB, OH 45433

U. S. Army Ballistic Missile
Defense Agency/ATC-M
Attn: J. Papadopoulos
P. O. Box 1500
Huntsville, AL 35807

Director, Defense Nuclear Agency
Attn: J. Somers (SPAS)
Washington, DC 20305

Naval Surface Weapons Center
Attn: Carson Lyons/K06
White Oak Laboratories
Silver Spring, MD 20910

Acurex Aerotherm
Aerospace Systems Division
Attn: C. Nardo
485 Clyde Avenue
Mountain View, CA 94042

Avco Systems Division
Attn: N. Thyson
201 Lowell Street
Wilmington, Mass 01887

General Electric Company
Attn: R. Neff
3198 Chestnut Street
Philadelphia, PA 19101

Lockheed Missiles and Space Co.
P. O. Box 504
Attn: G. T. Chrusciel
Sunnyvale, CA 94086

McDonnell Douglas Astronautics Co.
Attn: J. Copper
5301 Bolsa Avenue
Huntington Beach, CA 92647

PDA Engineering
Attn: M. Sherman
1560 Brookhollow Drive
Santa Ana, CA 92705

Sandia Laboratories
P. O. Box 5800
Attn: Library
Albuquerque, NM 87115

Science Applications, Inc.
Attn: A. Martellucci
994 Old Eagle School Road
Suite 1018
Wayne, PA 19087